LONG SCALE PHASE SEPARATION VERSUS HOMOGENEOUS MAGNETIC STATE IN $(La_{1-y}Pr_y)_{0.7}Ca_{0.3}MnO_3$

V. Pomjakushin[1,2]*, A. Balagurov*[1]*, D. Sheptyakov*[1,2]*, V.Aksenov*[1]*, P. Fischer*[2]*, L. Keller*
O.Gorbenko [3]*, A. Kaul* [3]*, N. Babushkina*[4]

[1] *Frank Laboratory of Neutron Physics, JINR 141980, Dubna, Russia*
[2] *Laboratory for Neutron Scattering ETHZ & PSI, CH-5232, Villigen PSI*
[3] *Chemical Department. Moscow State University, 119899, Moscow, Russia*
[4]*RSC "Kurchatov Institute", 123182 Moscow, Russia*

The magnetic structure of the colossal magnetoresistance perovskite manganites $(La_{1-y}Pr_y)_{0.7}Ca_{0.3}MnO_3$ for y from 0.5 to 1.0 has been studied by neutron powder diffraction in the temperature range from 10 to 293 K and in external magnetic fields up to 4 Tesla at DMC/SINQ, DN12/IBR2 and HRFD/IBR2 [1-2]. This family has a fixed optimal electron doping and variable

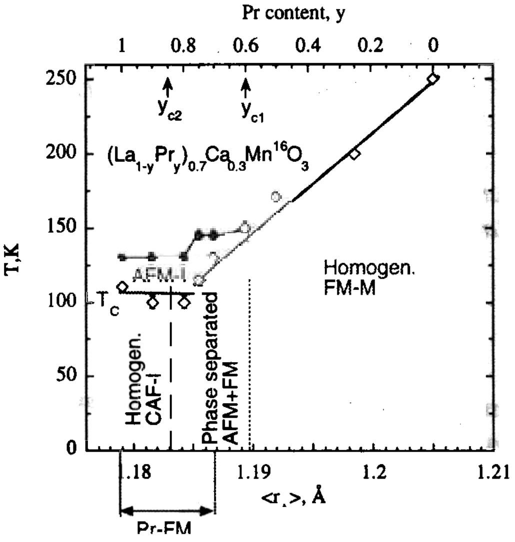

Fig. *1: Phase diagram of the* $(La_{1-y}Pr_y)_{0.7}Ca_{0.3}MnO_3$ *shows temperatures of magnetic ordering of Mn-ions. The bottom x-axis shows average A-cation radius* $<r_A>$*. The low temperature state is homogeneous for y>0.8 (canted antiferromagnetic insulator CAF-I) and for y<0.6 (ferromagnetic metal FM-M). In addition, a ferromagnetic contribution of the Pr-moments parallel to the ferromagnetic component of Mn-moments is found for y>0.6. The moment of Pr scales with the ferromagnetic Mn-moment rather than with the Pr-concentration and thus presumably induced by Mn.*

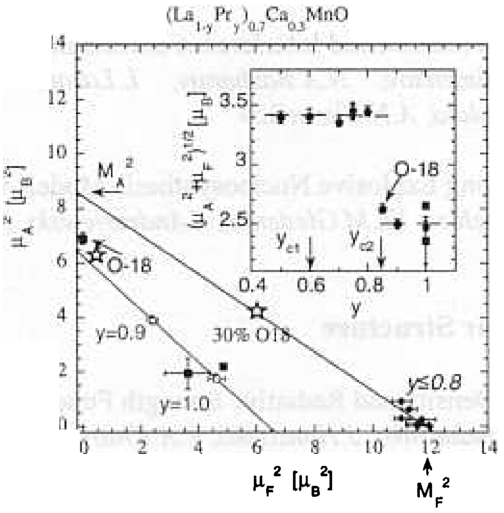

Fig. 2*: The squares of the antiferromagnetic component* μ_A^2 *as a function of the ferromagnetic (F) magnetic moment component* μ_F^2 *with Pr-concentration y as a parameter. The lines are the linear LS-fits to the data points for y≤0.8 and y>0.8. The* ^{18}O*-enriched samples (y=0.75) are also shown. 75%-enriched sample has no F-component at all (O-18), serving as a reference of pure antiferromagnetic state. The stars show samples with partial isotope substitution: 30% and 55%. The insert shows the total magnetic moment as a function of the Pr-concentration.*

A-cation radius $<r_A>$ which is linearly connected with the Pr-concentration y. It is believed that the principal effect of decreasing $<r_A>$ is a decrease in the charge carrier bandwidth W, which is proportional to T_C in the double exchange model. Our data show that the phase diagram has a border region of concentrations $0.6 \leq y \leq 0.8$ separating the homogeneous FM metallic and canted AFM (pseudo CE-type) insulating states. In this region the low temperature magnetic state is macroscopically (>10^3 Å) incoherently spatially separated into AFM an FM phases. The FM phase has a small non-collinearity of C-type, presumably due to interfaces to the AF-phase. The macroscopical clusters can be induced by disorder on the carriers hopping amplitude caused by natural dispersion of the A-cation radius near the metal-insulator transition around y=0.7 [3]. For the concentrations $y \geq 0.9$ the long range ordered magnetic state is homogeneous with a canted AF structure. The total long-range ordered magnetic moment of the Mn-ion shows a step like decrease from $\mu_{Mn}=3.4\mu_B$ to $2.5\mu_B$ as a function of Pr-concentration at the transition to a homogeneous canted antiferromagnetic (CAF) state (Fig.2). The canting angle is significantly increased on doping, while the total magnetic moment stays constant for $y \geq 0.9$. The spatial inhomogeneities can still be present for $y \geq 0.9$, according to the reduced μ_{Mn}-value, but the Mn-spins between the homogeneously CAF-ordered moments have to be either short range ordered or paramagnetic. The ^{18}O-isotope substitution for y=0.75 acts like increase of y: the effective bandwidth is decreased due to JT-polaronic effect. The sample with 75% substitution of ^{18}O (O18) reveals the ordered magnetic moment close to the natural isotope samples with y>0.8. This places O18 in the region above the concentrational transition at yc2.

REFERENCES

[1] A. Balagurov, V.Pomjakushin, D.Sheptyakov et al, Phys. Rev. **B** 60, 383 (1999).

[2] A.Balagurov, V.Pomjakushin, D.Sheptyakov, V.Aksenov, P. Fischer et al, Accepted in Phys. Rev. **B** (2001).

[3] A.Moreo et al, Phys. Rev. Lett. **84**, 5568 (2000).

Effect of partial $^{16}O \rightarrow {}^{18}O$ substitution on the magnetic structure of $(La_{0.25}Pr_{0.75})_{0.7}Ca_{0.3}MnO_3$

D.V. Sheptyakov[a,b], V.Yu. Pomjakushin[a], V.L. Aksenov[a], A.M. Balagurov[a], N.A. Babushkina[c], O.Yu. Gorbenko[d], A.R.Kaul[d]

[a]*FLNP JINR, Dubna, Russia*
[b]*Laboratory for Neutron Scattering ETHZ & PSI, 5232 Villigen PSI, Switzerland*
[c]*RRC Kurchatov Institute, Moscow, Russia*
[d]*Chemistry Department, Moscow State University, Moscow, Russia*

The magnetic structure and phase diagram of $(La_{1-y}Pr_y)_{0.7}Ca_{0.3}MnO_3$ compound with $0.5 \leq y \leq 1$ have been systematically studied by neutron powder diffraction **[1-3]**. For composition with y=0.75 (LPCM-75), the analysis was performed on two samples, one containing the natural mixture of oxygen isotopes (99.7% ^{16}O-sample, metallic at T≤100 K), and the other one 75%–enriched by ^{18}O (^{18}O-sample, insulating in all temperature range). At first it was found that both samples have identical crystal structures at room temperature. At the temperature lowering, the sample with ^{16}O undergoes subsequent antiferromagnetic (T_{AFM}=150 K) and ferromagnetic (T_{FM}=110 K) transitions, while in the sample with ^{18}O the pure AFM ordering (T_{AFM}=150 K) was found. To get a better insight into the crossover between the FM+AFM metal and AFM insulator states we decided to study LPCM-75 samples with partial oxygen isotope substitution.

Altogether 11 samples with different values of the $r={}^{18}O/({}^{16}O+{}^{18}O)$ ratio were prepared and studied macroscopically **[4]**, and three of them with r=0.30, 0.55 and 0.63 were examined by neutron diffraction. Experiments were performed at the IBR-2 pulsed reactor with DN-12 diffractometer, which is specially designed for microsamples studies. Despite of small amount of samples (about 100 mg each) good enough quality diffraction patterns were measured in 2.5 – 4 hours at several temperatures. The values of magnetic moments were refined with the use of FullProf program.

It was found that at low temperature compositions with r=0.30 and 0.55 possess the same type of the magnetic structure as ^{16}O sample: phase separated FM + AFM (pseudo-CE), while in the composition with r=0.63 only AFM state (just as in ^{18}O sample) appears. The temperature dependencies of FM and AFM magnetic moments for r=0 [1], 0.30 and 0.55 are shown in **fig.1.** The dependence of μ_{AFM} for r=0.63 and 0.75 is practically the same as for r=0.55.

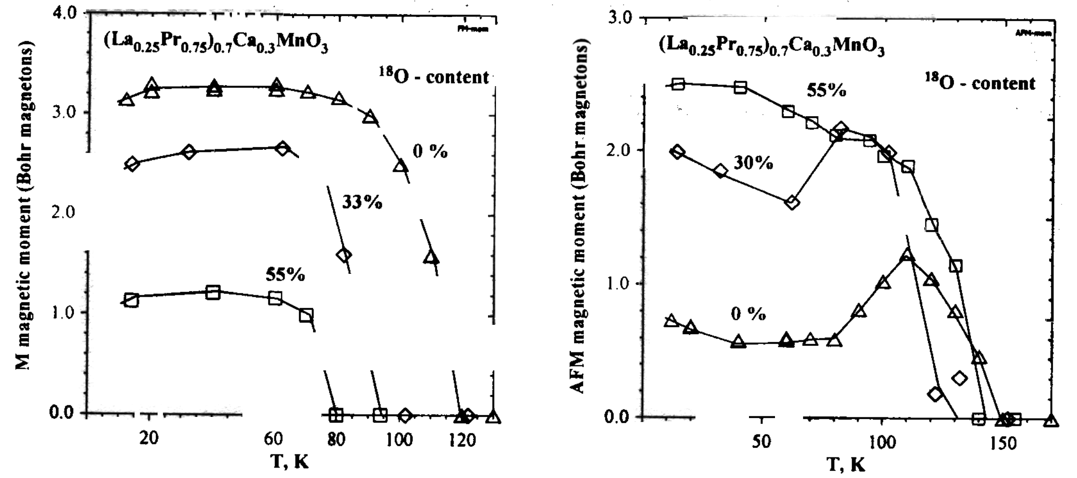

Fig.1. The temperature dependencies of FM (left part) and AFM (right part) magnetic moments of LPCM-75 with partial $^{16}O/^{18}O$ isotope substitution. The AFM moment lowering below the temperatures when FM phase appears is typical for phase separated state **[5]**.

One can see from fig.1 that T_{AFM} is more or less the same for all *r*, while T_{FM} decreases with *r*. The extracted from diffraction peaks intensity behaviour of the phase transition temperatures is displayed in **fig.2**.

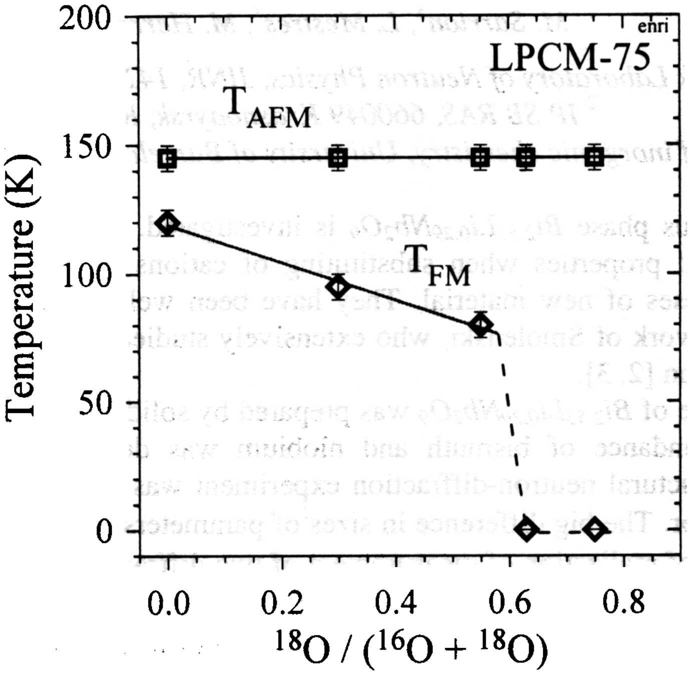

Fig.2. Dependence of T_{FM} and T_{AFM} phase transition temperatures on ^{18}O content in LPCM-75 samples. Points for r=0 and 0.75 are taken from Ref. [1].

The measurements of electrical resistivity and magnetic susceptibility show **[4]**, that samples with partial $^{16}O \rightarrow {}^{18}O$ isotope substitution behave as a percolation-type two-phase system consisting of the FM metal and AFM insulator. A critical value of ^{18}O for metal-insulator transition was found close to *r*=0.40. From the temperature behavior of magnetic moments values, the relative amounts of both magnetic phases at low temperature were estimated: 15% AFM + 85% FM for *r*=0; 50% AFM + 50% FM for *r*=0.3; and 98% AFM + 2% FM for *r*=0.55. These values are in good agreement with magnetic susceptibility data.

There are some attempts for explaining of so strong isotope effects in both LPCM-series and others manganites with CMR-effect (see, for instance, **[6]**) but details of this phenomenon are still far from clear understanding.

This work has been done with the help of RFBR program (project 00-02-16736).

References

1. A.M. Balagurov, V.Yu. Pomjakushin, D.V. Sheptyakov et al., Phys. Rev. B 60, 383 (1999).
2. A.M. Balagurov, P.Fischer, V.Yu. Pomjakushin et al., Physica B 276-278, 536 (2000).
3. A.M. Balagurov, V.Yu. Pomjakushin, D.V. Sheptyakov et al., Eur. Phys. J. (2001) accepted.
4. N.A.Babushkina, A.N.Taldenkov, L.M.Belova et al., Phys. Rev. B 62, R6081 (2001).
5. A.M. Balagurov, V.Yu. Pomjakushin, D.V. Sheptyakov, J.Phys.Soc.Japan, (2001) accepted.
6. N.M.Plakida, JETP Letters, 71, 720 (2000).

X-ray and neutron diffraction studies of a new Aurivillius phase $Bi_{2.53}Li_{0.29}Nb_2O_9$

A. M. Balagurov[1], *A. I. Beskrovniy*[1], *S. G. Vasilovskij*[1,2], *L. S. Smirnov*[1],
M. Sarrion[3], *L. Mestres*[3], *M. Herraiz*[3]

[1] *Frank Laboratory of Neutron Physics, JINR, 141980 Dubna, Russia*
[2] *IP SB RAS, 660049 Krasnoayrsk, Russia*
[3]*Departament of inorganic chemistry, University of Barselona, 08028, Barselona, Spain*

New Aurivillius phase $Bi_{2.53}Li_{0.29}Nb_2O_9$ is investigated. Structures of this type show hide variability of physical properties when substituting of cations of metal [1]. This opens greater possibilities at syntheses of new material. They have been well known as ferroelectric materials since the pioneering work of Smolenski, who extensively studied their ferroelectric properties as a function of composition [2, 3].

Powder sample of $Bi_{2.53}Li_{0.29}Nb_2O_9$ was prepared by solid-state reaction from Bi_2O_3, Li_2CO_3 and Nb_2O_5. The abundance of bismuth and niobium was determined by a method of x-ray fluorescence. The structural neutron-diffraction experiment was carried out in the FLNP, JINR at the IBR-2 pulse reactor. The big difference in sizes of parameters of an elementary cell (a=24.84 Å, c=5.45 Å) has served of realization of measurement of two diffractometers. On diffractometer DN-2 the neutron-diffraction date was measured in the range from 1 Å to 12 Å with the medium resolution. On diffractometer HRFD was received neutron-diffraction date in the range from 1 Å to 3.2 Å with high resolution. X-ray measurements were beforehand executed within the range of angle of scan from 6 ° to 80 °.

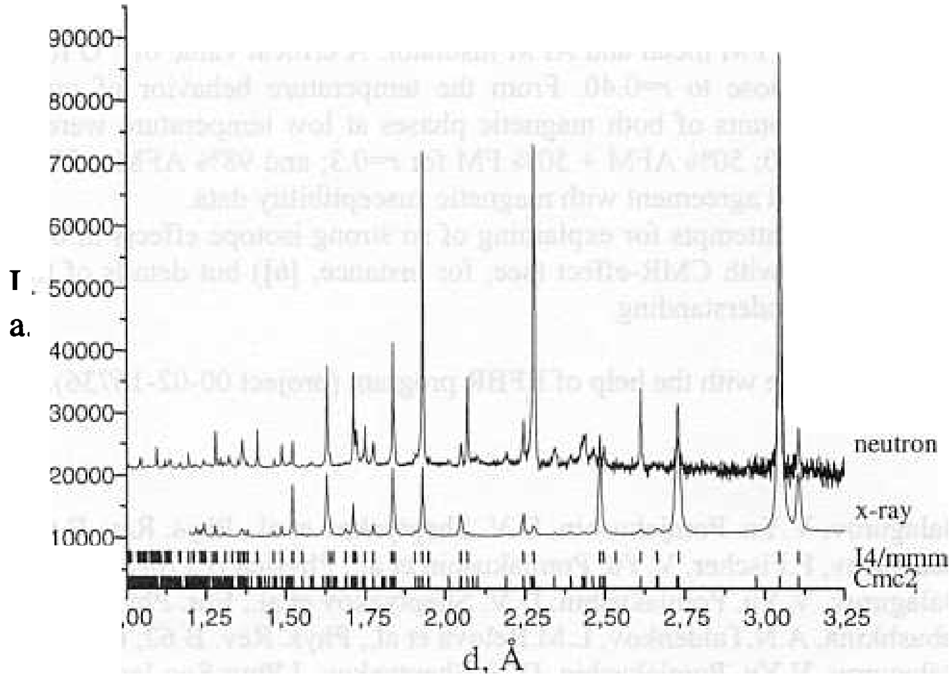

Fig.1

It was early show, the x-ray and neutron diffraction patterns showed that crystallographic structures phases of $Bi_2CaNb_2O_9$ and $Bi_2SrNb_2O_9$ are ortorombic with space group $Cmc2_1$. However, structure of $Bi_2BaNb_2O_9$ is tetragonal with space group $I4/mmm$ [4, 5].

Figure 1 shows the x-ray and neutron powder diffraction patterns at room temperature and afforded initial indexing the peaks. From figure it is visible, that only space group *Cmc2₁* describes all observably peaks.

Said above creates premises for suggestion that as initial terms when undertaking revision on method Rietveld possible use positions of atoms, determined for structures of $Bi_2CaNb_2O_9$ and $Bi_2SrNb_2O_9$ [4].

Under two temperatures (T=10 K and T=290 K) determined parameters of elementary cell, position of atoms in structure, sites and thermal factor in изотропном approach. Result Rietveld refinement profiles is brought on figures 2 and 3.

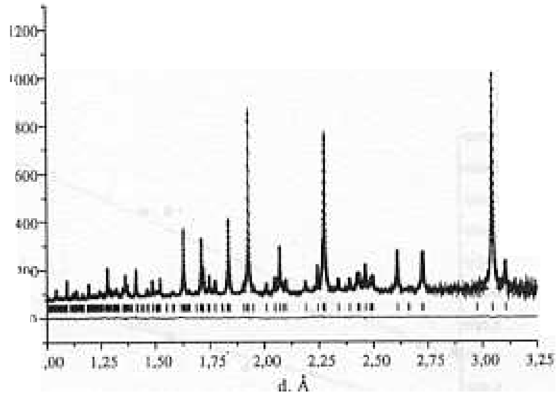

Fig.2. HRFD, T=10 K

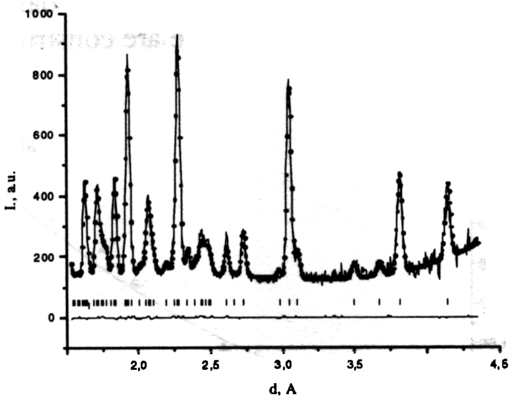

Fig.3. DN-2, T=290 K

In the structure to manage localize a position of atoms lithium. The possible variant of replacement of bismuth by lithium in bismuthic-oxide layer (position 8 (b)) was checked during specification of crystal structure. As a result of calculation the factor of population of lithium in position 8 (b) is received equal to zero. The received data give the basis to assume, that replacement of a bivalent ion with trivalent bismuth and univalent lithium results in occurrence of structural vacancies in the perofskite layer that can create favorable conditions for development of ionic conductivity on structural vacancies (fault ion conductivity).

On the received coordinates a bond valence method [6], calculation of valency V_{ij} for cations is calculated:

$$V_{ij} = \sum_{i}^{v} s_{ij}(R_{ij}) \tag{1}$$

where v – coordination number.

Dependence of valent effort s_{ij} on length of communication R is determined as:

$$s_{ij} = \exp[(R_{1j} - R_{ij})/b] \tag{2}$$

where R_1 - length of communication of individual valence, and the empirical parameter b is equaled 0.37 Å.

Atom	**Bond valence**		
	T=10 K	**T=290 K**	**Model**
Bi	3.03	2.89	3
(Bi/Li)	1.89	1.81	1.88
Nb	4.94	5.14	5

Arrangements of octahedrons in structure are distorted. Except this, noticeably garbling of their form. Below given lengths of communications of atoms, falling into octahedron.

Bond type	L, Å	
	T=10 K	T=290 K
Nb-O(1)	2.131	2.136
Nb-O(2)	1.868	1.831
Nb-O(4)	1.925 2.019	1.882 2.039
Nb-O(5)	1.957 2.054	1.992 2.085

For reception of more detailed information about sample, on difractometer DN-2 powder neutron diffraction data were collected at high temperature. Phase transitions in this area of temperatures it is not noticed. On the basis of the received data dependences of parameters of an elementary cell on temperature are constructed.

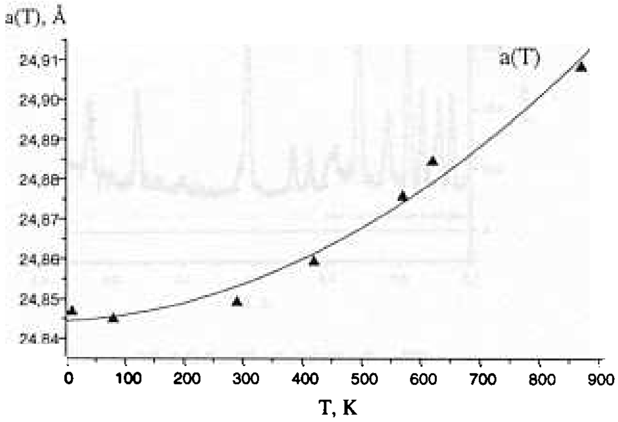

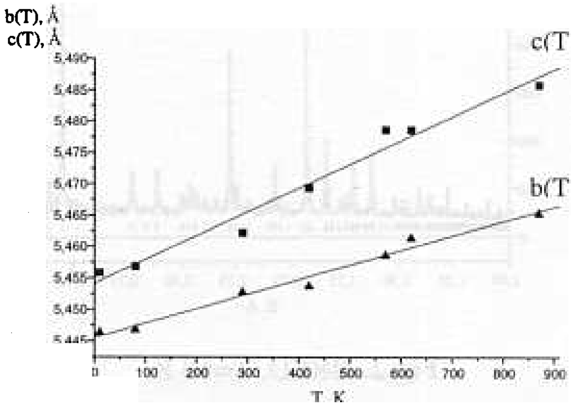

From the given dependences it is visible, that ortorhombic distortion of structure is increased with rise in temperature. It contradicts the data, which are given in [4] for $Bi_2(Sr, Ca)Nb_2O_9$.

1. K. S. Aleksandrov, B. V. Beznosikov, Crystals of type perouvskite, «Saince», Novosibirsk, 1999.
2. V. A. Isupov, Properties of the ferroelectric Aurivillius phases of type $A_{m-1}Bi_2M_mO_{3m+3}$, J. Unorgan. Chem, 1994, т. 39, №5, с. 731-737.
3. G. A. Smolenscki, Sov. Phys. Solid. State, 1959, 3, 651.
4. S. M. Blake, M. J. Falconer, M. McCredy, Cation disorder in ferroelectric Aurillius phases of the type $Bi_2ANb_2O_9$ ($A = Ba, Sr, Ca$), J. Matter. Chem., 1997, 7(8), 1609-1613.
5. Y. Shimacama, Y. Cubo, Crystal structure and ferroelectric properties of $Bi_2ATa_2O_9$ ($A = Ba, Sr, Ca$), Phisical Review B, v. 61, №10, 6559-6564.
6. V. S. Urusov, Theoretical chemistry of crystals, M., MSU, 1987.

PECULIARITIES OF INCOMMENSURATE PHASE IN FERROELECTRIC-SEMICONDUCTOR $TlInS_2$

A.I. Beskrovnyi[a], *B.R. Gadjiev*[a], *N.Yamamoto*[b], *N.Mamedov*[b], *S.Iida*[c], *H.Uchiki*[c] *and S.Kashida*[d]
[a] *Frank Laboratory of Neutron Phisics, Joint Institute for Nuclear Research, Dubna, Moscow region, Russia*
[b] *Department of Physics and Electronics, University of Osaka Prefecture, Osaka, Japan*
[c] *Department of Electrical Engineering, Nagaoka University of Technology, Nagaoka, Japan*
[d] *Department of Environment Science, Faculty of science, Niigata University, Niigata, Japan*

Incommensurate phases in ferroelectrics-semiconductors have a series of peculiarities. The most important one is a great influence of equilibrium and non-equilibrium carriers on the structure of incommensurate phase and possible change of the latter.

In this work we present the results of the full symmetry analysis of the succession of phase transitions of high-symmetry-commensurate-incommensurate type in ferroelectric-semiconductor $TlInS_2$ together with the results of temperature-dependent neutronography of this material. It is shown that the succession of high-symmetry-incommensurate-commensurate phase transitions in $TlInS_2$ is of improper ferroelectrical type.

In terms of a theoretical consideration the succession of high-symmetry-incommensurate-commensurate phase transitions in improper semiconductor-ferroelectric $TlInS_2$ shall be described by the irreducible representation of the space group C_{2h}^6 for the modulation wave vector $\vec{q} = (0,0,0.25)$ [1,2,3,4,5].

The full symmetry consideration in the framework of the theory of Landau shows that the functional of the thermodynamic potential of the $TlInS_2$ -type compounds can be written in the form

$$F = \iint_D f(x,z,\varphi(x,z),\varphi'_x,\varphi'_z)dxdz, \text{ were } f = \frac{\alpha}{2}\rho^2 + \frac{\beta}{4}\rho^4 + \gamma\rho^8 \cos n\varphi(x,z) - \delta_1\rho^2 \frac{\partial\varphi(x,z)}{\partial x} - \\ -\delta_2\rho^2 \frac{\partial\varphi(x,z)}{\partial z} + \frac{k_1}{2}\rho^2\left(\frac{\partial\varphi(x,z)}{\partial x}\right)^2 + \frac{k_2}{2}\rho^2\left(\frac{\partial\varphi(x,z)}{\partial z}\right)^2 + \frac{\upsilon}{2}\rho^2\left(\frac{\partial\varphi(x,z)}{\partial x}\right)\left(\frac{\partial\varphi(x,z)}{\partial z}\right) \quad (1)$$

The suddle equation corresponding to the functional (1) is represented by the expression

$$k_1\frac{\partial^2\varphi(x,z)}{\partial x^2} + k_2\frac{\partial^2\varphi(x,z)}{\partial z^2} + \nu\frac{\partial^2\varphi(x,z)}{\partial x\partial z} + n\gamma\rho^{n-2}\sin n\varphi(x,z) = 0 \quad (2)$$

The differential equation (2) is of hyperbolic type if $\nu^2 - 4k_1k_2 > 0$, of parabolic type if $\nu^2 - 4k_1k_2 = 0$ and of elliptical type if $\nu^2 - 4k_1k_2 < 0$.

In hyperbolic case the spatial distribution of the order parameter has the form

$$\psi(\xi,\eta) = 4arctg\left\{\frac{h'}{k'}sn\left[\left(\frac{16c}{6+4cd}\right)^{1/2}\frac{1}{k'}\xi\right]sn^{-1}\left[\left(\frac{16}{d}\right)\frac{1}{h'}\eta\right]\right\}. \quad (3)$$

The further analysis shows that in terms of Landau theory there takes place the $C_{2h}^6 \Rightarrow P_{1\bar{1}}^{C/2c} \Rightarrow P_{11}^{C2} \Rightarrow C_2^3 \Rightarrow S_2^1 \Rightarrow C_0^1$ succession of phase transitions in these materials as temperature decreases.

In the neutronographic experiments the tree-dimensional distributions of the diffraction intensity along the directions [100] and [001], and between directions [4, 0, 4] – [4, 0, 6] are measured at the temperatures 240*K*, 210*K*, 203*K*, 180*K* and 10*K*, chosen preliminary as possibly corresponding to the different phase states of $TlInS_2$.

The analysis of the two-dimensional cross-sections of the diffraction intensity at 240K shows that between directions [4, 0, 4] and [4, 0, 6] there are observed the corresponding Bragg peaks of the main lattice only. As temperature goes down to 203*K*, besides the main reflexes a satellite with $d = 1.942 Å$, and Miller indices (4, 0, 4.5) emerges in between the (4, 0, 4) and (4, 0, 6) peaks. Further cooling down to $T = 180K$ leads to the tripling the number of satellites. Positions of these satellites with $d_{hkl} = 1.768 Å$, $1.796 Å$, $1.928 Å$ relate fairly well with the calculated positions of the satellites with $d_{4,0.5,5} = 1.759 Å$, $d_{405.25} = 1.799 Å$ and $d_{404.75} = 1.926 Å$, respectively. At 100*K* (Fig.1) the intensities of the just-mentioned satellites become significantly increased and a satellite with $d_{404.5} = 1.883 Å$ appears in the intensity distribution. At last, at $T = 10K$ (Fig.2) the intensities of all the previous satellites become stronger again without positional change noticeable with the accuracy of the experiment. At the same time the (406) peak becomes approximately four times weaker in intensity. As follows from Fig. 1 and 2, the positions of the satellites are on the line that connects the (4, 0, 4) and (4, 0, 6) Bregg points.

With lowering the temperature, there also are some changes in the sector of the reciprocal space lying between [4, 0, 4], [4, 0, 6] directions. The peak having $d_{50.57.25} = 1.382 Å$ at 240*K* corresponds to the structure with modulation wave vector $\vec{q} = (0, q_y, 0.25)$ and $q_y \approx 0.5$. At 203*K* this peak disappears indicating the change of the modulation vector. At 180*K* already two peaks, with $d = 1.383 Å$ and $1.488 Å$, respectively, appear in the above zone. Their intensities decrease as temperature goes down to $T = 100K$. Further changes take place with lowering the temperature below 100K. At 10*K*, besides the already observed couple of peaks a third one appears, having the $d = 1.099 Å$.

In the cross-section (*hol*) the reflex (00*l*) relative intensities are temperature independent. There is no additional diffraction peaks in the zone $\Delta k \approx 0.5$ at temperatures 240*K* and 210*K*. At 180*K* a solitary weak peak emerges in the neutronogram remaining unchanged upon further decreasing the temperature. As temperature comes down to 10*K* one more additional peak appears. In the neighborhood of (*h*,0,0) peaks the temperature reduction effect can be easily made out only at 10*K* in the form of the significantly increased intensity of the (8, 0, 0) peak. Besides this, the (16, 0, 0) feflection becomes slightly observable at 100*K* and 10*K*. In this zone with $\Delta k \approx 0.5$ the additional peak appears first only at 180*K*. At 100*K* the number of the additional peaks triples and at 10*K* the intensities of these peaks is weakened.

To overall, we have shown that $TlInS_2$ crystals, which have an average space group of symmetry C_{2h}^6 in high-temperature phase, at $T = 240K$ are in incommensurate state with modulation wave vector $\vec{q}_{inc} = (q_x, q_y, 0.25)$. The parameters q_x and q_y exhibit significant temperature dependence. Within experimental accuracy these parameters do not exceed 0.005 at 203*K*. The magnitude of the third component does not change in the entire range of the accessed temperatures. According to the obtained data the $TlInS_2$ compound is in incommensurate phase already at 240*K*. The modulation wave vector is $\vec{q} = (0, q_y, q_z)$ and q_y is a strongly temperature dependent parameter ($q_y(T = 240K) \propto 0.5$, $q_y(T = 203K) \propto 0$). At the same time, the q_z is practically temperature independent. It seems important to figure out that the obtained neutron-scattering data are unambiguous about the successive structural changes and the modulation wave vector rotation with decreasing the temperature. These results permit the possibility of incommensurate-incommensurate phase transition and two-dimensionally modulated incommensurate phase on the phase diagram of $TlInS_2$. However, the results of the presented theoretical results on $TlInS_2$ require further experimental efforts, especially structural investigations in more detail.

Literature:

1. Vakhrushev S.B. Incommensurate phase transition in $TlInS_2$ crystal, JETP Letters, 1984, v.39, No. 6, pp. 245-247.

2. Kashida S., Kobayashi Y. X-ray study of the incommensurate phase of $TlInS_2$, J. Phys.: Condensed Matter, 1999, v.11, pp. 1027-1035.

3. Henkel W. High-pressure Raman study of the ternary chalcogenides $TlGaS_2, TlGaSe_2, TlInS_2 and TlInSe_2$, Phys. Rev. B, v.26, No.6, pp. 3211-3221.

4. Gashimzade F.M., Gadjiev B.R. Dielectric permittivity in incommensurate phase of $TlGaSe_2$, FTT, 1985, v.27, No.8, pp.2286-2290.

5. Gadjiev B.R., Seidov Yu. M. Incommensurate-incommensurate transition in subsuquant phase transitions in layered $TlInS_2$, ФТТ, 1996, т. 38, в.1, с. 3-13.

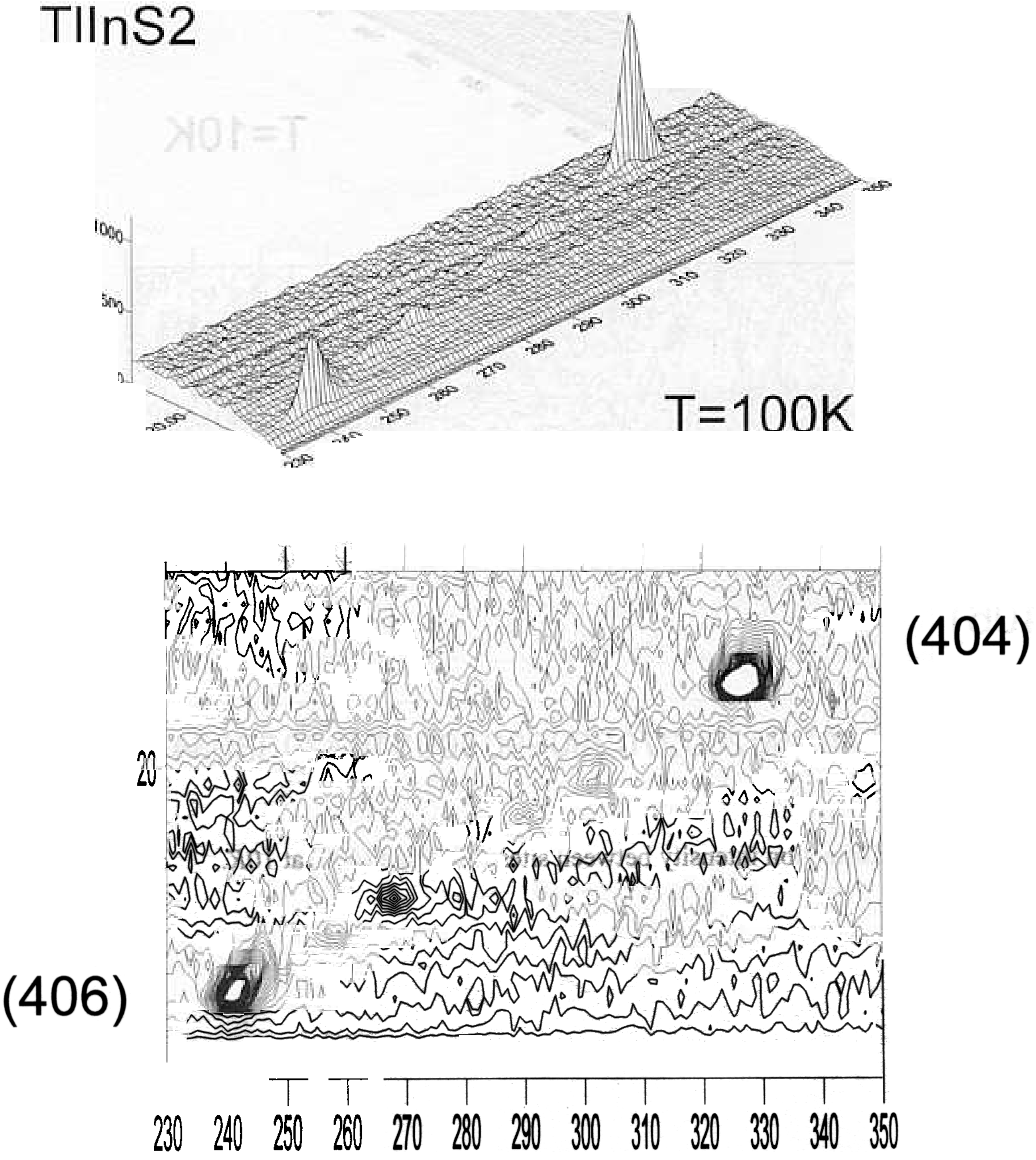

Fig.1 Maps of diffraction intensity between sites (404) and (406) at 100K

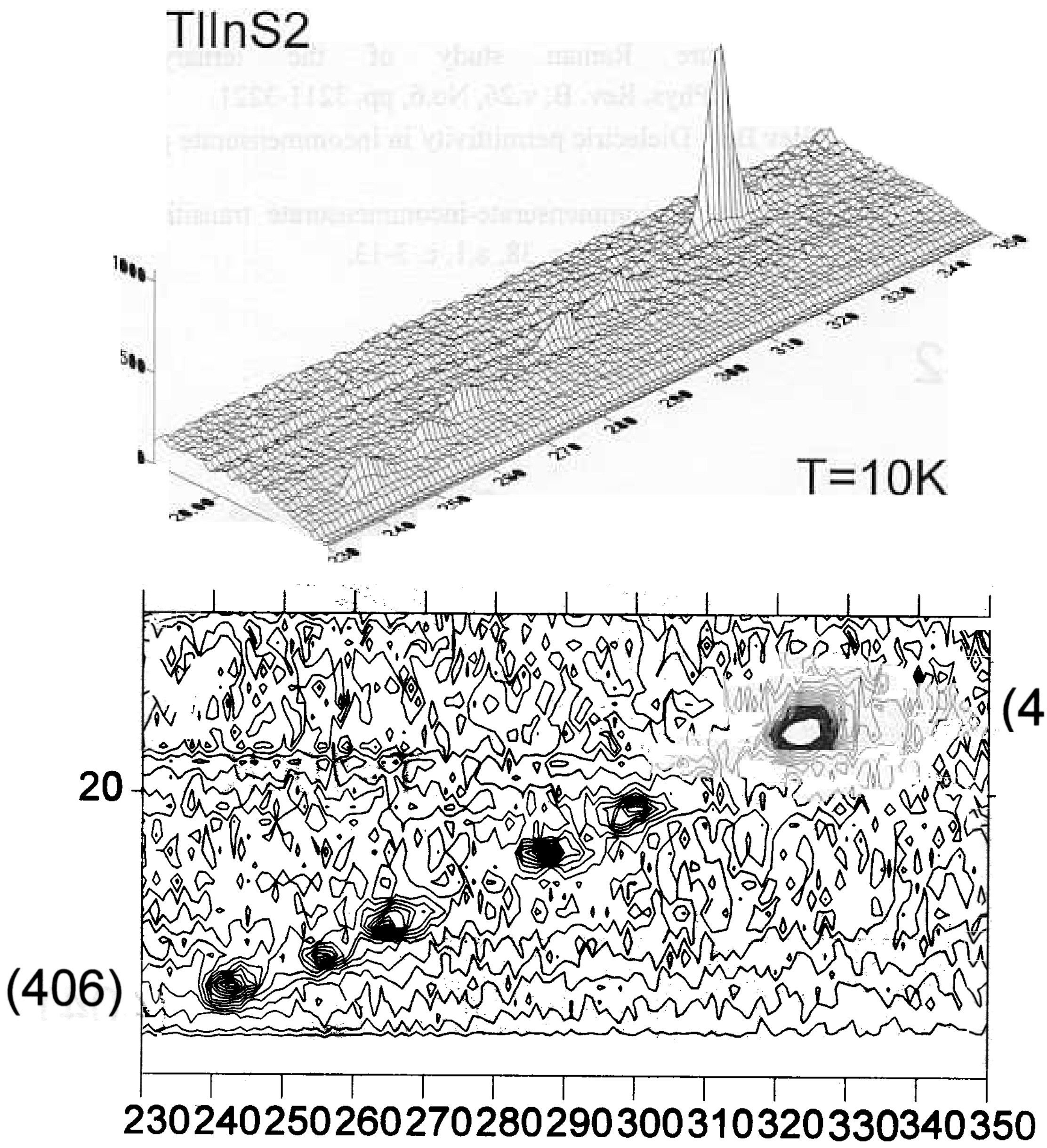

Fig.2. Maps of diffraction intensity between sites (404) and (406) at 10*K*.

Neutron diffraction study of the strain/stress behaviour on dolomite rock

Ch. Scheffzük [1,2], K. Walther[1], A. Frischbutter[1] and R.A. Zhukov [3]
[1] *GeoForschungsZentrum Potsdam, Telegrafenberg, 14473 Potsdam, Germany*
[2] *FLNP, Joint Institute for Nuclear Research, 141980 Dubna, Russia*
[3] *Tula State University, 300 600 Tula, Russia*

Introduction and sample orientation

Diffraction methods for strain/stress studies are well established in materials sciences [1]. Only recently geological materials became the subject of strain/stress investigations using diffraction methods. However, the study of geological problems is more complicated. One reason is the diversity of fabric elements, influencing the strain/stress properties of rocks, e.g. its polyphase composition, the occurrence of various macro- and microstructures like foliations, bedding planes, joints and crystallographic preferred orientations. Even the deformation history of rocks, which is often characterized by repeated superimposed deformation events accompanied by temperature and/or pressure is of importance. Consequently, the deformation history and the deformation parameters of geological materials are mostly unknown. In contrast to X-rays, neutron diffraction allows investigation of large sample volumes (several cm^3) due to the high penetration depth of neutrons. First experiments were carried out on sandstone using angle dispersive neutron diffraction as well as time-of-flight neutron diffraction in order to investigate applied and residual stresses [2]. Fundamental investigations of the strain/stress behaviour using diffraction methods in the laboratory - combined with microstructural investigations using optical and electron microscopy - are essential for a better understanding of rock mechanics.

The investigation of the strain-stress behaviour of monomineralic natural dolomite under uniaxial applied stress by neutron time-of-flight diffraction is the subject of this study. Next to calcite, the trigonal-rhombohedral $(\bar{3})$ dolomite ($CaMg(CO_3)_2$) is the most important rock forming mineral in carbonate rocks. The dominating morphological lattice planes are the rhombohedrons $\{10\bar{1}1\}$, special forms are pinacoids $\{0001\}$ and hexagonal prisms $\{hki0\}$. In contrast to calcite, which under load is twinning on *e*-planes $\{01\bar{1}2\}$, the most important twin plane of dolomite is the *f*-plane $\{02\bar{2}1\}$. The deformation mechanisms are described in [3] in more detail.

The sample (G3) was prepared from a core (⌀ 60 mm, depth: 1018 m below surface level) of borehole GUBEN 16/64 in the Niederlausitz (Germany). The sample is a grey, massive, oolithic dolomite, weakly developped flaser-bedding is indicated by thin layers of fine-grained, massive dolomite. The diameter of the ooids approximates 1 mm, most ooids are perfectly concentric. Only within a few distinct layers (thicknesses: several mm) the ooids are flattened, obviously due to the overburden pressure of the surface rock. Individual sparritic dolomite crystals embedded in a micritic dolomite matrix form the matrix between the ooids. The nuclei of the ooids are sometimes filled with dolomite monocrystals, too. The ooids itself consist of concentrically arranged layers of micritic dolomite-felt. Under the microscope, relics of muscovite and quartz can be detected, embedded within the matrix and enclosed within ooids as well. The mineralogical composition of the sample was determined by quantitative X-ray phase analysis: 92% dolomite, 3% quartz and accessory phases. All these observations indicate synsedimentary deformation and subsequent diagenetic recrystallization.

Experimental setup, sample preparation and results

For the experiments we used a sample cylinder (⌀=30 mm, l=60 mm). For d_0-determination, powder was prepared from the same sample (grain size ≤ 64 μm), heated for 24 h up to 400°C and slowly cooled down to room temperature. The experiments were carried out at room temperature at the diffractometer Epsilon at beamline 7A of the pulsed reator IBR-2 at JINR Dubna. Due to the long flight path of 102.38 m a rather good spectral resolution of 4×10^{-4} is achieved. The diffractometer is equipped with the uniaxial pressure device Exstress, which is able to apply loads up to 100 kN under *in situ* conditions. Stresses up to 150 MPa are applicable for the actual sample dimensions.

The neutron-TOF-pattern (Fig. 1), normalized with respect to the energy distribution, was measured with a time channel width of 32 μs. Taking into account the asymmetry of the diffraction peaks two superposed Gaussians with different half widths were used for the peak fit procedure [4]. The FWHM of the (0006) peak is in the order of 36 time channels, the $(10\bar{1}4)$ peak comprises about 27 channels, the $(11\bar{2}3)$ peak about 20 channels. Strain/stress experiments were carried out in four steps up to 45 MPa. Each loading state for applied stress measurement was interrupted by a stress-free state for residual strain measurements. The peak positions of all three lattice planes obviously change with different intensity towards lower time channels with increasing load (Fig. 2). Determining the corresponding values of the Young's modulus by linear regression, we obtained 101 GPa for the $(11\bar{2}3)$ reflection, 63 GPa for the (0006) reflection and 292 GPa for the $(10\bar{1}4)$ reflection.

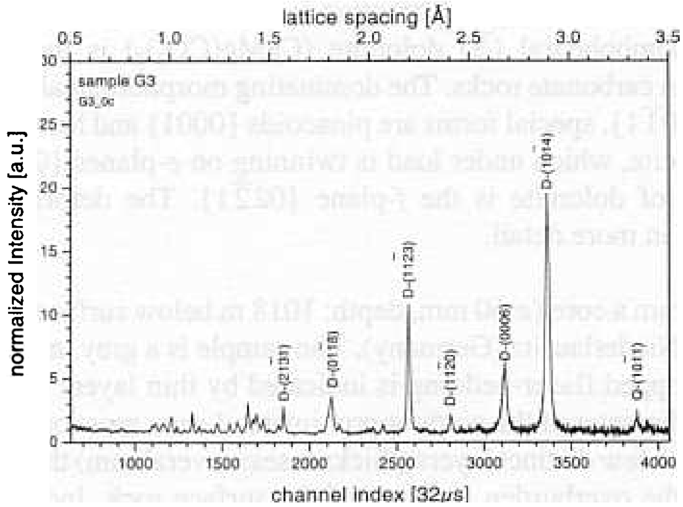

Fig. 1: Neutron time-of-flight diffraction pattern of the dolomite sample investigated.

The patterns determined at the relaxed positions of the sample are similar regarding the behaviour of the three reflections. Differences are valid only in scale (Fig. 3). This evolution is restricted to less than one time channel for the $(11\bar{2}3)$ and $(10\bar{1}4)$ reflections.

Nevertheless, all considered lattice planes indicate the same gap of compressive pseudostrain by a period of extension (stage 2). Assuming that the virginal state (◆ in Fig. 3) of the sample is more or less stress-free, the strain of the relaxed states of the sample was calculated using the virginal state as d_0. There are only weak changes regarding the evolution of the FWHM during the deformation experiment. This is demonstrated on behalf of the $(11\bar{2}3)$ peak, which is free of superimpositions. The FWHM of the $(11\bar{2}3)$ peak only slightly increases with increasing load.

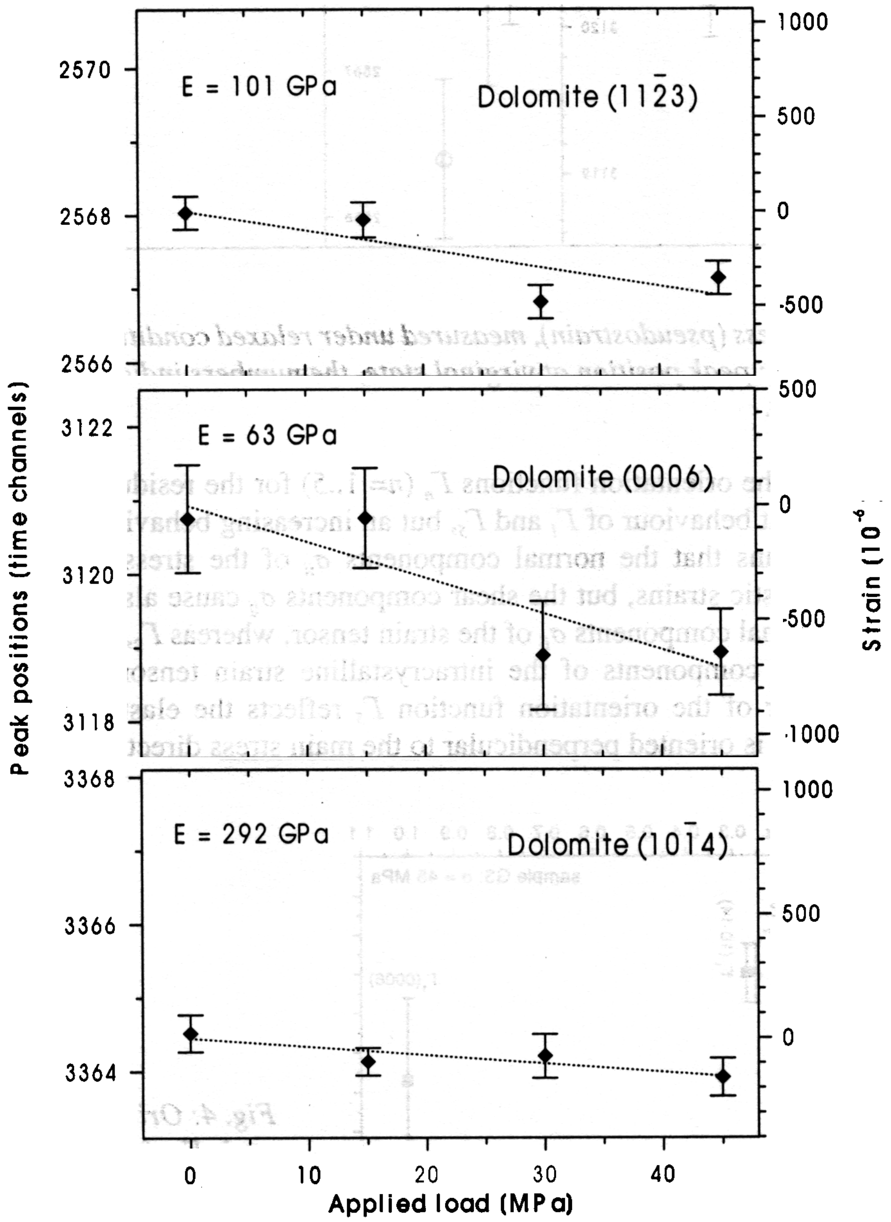

Fig. 2: Strain-stress relation for the $(11\bar{2}3)$, (0006) and $(10\bar{1}4)$ Bragg reflections of dolomite (sample G3), measured by stepwise increase of applied load. The Young's modul are enclosed.

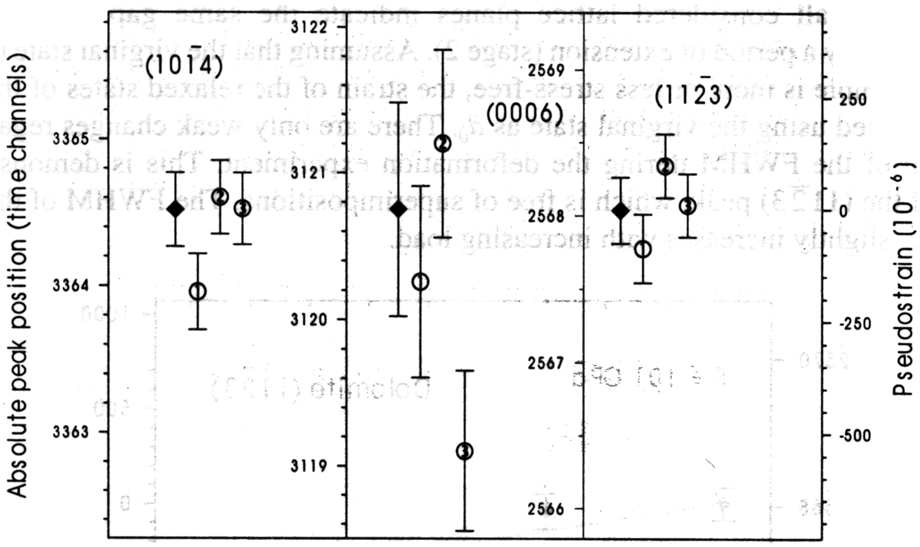

Fig. 3: Residual stress (pseudostrain), measured under relaxed conditions after each state of applied load. (♦: peak position at virginal state, the numbers indicate the order of the state of relaxation).

By calculation of the orientation functions Γ_n (n= 1..5) for the residual strain values we observed a constant behaviour of Γ_1 and Γ_5, but an increasing behaviour of Γ_2, Γ_3 and Γ_4 (Fig. 4). This means that the normal components σ_{ii} of the stress tensor cause only intracrystalline elastic strains, but the shear components σ_{ij} cause also plastic strains. Γ_1 represents the normal components σ_{ii} of the strain tensor, whereas Γ_2, Γ_3 and Γ_4 represent elastic and plastic components of the intracrystalline strain tensor. Furthermore, the constant behaviour of the orientation function Γ_5 reflects the elastic character in the direction σ_3, which is oriented perpendicular to the main stress direction σ_1.

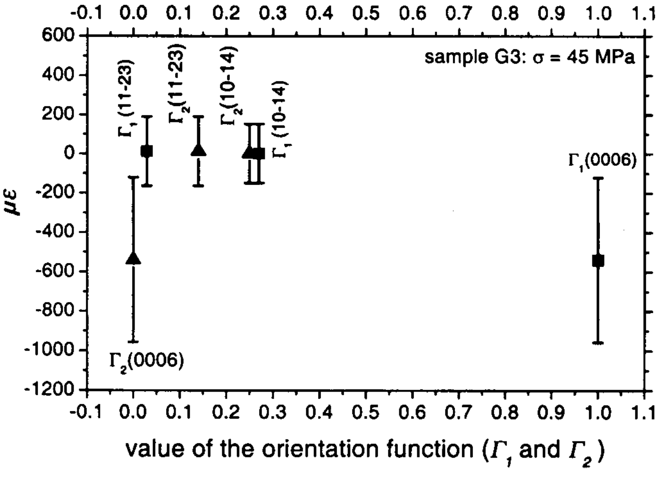

Fig. 4: Orientation functions Γ_1 and Γ_2 for residual stress values of the dolomite sample G3.

Discussion

Our results indicate that neutron time-of-flight diffraction is a useful tool for *in situ* experiments concerning the strain/stress behaviour and residual stress measurements on dolomite rocks. The actual experimental set up allows us to make use of only two dolomite reflections for strain/stress studies: $(11\bar{2}3)$ and $(10\bar{1}4)$, because other reflections are either weak (measuring time), superposed or out of range. The Young's modulus, determined from the strain-stress curve for the dolomite $(11\bar{2}3)$ reflection, agrees well with published data for isotropic polycrystalline aggregates [5], but disagrees with published values for the dolomite (0006)- and $(10\bar{1}4)$-reflections. The discrepancy may arise from the entirety of macro- and microstructural features of the studied sample, from the superimposition of diffraction peaks and from resulting complications in data analysis.

The work has been founded by the German BMBF (projects DUBPOT-3 and DUBPOT-9). We gratefully acknowledge further support of FLNP/JINR Dubna and GeoForschungsZentrum Potsdam.

REFERENCES

1. M.T. Hutchings and A.D. Krawitz (Eds.), Measurement of Residual and Applied Stress Using Neutron Diffraction. NATO ASI Series **E216**: 588 p. (1992).
2. A. Frischbutter, D. Neov, Ch. Scheffzük, M. Vrana and K. Walther, Lattice strain measurements on sandstones under load using neutron diffraction. *J. Struct. Geol.* **22** (11/12), 1587-1600 (2000).
3. D.J. Barber, H.C. Heard and H.-R. Wenk, Deformation of dolomite single crystals from 20-800°C. *Phys. Chem. Minerals* **7**, 271-286 (1981).
4. K. Walther, Ch. Scheffzük and A. Frischbutter, Strain-stress-experiments on dolomite using neutron TOF diffraction. *Physika semli*, in preparation.
5. K.H. Hellwege, Landolt-Börnstein - Zahlenwerte und Funktionen aus Naturwissenschaften und Technik. - Neue Serie, Band 1b: Physikalische Eigenschaften der Gesteine. [Springer Verlag Berlin, Heidelberg, New York: 604 p., 1982].

TEXTURE – AN INDICATOR OF ROCK METAMORPHISM AND DEFORMATION PROCESSES IN THE CONTINENTAL CRUST

A.N. Nikitin[a], T.I. Ivankina[a], N.V. Zamyatina[a], V.I. Kazansky[b], K.V. Lobanov[b] and A.V. Zharikov[b]

[a] *Joint Institute of Nuclear Research, Frank Laboratory for Neutron Physics,*
141980, Dubna, Russia
[b] *Institute of Geology of Ore Deposits, Petrography, Mineralogy and Geochemistry, Russian*
Academy of Sciences, 109017, Moscow, Russia

Introduction

Crystallographic preferred orientation (texture) of rock-forming minerals is the main controlling factor of rock anisotropy, among other factors like shape preferred orientation and microcracks. Textures can produce pronounced directional dependence of elastic properties. Hence, texture determinations contain information on the seismic anisotropy and can be helpful to understand the nature of seismic boundaries in the continental crust. Texture measurements of naturally deformed rocks combined with the results of deep seismic sounding may allow reconstruction of the paleotectonic stress state at deep crustal levels. Texture analyses give us a key for the understanding of texture development and, consequently, for the restoration of geological evolution processes.

In this paper we report results of texture determinations carried out on core samples from the Kola superdeep borehole SG-3 and their surface analogues. These measurements carry on earlier texture and anisotropy investigation of deep crustal rocks [1] and will be useful for the geodynamic modelling [1] of the crustal structure at the Pechenga ore region (Kola Peninsula) [2].

Sample description

The core samples were collected from selected sections of the SG-3 core distance (8.5 – 11.5 km). The surface analogues were collected about 50 km northeast from the SG-3 drilling site in a reference area located south from the Mustatuntury ridge. The core and surface samples (two gneisses, four amphibolites) are characterized by identical mineralogical and chemical composition and mineral density. The average mineralogical composition of the core samples (black bars) and surface samples (white bars) are presented in Fig. 1.

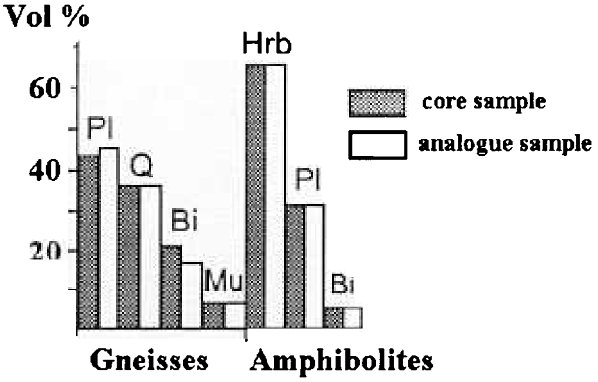

Fig. 1. Mineralogical composition of Kola rock samples:
Pl – plagioclase, **Q** – quartz,
Bi – biotite, **Mu** – muscovite,
Hrb – hornblende.

The experiments were performed on cubic samples with 30 mm edge length. The sample reference system corresponds to the geographical coordinates (azimuth and declination).

Experiment and results

Texture measurements have been carried out at the neutron texture diffractometer SKAT at the pulsed reactor IBR-2. The measuring time for the each sample was 36 hours, the exposition time at one sample position was 30 min. As an example, the time-of-flight diffraction pattern of the core gneiss sample K9002 is shown in Fig.2. The K9002 sample constitutes of plagioclase – 55%, quartz – 26%, biotite and muscovite– 16%, additional minerals – 3%.

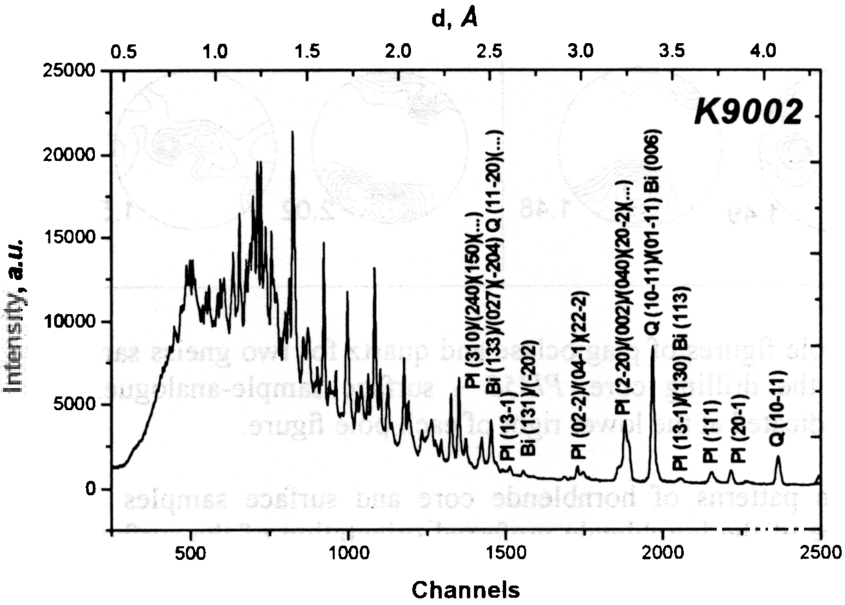

Fig. 2. Diffraction pattern of sample K9002. Some Bragg reflections as well as the overlapping conditions are indicated. Pl – plagioclase, Q – quartz, Bi – biotite.

Since the samples consist of low symmetrical minerals, texture analysis of such polyphase rock is not trivial due to complex diffraction patterns with many overlapping peaks. Nevertheless, a sufficient number of plagioclase and quartz pole figures (for gneisses) and hornblende and plagioclase pole figures (for amphibolites) could be extracted from the diffraction spectra. Since counting statistics of biotite and muscovite reflections are insufficient, pole figures for these mineral phases were not extracted from the diffraction pattern.

Based on the experimental pole figures, the orientation distribution functions (ODF`s) and pole figures of the main crystallographic planes (100), (010) and (001) of the predominant mineral phases have been calculated. The results of texture analysis display a well developed textures of all mineral phases.

In the gneiss samples preferred orientation patterns of plagioclase are more pronounced compared to the quartz patterns. Pole figures of the plagioclase crystallographic planes (001), (010), (100) of core sample *K9002* and its surface analogue *Pl358* are shown on Fig. 3. It was observed that patterns of both samples are similar, but the degree of preferred orientations of sample *Pl358* is weaker compared to sample *K9002*.

Fig. 4 displays pole figures of two amphibolite samples: *K8933* - selected from the drilling core SG-3 and *Pl356* – the surface equivalent. It is obvious, that the prevailing rock forming mineral hornblende (65-70 %) possesses the more pronounced stronger preferred orientations compared to plagioclase textures. The texture of quartz could not be calculated because of the low volume fraction (~ 4 %) of this mineral.

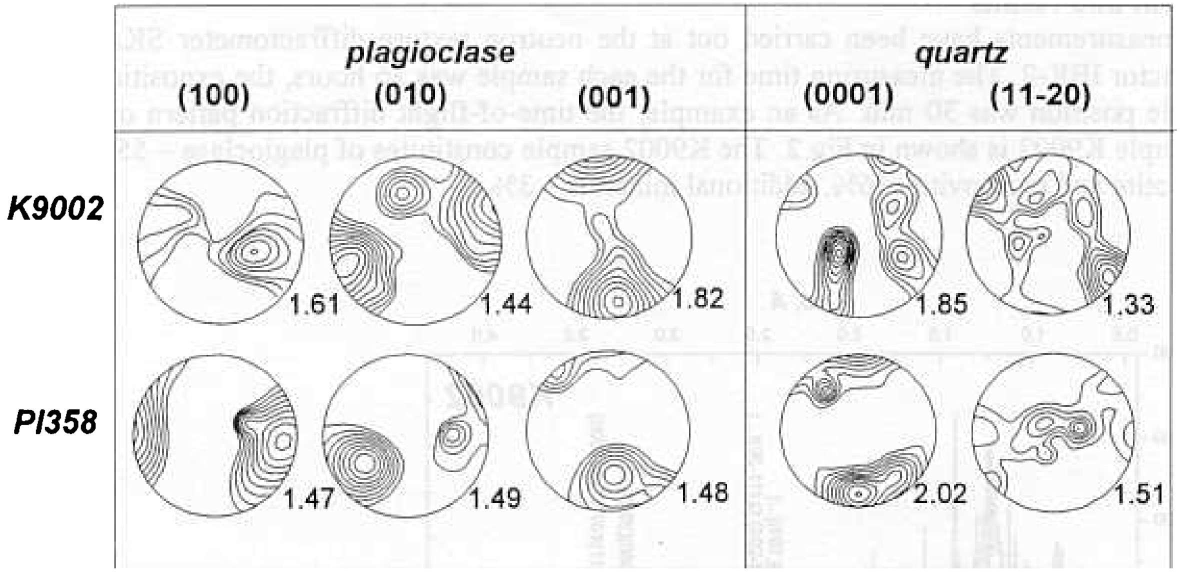

Fig. 3. ODF - derived pole figures of plagioclase and quartz for two gneiss samples: *K9002* – gained from the drilling core, *Pl358* – surface sample-analogue. The maximum intensity is indicated at the lower right of each pole figure.

The preferred orientation patterns of hornblende core and surface samples as well are comparable. However, the degree of the hornblende preferred orientation of the surface sample is higher compared to the core sample. In the case of plagioclase, differences in the preferred orientation of core and surface sample is not so clear as for the hornblende textures.

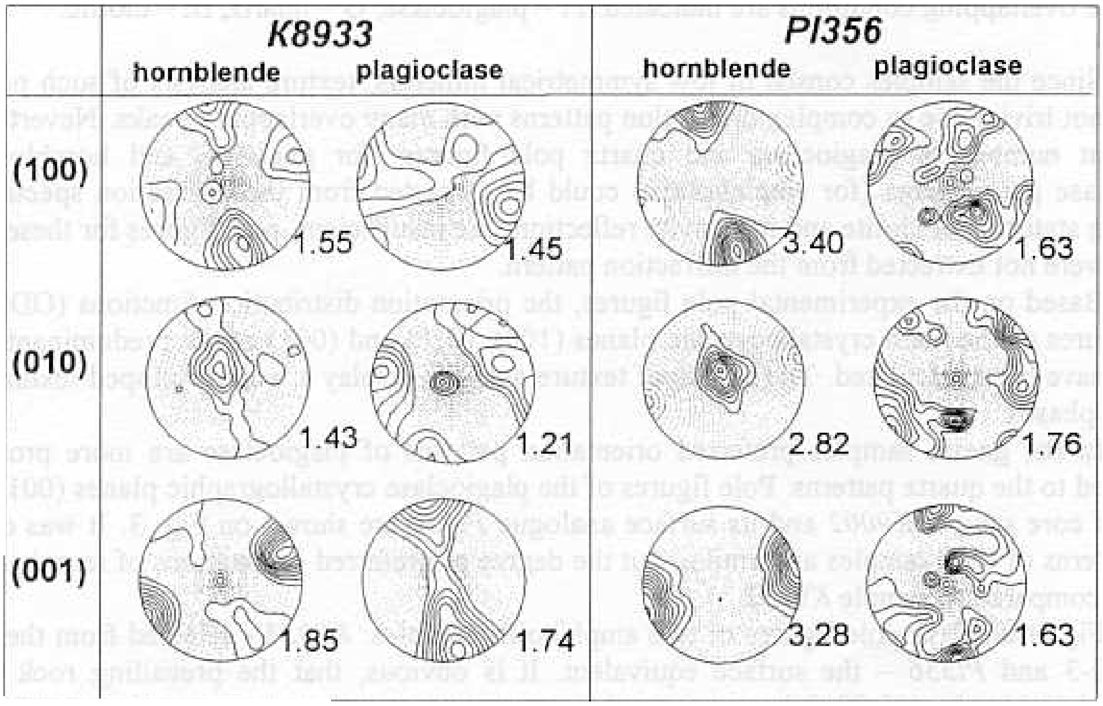

Fig. 4. ODF - derived pole figures of hornblende and plagioclase for two amphibolite samples: *K8933* – gained from the drilling core, *Pl356* – surface sample-analogue. The maximum intensity is indicated at the lower right of each pole figure.

Comparing the plagioclase pole figures (gneisses and amphibolites as well) from different levels of the SG-3 section, it can be found that plagiogneisse K9002 and amphibolite K8933, belonging to the allocated section, are characterised by identical patterns. It should be also noted that texture formation took place of about 550-630°C (amphibolite metamorphic facies), as indicated by plagioclase-hornblende geothermometer. This represents an additional forcible evidence for analogy between the samples collected from the Kola SG-3 and Mustatunturi area.

Acknowledgements
This study has been performed in the framework of the UNESCO International Geological Correlation Programme (Project 408) and with financial support from the Russian Foundation for Basic Research (Project № 00-05-64244).

References

[1] Nikitin A.N., Ivankina T.I., Ullemeyer K., Locajicek T., Pros Z., Klima K., Smirnov Yu.P., Kusnetzov Yu.I. Texture controlled elastic anisotropy of amphibolites from the Kola superdeep borehole Sg-3 at high pressure. Fizika Zemli. **1** (2001)

[2] Three-dimensional models and geodynamics of the Pechenga ore region and adjacent areas. In: Kola Superdeep. Scientific Results and Research Experience. M.: TECHNONEFTEGAZ, 130-155 (1998)

STRUCTURAL STUDY OF TERNARY MERCURY CHALCOGENIDE SYSTEMS $HgSe_{1-x}S_x$ (x=0.3, 0.5, 0.6) UNDER HIGH PRESSURE

V.I.Voronin[1], V.P.Glazkov[2], D.P.Kozlenko[3], S.V.Tikhomirov[3], B.N.Savenko[3]
I.F.Berger[4], V.V.Shchennikov[1]

[1] *Institute for Metal Physics, RAS, Ural Division, 620219 Ekaterinburg, Russia*
[2] *Russian Research Center "Kurchatov Institute", 123182 Moscow, Russia*
[3] *Frank Laboratory of Neutron Physics, JINR, 141980 Dubna Moscow Reg, Russia*
[4] *Institute of Solid State Chemistry, RAS, Ural Division, 620219 Ekaterinburg, Russia*

Mercury chalcogenides HgX (X=O, S, Se, Te) attract great deal of attention due to a number of pressure-induced phase transitions accompanied by the changes in electronic structure [1]. Structures of binary systems HgSe and HgS under high pressure have been extensively studied by X-ray diffraction [2-4]. HgS (the cinnabar) at ambient conditions has a hexagonal structure, space group $P3_121$ (the cinnabar phase). This phase is characterized by spiral atomic chains, parallel to c-axis. HgSe at ambient conditions has a zinc blende cubic structure, space group $F\bar{4}3m$. Under pressure HgSe converts to the cinnabar phase at $P \sim 10$ kbar [2]. Both HgS at $P \sim 130$ kbar and HgSe at $P \sim 200$ kbar transform to NaCl-type cubic structure, space group *Fm3m* [4]. At higher pressures ($P \sim 400$ kbar) HgSe transform to orthorhombic structure, space group *Cmcm*.

An effect of high pressure on the structure of ternary systems $HgSe_{1-x}S_x$ have not been studied yet. One may expect that these compounds will undergo a sequence of the phase transitions similar to that for pure HgS or HgSe. In [6] it was found that electrical resistance of $HgSe_{1-x}S_x$ systems ($0.1 < x < 0.6$) increases rapidly in 2-3 orders of magnitude at pressure $P \sim 4 - 8$ kbar depending of S content. This effect was attributed to a semimetal-semiconductor electronic transition and it was suggested that this change of electrical resistance corresponds to the structural phase transition from cubic zinc-blende phase to cinnabar hexagonal phase. At $P \sim$ 100-150 kbar the decrease of electrical resistance of $HgSe_{1-x}S_x$ compounds was observed [7]. This effect may correspond to semiconductor-metal electronic transition and it was suggested that it is accompanied by a structural phase transition to NaCl-type cubic phase.

To study structural changes in ternary mercury chalcogenide systems $HgSe_{1-x}S_x$ (x = 0.3, 0.5, 0.6), neutron diffraction experiments have been performed with the DN-12 spectrometer at pressures up to 30 kbar and ambient temperature using sapphire anvil high pressure cells. The scattering angle was $2\theta = 90°$.

Diffraction patterns of $HgSe_{0.7}S_{0.3}$ measured with the DN-12 spectrometer at $P = 0$ and 17 kbar are shown in fig. 1. Diffraction patterns of $HgSe_{0.5}S_{0.5}$ and $HgSe_{0.4}S_{0.6}$ look similar. For all the investigated systems a phase transition from the cubic zinc-blende phase to the hexagonal cinnabar phase was observed at $P \sim 10$ kbar in agreement with electrical resistance measurements [6]. In the high pressure cinnabar phase Hg atoms occupy 3*a* sites (*u*, 0, 1/3) and Se/S atoms occupy 3*b* sites (*v*, 0, 5/6) of the space group $P3_121$ with $u = 0.72(1)$ and $v = 0.47(1)$. As a result of the phase transition, the unit cell volume per molecular unit undergoes a jump with relative volume reduction of $\Delta V/V \sim 12$ %. From diffraction data lattice parameters and interatomic distances as functions of pressure were obtained. Lattice parameters *a* and *c* as functions of pressure for the cinnabar high pressure phase of $HgSe_{1-x}S_x$ systems (x=0.3, 0.5, 0.6) are shown in fig. 2.

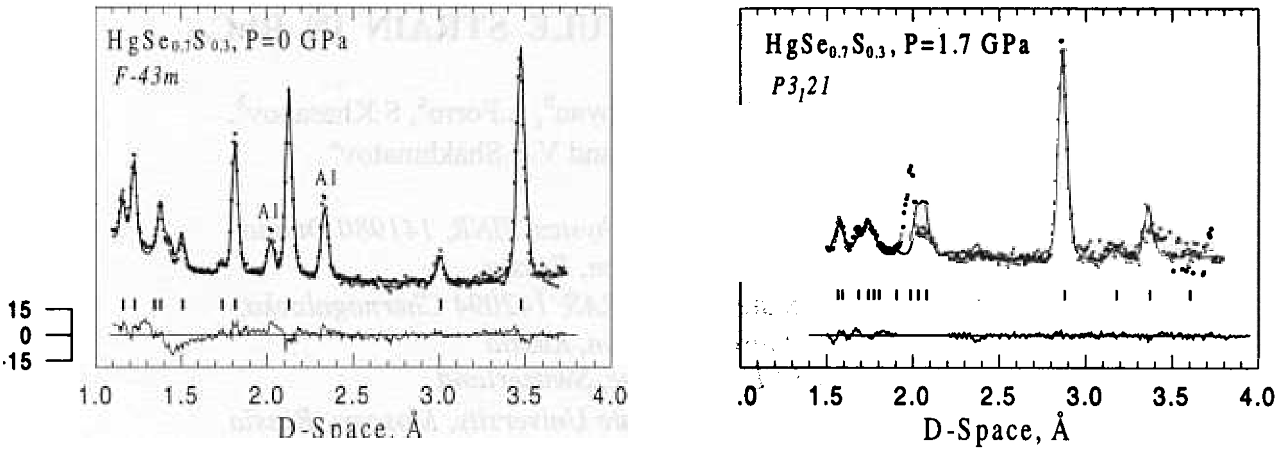

***Figure 1.** Diffraction patterns of $HgSe_{0.7}S_{0.3}$, measured with the DN-12 spectrometer at P=0 (zinc blende cubic phase) and P=17 kbar (hexagonal cinnabar phase) and processed by the Rietveld method.*

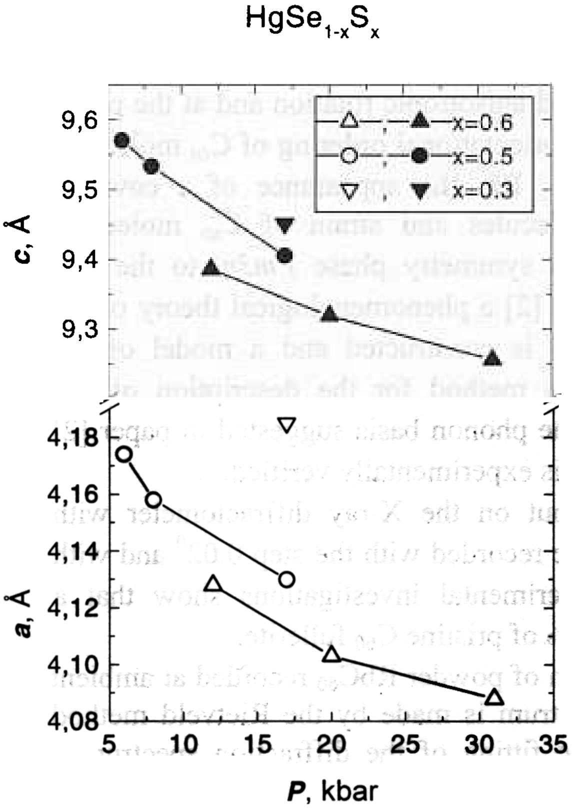

***Figure 2.** Lattice parameters a and c as functions of pressure for the cinnabar high pressure phase of $HgSe_{1-x}S_x$ systems (x=0.3, 0.5, 0.6).*

The work has been supported by Russian Foundation for Basic Research, grant № 00-02-17199.

1. I.M.Tsidilkovsky, V.V.Schennikov, I.G.Gluzman, Soviet Phys. of Soild State, 24, 2658 (1982).
2. M.I.McMahon, R.J.Nelmes, Phys. Stat. Sol. (b) 198, 389 (1996).
3. A.Werner, H.D.Hocheimer and K.Strössner, Phys. Rev. B 28, 3330 (1983).
4. T.L. Huang and A.L.Ruoff, Phys. Rev. B 31, 5976 (1985).
5. N.G.Wright, M.I.McMahon, R.J.Nelmes, A.San-Miguel, Phys. Rev. B 48, 13111 (1993).
6. V.V.Shchennikov, N.P.Gavaleshko, V.M.Farsunyak, V.I.Osotov, Soviet Physics of Solid State, 37, 2398 (1995).
7. V.V.Shchennikov, N.P.Gavaleshko, V.M.Farsunyak, Soviet Physics of Solid State, 35, 389 (1993).

FULLERENE MOLECULE STRAIN IN RbC$_{60}$

V.L.Aksenov[a], Yu.A.Ossipyan[b], L.Forro[c], S.Khasanov[b],
V.V.Chernyshev[d] and V.S.Shakhmatov[a]

[a] *Frank Laboratory of Neutron Physics, JINR, 141980 Dubna,*
Moscow Region, Russia
[b] *Institute of Solid State Physics RAS, 142094 Chernogolovka,*
Moscow Region, Russia
[c] *EPFL, Lausanne, Switzerland*
[d] *Lomonosov Moscow State University, Moscow, Russia*

Strain displacements of carbon atoms in a C$_{60}$ molecule in the *Pnnm* phase of the RbC$_{60}$ fulleride are first determined by X-ray diffraction. The measurements show that the polymeric bond length between carbon atoms of two nearest molecules C$_{60}$ is equal to 1.69 (1) Å, the rotation angle of the molecule about the polymeric direction is 47.0(3)^0 [1].

In most fullerene crystals, orientational phase transitions are observed. At high temperatures, C$_{60}$ molecules experience retarded anisotropic rotation and at the phase transition temperature, the rotation ceases and orientational ordering of C$_{60}$ molecules takes place. In AC$_{60}$ fullerides, where A=K, Rb, the appearance of a covalent (polymeric) bonds between nearest C$_{60}$ molecules and strain of C$_{60}$ molecules following the phase transition from the high symmetry phase *Fm3m* to the low symmetry phase *Pnnm* are observed. In papers [2] a phenomenological theory of the structural phase transition in fullerides AC$_{60}$ is constructed and a model of the orientational phase transition together with a method for the description of C$_{60}$ molecule strain are proposed. In this article, the phonon basis suggested in paper [2] for the description of fullerene molecule strain is experimentally verified.

Structural investigations are carried out on the X-ray diffractometer with CuK$_{\alpha 1}$ radiation (λ =1.5406 Å). The spectra are recorded with the step 0.02^0 and with the fixed exposition time 30 sec. Our experimental investigations show that a polycrystalline sample of RbC$_{60}$ contains ~13 % of pristine C$_{60}$ fullerite.

In Fig. 1, the X-ray diffraction spectrum of powder RbC$_{60}$ recorded at ambient temperature is shown. The fitting of the spectrum is made by the Rietveld method using a modernized MRIA program. For the fitting of the diffraction spectrum a number of the models are used.

The results are following. On the basis of the symmetry theory [2] of fullerene molecule strain at the orientational phase transition in AC$_{60}$ crystals it is possible to obtain deformational displacements of carbon atoms in the C$_{60}$ molecule in diffraction experiments (see Fig. 2). Double bond lengths of strained C$_{60}$ molecule range from 1.37 Å to 1.55 Å and single bonds lie in the interval from 1.18 Å to 1.59 Å. The length of a broken double bond in the molecule is 1.55(2) Å and the distance between the carbon atoms of two nearest molecules is equal to 1.69(1) Å.

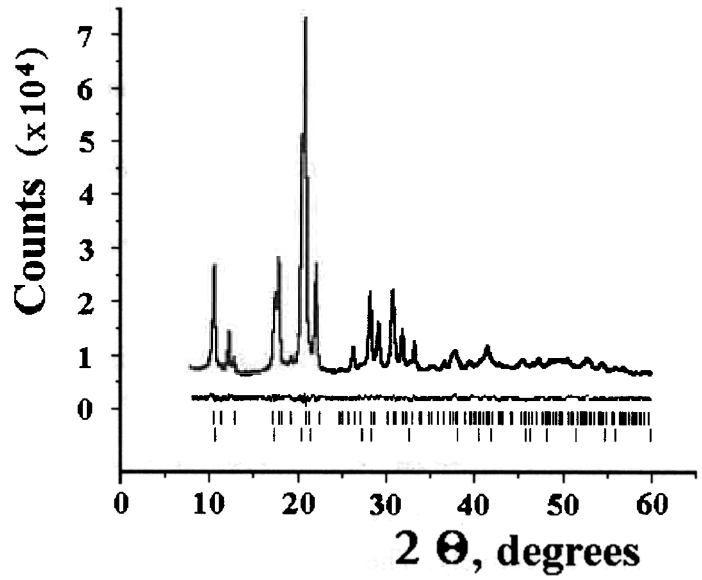

Fig. 1. The X-ray diffraction spectrum of RbC_{60} (and ~13 % of pristine C_{60}) at 300 K.

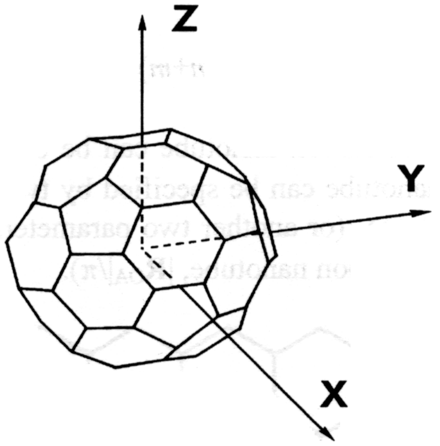

Fig. 2. The strain of C_{60} molecule of RbC_{60} fulleride in the polymer- like *Pnnm* phase.

The reported work has been performed under the auspices of the State Scientific and Technical Program «Fullerenes and Atomic Clusters», N20002.

References

1. Aksenov V.L., Ossipyan Yu.A., Forro L., Khasanov S., Chernyshev V.V., Shakhmatov V.S. Fullerene molecule strain in RbC_{60}, Physics Letters A, 2000, v.268, pp. 395-398.
2. Aksenov V.L., Ossipyan Yu.A., Shakhmatov V.S. *JETP Letters*, **64**, 120 (1996); *JETP*, **86**, 591 (1998).

SYMMETRY GROUPS OF CARBON NANOTUBES

V.L.Aksenov[a], Yu.A.Ossipyan[b] and V.S.Shakhmatov[a]

[a] *Frank Laboratory of Neutron Physics, JINR, 141980 Dubna, Moscow Region, Russia*
[b] *Institute of Solid State Physics RAS, 142094 Chernogolovka, Moscow Region, Russia*

The structure of carbon nanotubes of different types is investigated and the symmetry groups of them are proposed. A carbon nanotube of zigzag type, (n,0), where n- an integer number, has the D^1_{2nh} symmetry group or D^2_{2nh} group for odd or even n, respectively. Tubes of armchair type, (n,n), has also two groups, D^3_{2nh} and D^4_{2nh}, for odd or even n, respectively. The latter groups are isomorphic to previous ones but are different from them by the translation vector along axis of tube. A nanotube of general type (n,m) ($n>m$ and $m\neq 0$) has the symmetry group $D_N^{n',m'}$ if the number $N=2(n^2+m^2+nm)/(n-m)$ is an integer. The basic translation vector in this case is defined by the numbers n' and m' which comply the equation

$$n'(2n+m) + m'(n+2m)= 0.$$

The structure of carbon nanotube can be understood using a plane shown in Fig. 1. The carbon nanotube can be specified by two numbers n and m which define the vector $\mathbf{R}_{OA}= n\mathbf{a}_1+ m\mathbf{a}_2$ (or another two parameters, for example, the chiral angle, ψ, and the diameter of carbon nanotube, $|\mathbf{R}_{OA}|/\pi$).

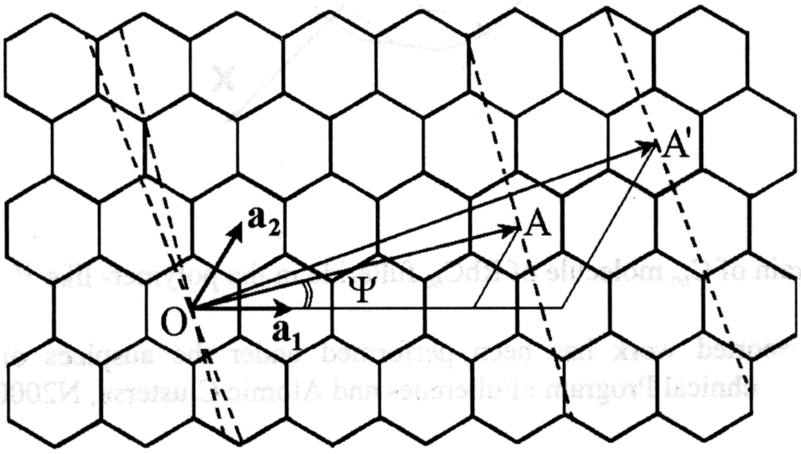

Fig. 1. A two-dimensional graphene sheet for construction of the carbon nanotubes. Carbon atoms are located at each vertex of the honeycomb cell. $\{\mathbf{a}_1,\mathbf{a}_2\}$ are the unit vectors of the hexagonal lattice. $\mathbf{R}_{OA}= 3\mathbf{a}_1+ 1\mathbf{a}_2$ defines the (3,1) nanotube and $\mathbf{R}_{OA'}= 4\mathbf{a}_1+ 2\mathbf{a}_2$ defines the (4,2) nanotube.

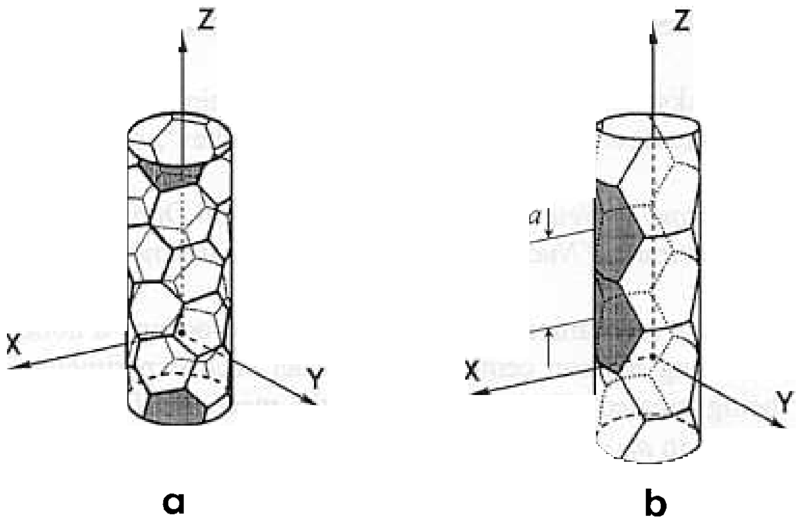

Fig. 2. a). The structure of (4,2) carbon nanotube. b). The structure of (2,2) carbon nanotube. The shaded hexagons are separated by the basic translation vector, **t** (|**t**|= *a*), along Z axis.

Two different carbon nanotubes are shown in Fig. 2. The symmetry elements of the (2,2) carbon nanotube are written as [1]

$$\{E, (C_4|\mathbf{t}/2), C_4^2, (C_4^3|\mathbf{t}/2)\}\otimes\{E, U_1, (U_2|\mathbf{t}/2), U_3, (U_4|\mathbf{t}/2)\}\otimes$$

$$\otimes\{E, I\}\otimes\{E, \mathbf{t},..., \mathbf{t}^k,...\},$$

where E is the identical element, $(C_4|\mathbf{t}/2)$, C_4^2 and $(C_4^3|\mathbf{t}/2)$ are the rotations about Z axis at 90^0, 180^0 and 270^0, respectively, $\mathbf{t}/2$ is the accompanied nonprimitive translation, $U_1,..., (U_4|\mathbf{t}/2)$ are the rotations at 180^0 about axes perpendicular Z axis, I is the inversion operation, **t** is the unit translation vector of one-dimensional subgroup of translations, the symbol ⊗ denotes direct production of subgroups. The proposed symbol of this group is D_{4h}^{4}.

For the (4,2) carbon nanotube the symmetry elements are following

$$\{E, (C_{28}|\tau), (C_{28}|\tau)^2,..., (C_{28}|\tau)^{27}\}\otimes\{E, U_1, (U_2|\tau),..., (U_{28}|\tau^{27})\}\otimes$$

$$\otimes\{E, \mathbf{t},..., \mathbf{t}^k,...\},$$

where $\tau = \mathbf{t}\sqrt{\frac{27}{28}}$. The symbol of this group is $D_{28}^{4,-5}$.

The work has been performed under the auspices of the State Scientific and Technical Program «Fullerenes and Atomic Clusters», N20002.

References

1. Aksenov V.L., Ossipyan Yu.A., Shakhmatov V.S. Symmetry groups of carbon nanotubes, Particles and Nuclei, Letters, N1[98]-2000, pp.44-47.

FOURIER STRESS DIFFRACTOMETER (FSD): FIRST RESULTS

G.D.Bokuchava[a], V.L.Aksenov[a], A.M.Balagurov[a], E.S.Kuzmin[a], A.V.Tamonov[a], V.V.Zhuk[a], V.V.Zhuravlev[a], V.A.Trounov[b], V.A.Kudrjashev[b], A.P.Bulkin[b]

[a] *Frank Laboratory of Neutron Physics, JINR, 141980 Dubna, Russia*
[b] *Petersburg Institute of Nuclear Physics, 188350 Gatchina, Russia*

Experiments to study mechanical internal stress start to occupy a noticeable position in the research programs of leading neutron centers. To conduct such experiments, specialized neutron diffractometers are being created. Such devices should meet the following requirements: high luminosity, high resolution in d_{hkl}-spacing, fixed scattering angles $2\theta=\pm 90°$, sufficiently wide range of d_{hkl}, specific sample environment (goniometers, collimators, loading devices, etc.). The experience of application of neutron diffraction to study residual stresses with the HRFD diffractometer in Dubna arouse much interest on the side of science and Russian industry [1, 2]. Therefore, the new project for the creation of a neutron diffractometer dedicated *exclusively* to residual stress studies started on beam №11a of the IBR-2 pulsed reactor in FLNP JINR. Channel 11 of IBR-2 is divided in two neutron beams: beam 11a for the FSD diffractometer and the ISOMER instrument for nuclear physics studies will be installed on beam 11b (fig. 1).

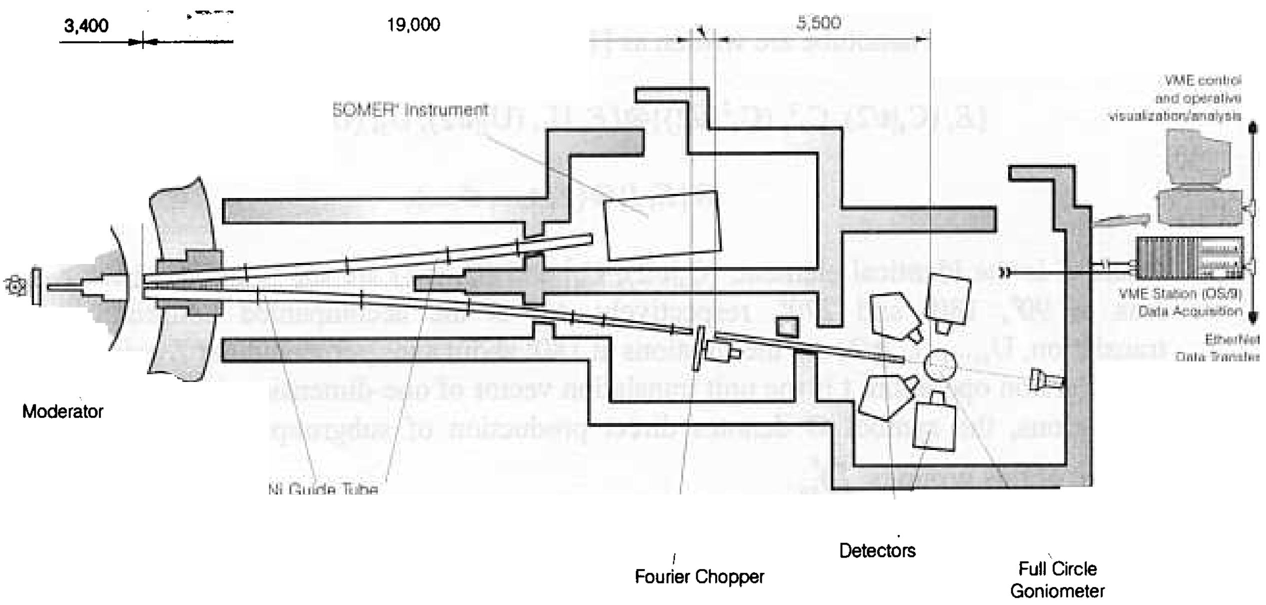

Fig. 1. The layout of the FSD diffractometer at the IBR-2 pulsed reactor.

After installing the mirror neutron guide produced in PNPI (Gatchina) the first test experiments on FSD were carried out in May, 1999: the vertical and horizontal profiles of the direct beam at the mirror neutron guide exit and at the sample site were investigated, the integral neutron flux at Fourier chopper site and at the neutron guide exit were estimated, the first diffraction spectra from standard samples in the low-resolution mode (usual time-of-flight regime without the Fourier chopper) were registered (fig. 2).

In November 1999 the Fourier chopper made in PNPI (Gatchina) was installed in FSD. One of the major parameters of the Fourier diffractometer using the correlation technique is the Fourier chopper contrast factor. With the help of the ^{3}He-detector at the scattering angle $2\theta\approx 90°$ neutron diffraction spectra from the standard sample Al_2O_3 in the low-resolution mode (usual time-of-flight regime) were measured at different positions of the Fourier chopper rotor. The dependence of the (210) diffraction peak integral intensity (d=2.086 Å) versus the rotor position x is shown in fig. 3. The Fourier chopper contrast factor was defined as R=max(I)/min(I) and the effectiveness factor

Q(R)=1-1/R, where I is the diffraction peak integral intensity The Fourier chopper contrast dependence on the wavelength is given in table 1.

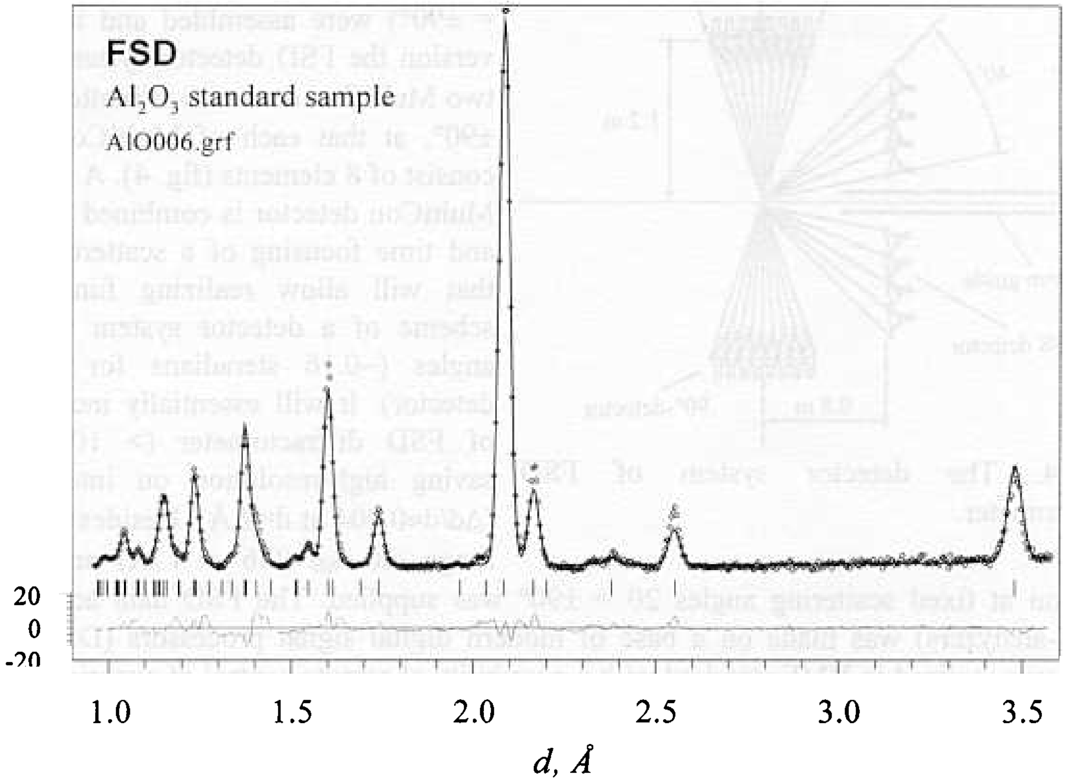

Fig. 2. Part of the neutron diffraction pattern from the Al_2O_3 standard sample measured on FSD in the low-resolution mode (usual time-of-flight regime without the Fourier chopper). The experimental points, the profile calculated by the Rietveld method and the difference curve are shown.

Table 1. The Fourier chopper contrast dependence on the wavelength.

d, Å	λ, Å	R	Q(R)
2.086	2.949	72.352	0.986
1.613	2.281	58.809	0.983
1.392	1.968	51.819	0.981
1.252	1.770	41.067	0.976

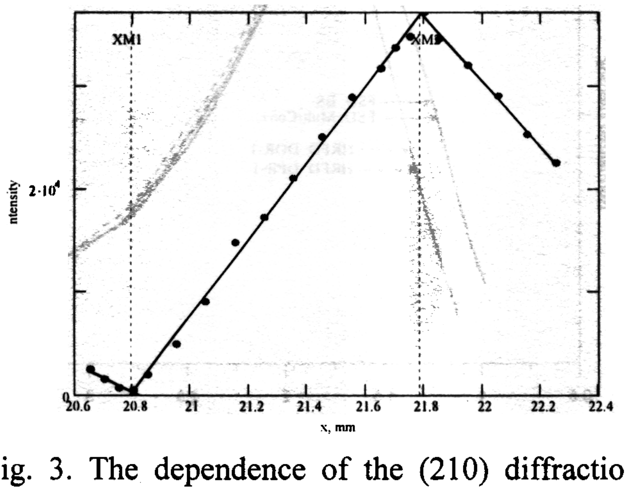

Fig. 3. The dependence of the (210) diffraction peak intensity (d=2.086 Å) versus the rotor position *x*. ^{3}He-detector ($2\theta\approx90°$), sample Al_2O_3, T=3 min.

For good Fourier chopper performance contrast value should be $R \geq 20$. In our case this value is exceeded in 2-3 times depending on a wavelength. Thus the carried out test measurements have confirmed high contrast of the Fourier chopper, which gives a possibility to obtain a good quality of high-resolution spectra.

After first experiments in low resolution mode backscattering BS- detector (2θ = -141°) composed of 16 ^{6}Li scintillation elements (analogue of DPR-1 detector existing on HRFD) was

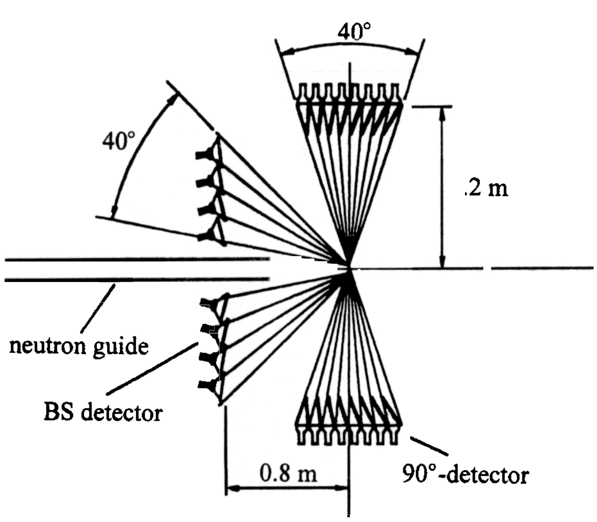

Fig. 4. The detector system of FSD diffractometer.

installed on FSD. Additionally ZnS scintillator based two 1st elements of MultiCon detector ($2\theta = \pm 90°$) were assembled and installed. In final version the FSD detector system will consist of two MultiCon detectors at scattering angles $2\theta = \pm 90°$, at that each of MultiCon detectors will consist of 8 elements (fig. 4). A peculiarity of the MultiCon detector is combined use of electronic and time focusing of a scattered neutron beam that will allow realizing fundamentally new scheme of a detector system with large solid angles (~0.16 steradians for each MultiCon detector). It will essentially increase luminosity of FSD diffractometer (> 10^5 n/cm^2/sec) at saving high-resolution on interplanar spacing ($\Delta d/d \approx 0.004$ at d=2 Å). Besides the wide enough range on d_{hkl} (0.6 ÷ 4 Å) and possibility of operation at fixed scattering angles $2\theta = \pm 90°$ was supplied. The FSD data acquisition system (RTOF-analyzers) was made on a base of modern digital signal processors (DSP). The control system was realized in VME standard with a possibility of remote control of experiment.

A comparison of neutron intensity spectral distributions for FSD and HRFD diffractometers was made with the help of neutron scattering on standard vanadium sample. On FSD mirror neutron guide has greater radius of curvature in comparison with HRFD diffractometer in order to obtain appropriate neutron spectral distribution. It was found that for FSD neutron intensity spectral distribution is shifted towards shorter wavelengths by $\Delta\lambda \approx 0.2$ Å (fig. 5). This fits well to FSD required characteristics since lattice parameters of most studied materials at FSD are rather small so the available d_{hkl}-range should be shifted to smaller values. Integral neutron flux with Fourier chopper measured at the sample position gives quite high value $F \approx 3\times10^5$ neutr./cm^2/sec. The value of Fourier chopper transmission was found ≈ 1/4.5.

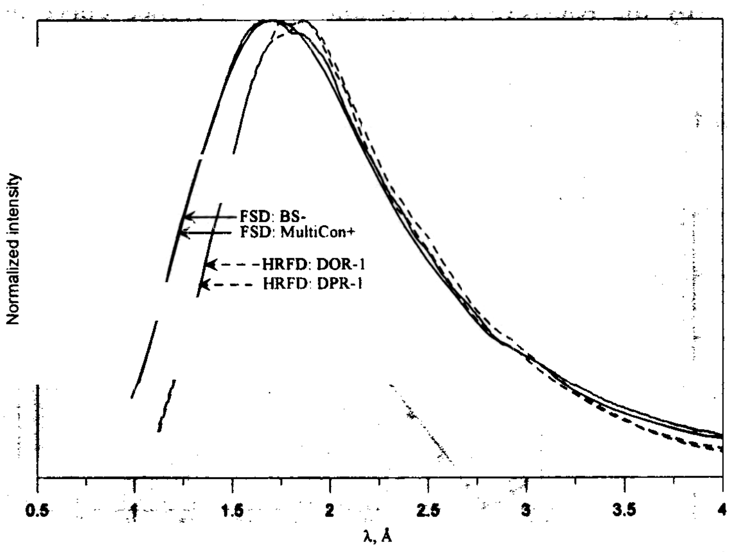

Fig. 5. Comparison of neutron intensity spectral distributions for FSD and HRFD diffractometers. For FSD spectral distribution is shifted by $\Delta\lambda \approx 0.2$ Å towards shorter wavelengths.

The first neutron diffraction patterns from α-Fe standard sample measured on FSD in high-resolution mode by BS- and MultiCon± detectors are shown in fig. 6. After registering first neutron diffraction spectra in high-resolution mode some important experiments were carried out in order to investigate FSD main parameters. Thus FSD resolution function was measured on annealed α-Fe powder by all three detectors at maximal Fourier chopper speed V_{max}=6000 rpm (fig. 7). Results of experiments shown that all detectors have sufficiently high-resolution: $\Delta d/d \approx 2.3\times10^{-3}$ for BS- detector and $\Delta d/d \approx 4\times10^{-3}$ for both 1st elements of MultiCon± detectors at d=2 Å. This outcome confirms fitness of FSD diffractometer for residual stress studies with required accuracy.

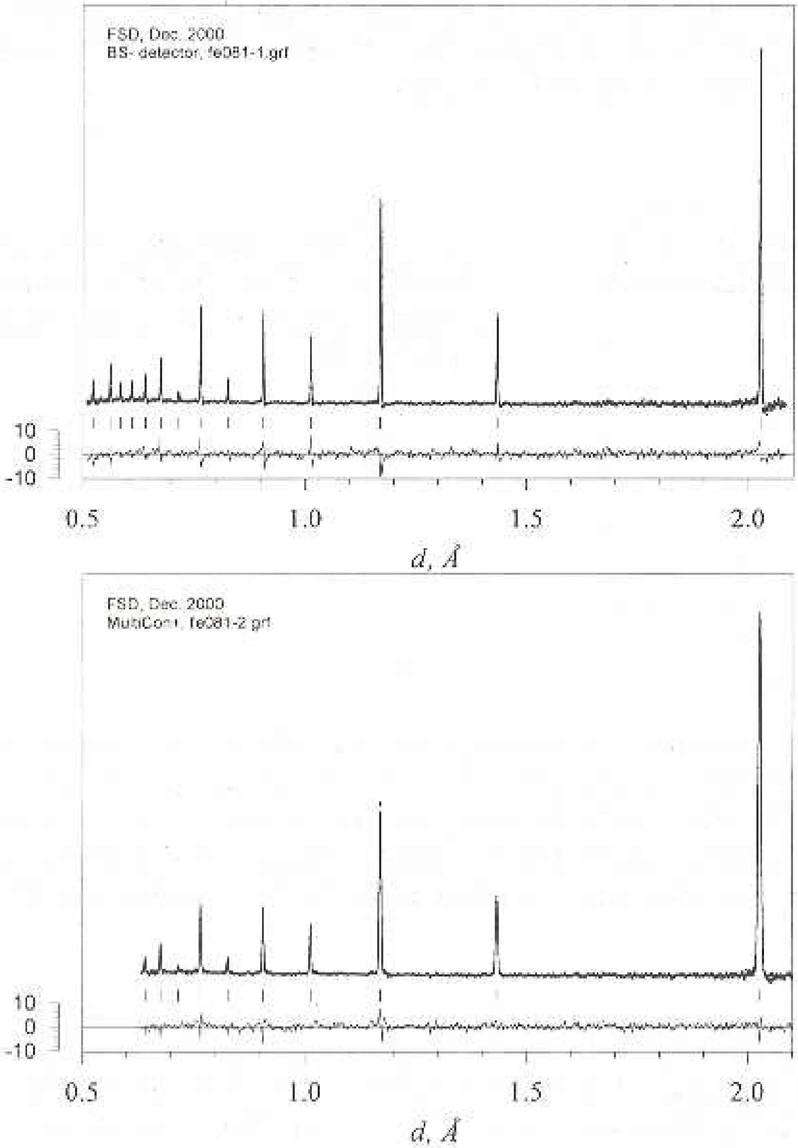

Fig. 6. Part of the neutron diffraction pattern from the α-Fe standard sample measured on FSD in the high-resolution mode by BS- (top) and MultiCon+ (bottom) detectors. The experimental points, the profile calculated by the Rietveld method and the difference curve are shown.

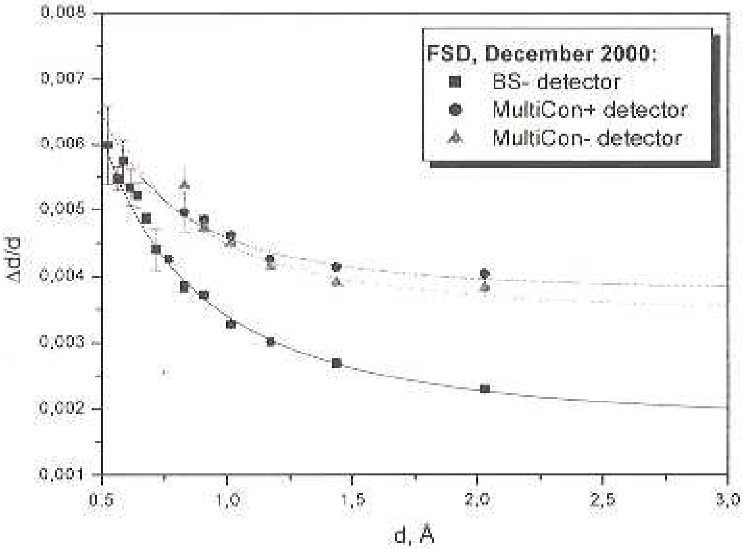

Fig. 7. FSD resolution function measured on the α-Fe powder at maximal Fourier chopper speed V_{max}=6000 rpm.

One of the peculiarities of RTOF technique is diffraction peak width (fig. 8) dependence versus maximal Fourier chopper speed. This feature gives possibility to vary a necessary resolution and luminosity of diffractometer depending on problem to be solved.

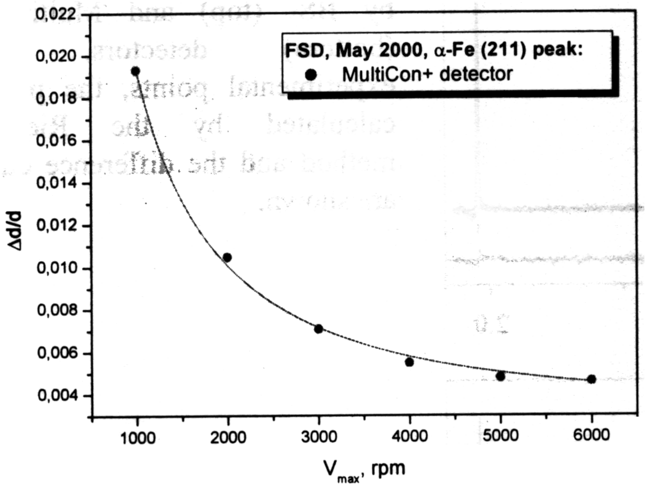

Fig. 8. FSD resolution function dependence versus maximal Fourier chopper speed (α-Fe, peak (211), d=1.1711 Å).

Thus the first stage of FSD construction was completed successfully, that enables to continue work on the further diffractometer development. Currently the designing work on the sample environment (goniometers, collimators, loading devices, furnaces, etc.) and precise sample positioning system is in progress. The existing devices will be adapted to fit the FSD diffractometer. Further work on manufacturing the rest working counters of large area MultiCon detector now is conducted.

REFERENCES

[1] V.L. Aksenov, A.M. Balagurov, V.G. Simkin et al., *J. Neutron Research*, v. 5, p. 181, (1997).

[2] V.L.Aksenov, A.M.Balagurov, G.D.Bokuchava et al., Proc. of National Conference on Application of X-rays, Synchrotron Radiation, Neutrons and Electrons for Material Studies, May 25-29, 1997, Dubna, Russia, vol. 1, pp.69-74 (in Russian).

EFFECT OF ANISOTROPIC THERMAL EXPANSION ON THE PHYSICAL WEATHERING OF MARBLES

K. Ullemeyer[a,b], S. Siegesmund[c], T. Weiss[c] and E.K. Tschegg[d]

[a]Frank Laboratory of Neutron Physics at JINR, 141980 Dubna, Russia
[b]Geological Institute, University of Freiburg, D-79104 Freiburg, Germany
[c]Institute of Geology and Dynamics of the Lithosphere, University of Göttingen,
D-37077 Göttingen, Germany
[d]Institut für Angewandte und Technische Physik, TU Wien, A-1040 Wien, Austria

Introduction

Marbles as building stones often show complex weathering phenomena, which can be of enormous economic importance (see Fig. 1). In addition to the influence of climate and chemical substances (acid rain, biofilms), the highly anisotropic thermal expansion coefficient of calcite and dolomite and therefore their textures have significant influence on mechanical weathering [1]. Marbles with distinctively different fabrics were selected to investigate the relationship between the anisotropy of the thermal expansion α and the residual dilatation behaviour after heating and cooling. In order to understand and to quantify these effects, rock fabric studies were carried out. Based on the calcite and dolomite textures, the directional dependence of thermal dilatation was modeled and compared with the experimental data to identify constraints on the observed weathering phenomena.

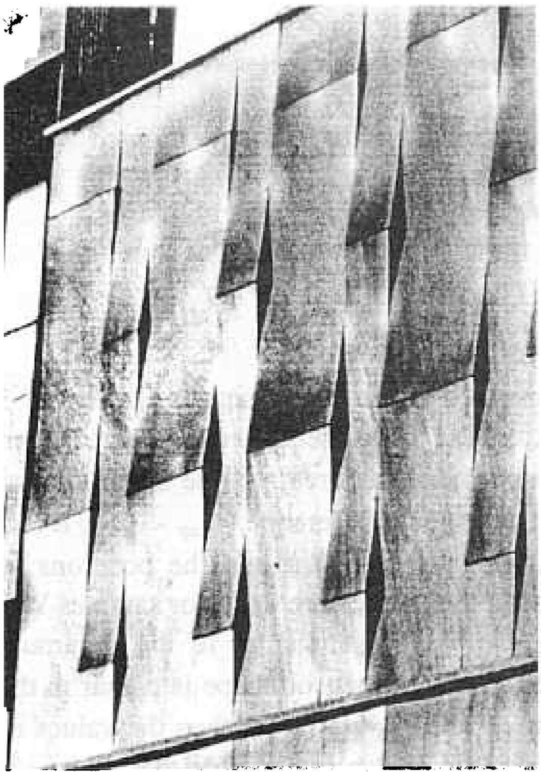

Fig. 1. The deformed facade cladding of the Finlandia Hall at Helsinki, made of Carrara marble.

Experimental Results

The *textures* - which can be sufficiently described by the c-axes pole figures - show variations between axial symmetric and girdle-like intensity distributions (see Fig. 2). The shape parameter T calculated from the pole figure tensor describes the texture differences quite well. It covers the range from $T = -0.824$ (sample WU5) to $T = 0.485$ (sample CA, see Fig. 2) indicating a well pronounced cluster-like and a moderate girdle-like intensity distribution as extreme cases. Because of the strong preferred orientations it must be assumed that the behaviour of the samples is anisotropic with respect to thermal dilatation - even highly anisotropic in some cases.

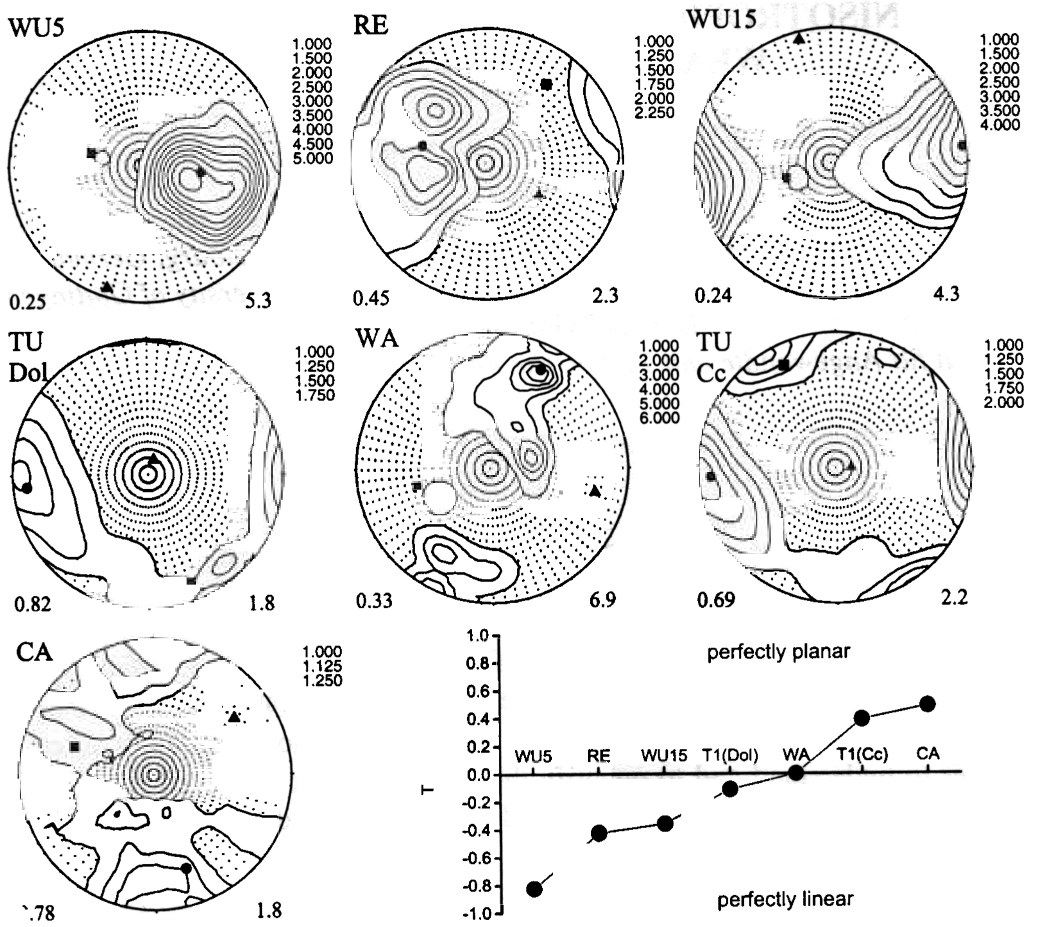

$$T = \left(\ln\frac{e_{int}}{e_{\min}} - \ln\frac{e_{\max}}{e_{int}}\right) \Big/ \left(\ln\frac{e_{int}}{e_{\min}} + \ln\frac{e_{\max}}{e_{int}}\right)$$ (*e*: eigenvalues of the pole figure tensor)

Fig. 2. The c-axes [006] preferred orientations of the samples investigated (calculated from the ODF). Dots, squares and triangles refer to the maximum, intermediate and minimum principal directions of the pole figure tensor, respectively. The graph at the bottom gives the trend of the parameter T which characterizes the shape of the pole figure tensor.

Thermal expansion measurements were performed using a triple dilatometer [2]. Figure 3 illustrates the directional dependence of the thermal expansion coefficient α (i) obtained from thermal expansion experiments, α_{exp} (ii) modeled from the mineral textures and the single crystal constants applying the VOIGT model [3], α_{mod} (iii) as well as of their difference, α_{exp} - α_{mod}. It is a common observation that the patterns of α_{exp} and α_{mod} look quite similar and the positions of maximum and minimum agree more or less. Most pronounced differences are valid for samples WA and WU 15: the maximum of α_{exp} is elongated along a girdle perpendicular to the minimum whereas the plots of α_{mod} show such a trend for the minimum, *i.e.* the tensor shape is planar in the first case and linear in the second one. In all cases, the values of α_{exp} are larger than the values of α_{mod}, *i.e.* the difference is non-zero and is usually quite large. It is also remarkable that the α_{exp} - α_{mod} - distribution is anisotropic as well, and the patterns look different compared to the experimental and modeled ones. The latter observation is well illustrated by the positions of the maxima, see Fig. 3.

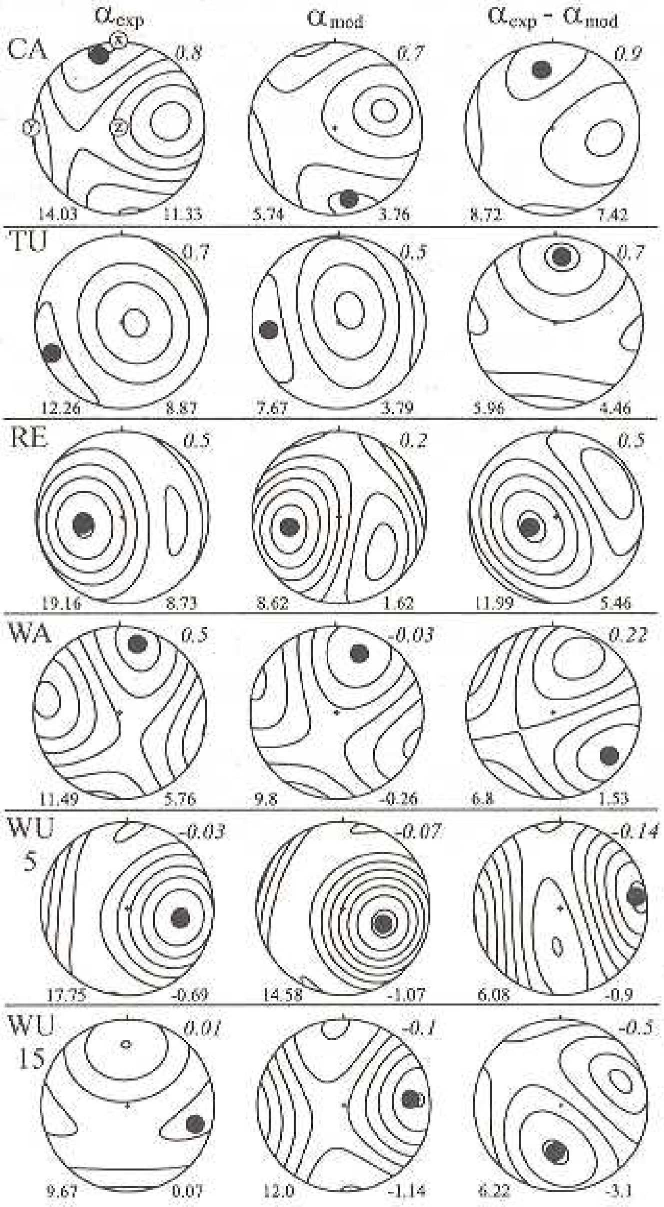

Fig. 3. The directional dependence of the thermal expansion coefficient α: experimentally determind (α_{exp}) and modeled from the textures (α_{mod}). The units are 10^{-6} K^{-1}. The minimum and maximum values are given at the bottom of the plot, as well as the anisotropy parameter $A_T = \alpha_{min}/\alpha_{max}$. The dot indicates the position of the maximum. The right column contains the difference $\alpha_{exp} - \alpha_{mod}$.

Discussion and conclusions

Judging the textures and the pronounced anisotropy of the thermal expansion coefficient α, the following conclusions can be evaluated: (i) for cluster-like c-axis distributions, the maximal thermal expansion can be observed in a single sample direction whereas the intermediate and minimum directions are connected by a girdle. Hence, measuring the thermal expansion in an arbitrary sample direction without knowledge of the texture, the probability to measure smaller values than the mean value is large because the cluster covers only a small area on the pole sphere. (ii) for girdle-like c-axis distributions the minimal thermal expansion is observed in a single sample direction and the intermediate and maximum directions are connected by a girdle. In this case, the probability to measure larger values than the mean value is large because the area of minimal values on the pole sphere is quite small. It is obvious, that large errors may arise in dependence on the type and strength of the texture, if the thermal expansion is estimated only in a single sample direction. Consequently, knowledge of the texture is obligatory for the proper determination of the dilatation behaviour of bulk rock.

The differences between the experimentally determined and modeled thermal expansion coefficients (α_{exp} - α_{mod}) are essentially addressed to the occurrence of microcracks. Microcracks usually originate in the late stage of tectonic history during uplift (stress-induced cracking) or in the late stage of cooling (thermal cracking). They are common in crystalline rocks. New cracks may be generated due to recent thermal treatment, *e.g.* alternating heating/cooling. It is assumed that the formation of new microcracks influences the thermal dilatation anisotropy much stronger than preexisting microcracks, and that microcrack formation is largely controlled by the texture. Evidence to support the conclusion comes from the observation that the topology of the α_{exp} - α_{mod} stereogram (Fig. 3) is clearly associated with the texture. This is true even for the sample with the lowest anisotropy of thermal dilatation, CA. If this relationship between texture and microcrack formation can be confirmed experimentally, it is also confirmed that the influence of the texture on the bulk rock thermal expansion anisotropy is double: (i) direct influence, which at least is based on the single crystal anisotropy (ii) indirect influence due to control of microcrack formation.

References

1. S. Siegesmund, A. Vollbrecht, K. Ullemeyer, T. Weiss, R. Sobott. Application of geological fabric analysis to characterize natural building stones - case study: Kauffung marble, Int. J. for Restoration of Buildings and Monuments, 1997, v.3, pp.269-292.
2. C. Widhalm, E. Tschegg, W. Eppensteiner. Anisotropic thermal expansion causes deformation of marble cladding, J. of Performance of Constructed Facilities ASCE, 1997, v10, pp.5-10.
3. H.J. Bunge, *Texture Analysis in Materials Sciences*, 1982, Butterworth, London.

INFLUENCE OF PARTICLE CONCENTRATION ON FERROFLUIDS MICROSTRUCTURE STUDIED BY SANS

M.V.Avdeev[a], Maria Balasoiu[a*], Doina Bica[b], L.Rosta[c], G.Torok[c], L.Vekas[b]

[a] *FLNPh, JINR, 114980, Dubna, Russia (*permanent address: ISS, Bucharest, R-76900, Romania)*
[b] *Laboratory of magnetic fluids, CFATR, Timisoara Branch of the Romanian Academy, Romania*
[c] *KFKI, H-1525, Budapest, Hungary*

Ferrofluids are dispersions of small, single-domain magnetic particles suspended in a fluid carrier (Fig.1). Aggregation through Van der Waals and magnetic forces is prevented by coating the particles with a surfactant layer. It is known that the stability and properties of magnetic colloidal solutions are considerably due to the degree of surfactant adsorption at the ferrophase surface. The micro-behavior of the surfactant molecules adsorbed at the surface of the particles is not yet completely understood. The data available in the literature [2-3] are insufficient to determine the features of the surfactant behavior under different conditions.

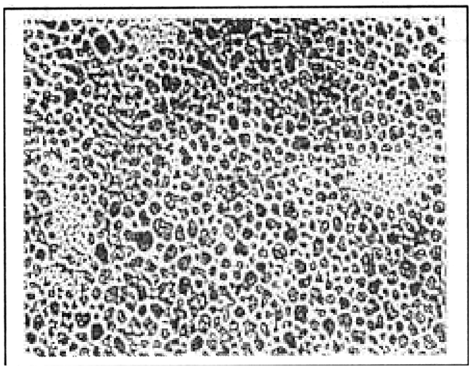

Fig.1 Electron microscopy image of a ferrofluid sample

The purpose of this work is to investigate the changes of the surfactant layer structure due to the variation of the colloid particles concentration by the SANS method . As is well known small angle neutron scattering (SANS) is an ideal method for investigating the structure of particles of about 1-100nm.

We have investigated a deuterated benzene ferrofluid sample of 19% particle volume fraction, with oleic acid as surfactant, prepared by the method of chemical condensation at the Institute of Complex Fluids Timisoara, Romania. The size distribution of magnetite particles analyzed by EM was determined to have a lognormal form with the mean diameter of about 100Å. By dilution with measured quantities of D-benzene were obtained the following volume fractions: 9.5%; 6.3%; 3.8%; 1.1%.

The SANS measurements were performed in the Q-range of $0.01944\ \text{Å}^{-1} \leq Q \leq 0.2778\ \text{Å}^{-1}$ with the SANS facility in function at the VVR-SM, KFKI-Budapest [4]. SANS experiment measures the coherent differential scattering cross section $d\Sigma(Q)/d\Omega$ as a function of the scattering vector $Q = (4\pi/\lambda)\sin\theta/2$, where λ is the neutron wavelength and θ is the scattering angle.

The experimental curves $d\Sigma(Q)/d\Omega$ versus Q, plotted on the logarithmic scale for each value of the particle volume concentration (Fig.2) were fitted with the theoretical expression of scattering from spherical particle with two components:

$$d\Sigma(Q)/d\Omega = \{d\Sigma(0)/d\Omega[\int(V_0+\eta V_1)^2 \quad D_N(R_0)dR_0]^{-1}\} \int[V_0\Phi(QR_0)+\eta V_1\Phi(Q(R+h))]^2 D_N(R_0)dR_0 + B, \qquad (1)$$

where $d\Sigma(0)/d\Omega$ - is the scattering cross section at $Q = 0$; ρ_0, ρ_1, ρ_s - scattering density of the particle, of the surfactant and of the solution; $\eta = (\rho_1-\rho_s)/(\rho_0-\rho_1)$; $V_i = (4/3)\pi R_i^3$; $\Phi = (3\sin x - x\cos x)/x^3$; h - thickness of the surfactant layer, $h = R_1-R_0$; $D_N(R_0)$ - log-normal size distribution; σ - dispersion; B - the contribution of the incoherent and magnetic scattering.

Choosing the best fit of the experimental data for each particle concentration by the variation method of six parameters (R_0, δ, η, h, I(0), B) in the expression (1) we have obtained the following results (Tab.1):

Tab.1[6]

φ	R_0	σ	η	$d\Sigma(0)/d\Omega$	h	B
19%	40.9282	16.1338	-0.79477	59.8176	9.98534	0.06016
9.5%	40.6504	15.5454	-0.80239	46.712	11.4928	0.05011
6.3%	40.5262	15.6075	-0.80889	34.3885	12.368	0.03430
3.8%	41.4544	16.5211	-0.81581	19.1907	14.937	0.021426
1.1%	41.3777	17.6357	-0.80957	3.94212	17.8403	0.009456

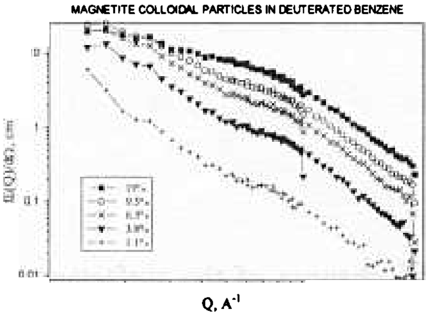

Fig.2 Experimental curves for C_6D_6 ferrofluid samples.

. As we expected the values $d\Sigma(0)/d\Omega$ decrease with the lowering of the particle concentration (Fig.3). It is interesting to notice that h, the thickness of surfactant shell is increasing with the decrease of the particle concentration (Fig.5), the same time η, the degree of the solvent penetration in the surfactant shell is constant. Our results [6] referring to the lowering of the surfactant shell thickness are in agreement with those obtained by viscosity measurements at the Institute of Complex Fluids, Timisoara [7].
The variation of the surfactant shell thickness with particle concentration fits with the following exponential decay (see Fig.4):

$$h(\phi) = h_0 + 8.21\, e^{-(\phi-\phi_0)/t_1}$$

where t_1 is a constant.

As first explanation of the fact that h and R_g, the thickness of surfactant shell and radius of gyration, are changing with particle concentration it was presumed that with the increasing of particle concentration the particles come closer and the "elastic" surfactant layer suffers effects as the partial bending of the oleic acid molecules' tails of the surfactant adsorbed on the same particle, and the interpenetration of surfactant chains.

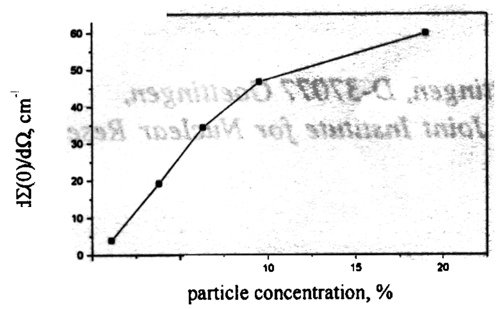

Fig.3 Variation of $d\Sigma(0)/d\Omega$ with the particle concentration.

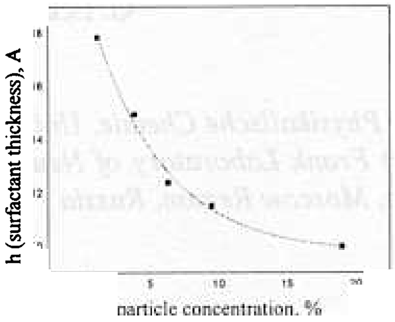

Fig.4 Variation of h, thickness of surfactant shell with particle concentration, ϕ.

To come to final conclusion it will be necessary further to analyze the experimental data taking into account the magnetic scattering, too.

References

[1] S.W.Charles and J.Popplewell, IEEE Trans on Magn., Vol. Mag-16, (1980) 172.
[2] P.C.Scholten, J.Magn.Magn.Mater.39(1983) 99.
[3] R.V.Mehta, P.S.Goyal, B.A.Dasannacharya, R.V.Upadhyay, V.K.Aswal, G.M.Sutariya., J.Magn.Magn.Mater.149 (1995) 47.
[4] M.Balasoiu, S.Borbely, D.Bica, G.Torok, L.Vekas, Experimental Report BNC, 1997.
[5] M.V.Avdeev, M.Balasoiu, D.Bica, S.Borbely, L.Rosta, G.Torok, L.Vekas, 8-th International Conference on Magnetic Liquids, 31 Juin-3 July, Timisoara, Book of Abstracts, 215-216(1998)
[6] M.Balasoiu, Thesis, *On the ferrofluids microstructure*, Bucharest, 1998.
[7] L.Vekas, D.Bica, D.Gheorghe, I.Potencz, M.Rasa, JMMM 201(1999) 159-162.

SMALL-ANGLE NEUTRON SCATTERING FROM TETRADECYLTRIMETHYLAMMONIUM BROMIDE IN NaBr AQUEOUS SOLUTIONS

G. Eckold * and N. Gorski */*

**) Institut fuer Physikalische Chemie, Universitaet Goettingen, D-37077 Goettingen, Germany, **) Frank Laboratory of Neutron Physics, Joint Institute for Nuclear Research JINR, 141980 Dubna, Moscow Region, Russia*

Small angle neutron scattering (SANS) was used to characterize quantitatively the micelles of tetradecyltrimethylammonium bromide (TTABr) at a concentration of about 50 mM in aqueous (D_2O) solutions with added salt NaBr. It is shown that the shape of the micelles change from spheres to rod-like particles with increasing electrolyte concentration. The interparticle interaction becomes effectively screened if the salt concentration exceeds 0.1 M leading to a remarkable growth of the cylindrical micelles. Moreover, it is demonstrated that there is a gradual dehydration of the micelles due to the addition of NaBr.

SANS experiments were performed on the time-of-flight instrument MURN at the pulsed reactor IBR-2, JINR, Dubna, Russia. Using neutrons with wavelengths λ between 0.7 and 10 Å the accessible range of momentum transfer $Q=(4\pi/\lambda)\sin(\theta/2)$ extends from 0.009 to 0.25 $Å^{-1}$. The samples were contained in quartz glass cells (Hellma) with a path length of 1 mm. The temperature of the cells was kept constant at 20.0 ± 0.1 °C by means of a thermostat. Conversion of the scattering intensities into absolute differential cross-sections was done by using vanadium as an internal calibration standard. Background scattering was subtracted by comparison with a reference sample of pure D_2O. The data treatment was done according to the standard procedures.

In Fig.1 the observed intensity distributions are shown for a number of TTABr-solutions with different NaBr-contents from 0.020 to 0.447 M along with the corresponding data for the pure TTABr-solution.

The intensity profile for the pure TTABr solution exhibits a well defined peak at $Q\approx0.046$ $Å^{-1}$. This peak is due the inter-particle structure factor S(Q) and indicates the presence of strong electrostatic interaction between TTABr micelles.

The average distance d between the micelles may be estimated from the position Q_{max} of this correlation peak according to $d=2\pi/Q_{max}=136.5$ Å. The number density n of the micelles is then calculated as $n=1/d^3=3.93\cdot10^{17}$ cm^{-3}. From the total TTABr-concentration C = 52.6 mM and the volume of a single surfactant molecule $V=550$ $Å^3$ we obtain the aggregation number $N=CN_A/n=80.7$ and the micelle volume $V_m=44400$ $Å^3$. Using the fact, that in a pure solution, free of NaBr, the TTABr-micelles are of spherical shape, their radius turns out to be $R \approx 22$ Å in good agreement with the SANS-results of variuos authors [1-4].

As can readily be seen from Fig.1, the addition of NaBr dramatically alters the intensity profile. The correlation peak at $Q_{max}=0.046$ $Å^{-1}$ is gradually reduced as the amount of salt is increased. At a NaBr-concentration of 0.098 M this peak has in fact completely disappeared. This finding is due to the fact that by addition of electrolyte (NaBr) the intermicellar electrostatic interactions are screened substantially and the structure factor is reduced to unity.

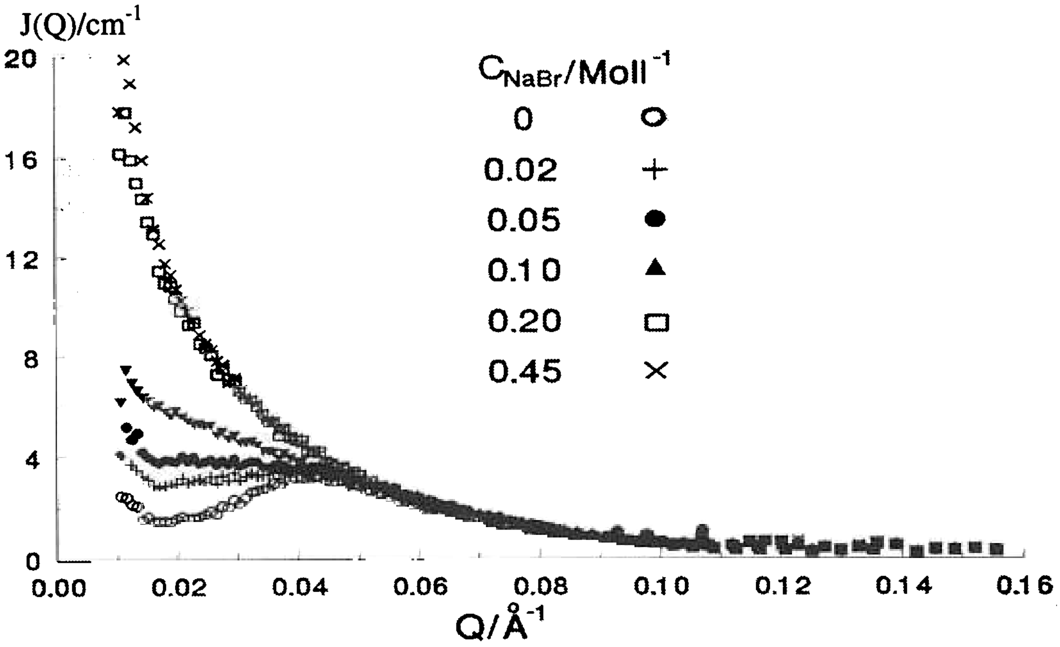

Fig. 1 Neutron scattering intensity profiles J(Q) vs. Q from D_2O solutions containing ≈50 mM TTABr with different NaBr concentrations

The radii of gyration R_g and R_c, the geometrical dimensions of the cylinder, R and L, and the aggregation number per unit micellar length, N/L, are determined according to eqations

$$\frac{d\ln(J(Q))}{dQ^2} = -\frac{R_g^2}{3} \quad (1), \qquad \frac{d\ln(J(Q)\cdot Q)}{dQ^2} = -\frac{R_c^2}{2} \quad (2), \qquad R_c = \frac{R}{\sqrt{2}} \quad (3),$$

$$R_g = \sqrt{\frac{R^2}{2} + \frac{L^2}{12}} \quad (4), \qquad \lim_{Q\to 0}(J(Q)\cdot Q) = \pi\cdot(\rho-\rho_s)^2\cdot C\cdot N_A\cdot\frac{N}{L}\cdot V^2 \quad (5)$$

for the different electrolyte concentrations. These data are collected in table 1.

Table 1: Characteristics of TTABr Micelles in Aqueous (D_2O) NaBr Solutions at 20 °C

C_{TTABr} - the surfactant concentration (mM), NaBr – the salt concentration (M), R_g – the radius of gyration of the whole micelle, R_C – the radius of gyration of the cross sectional area of micelle, R – the radius of the cylindrical micelle, L – the length of the micelle, N/L – the aggregation number per unit micellar length.

C_{TTABr} (mM)	NaBr (M)	R_g (Å)	R_c (Å)	R (Å)	L (Å)	N/L (Å^{-1})
52.4	0.020	25.5±0.4	15.4±0.5	21.8±0.7	70.7±3.0	1.77±0.08
52.0	0.0496	25.7±0.3	16.0±0.2	22.6±0.3	69.8±1.9	1.89±0.04
51.4	0.098	28.5±0.4	16.2±0.2	22.9±0.3	81.1±2.2	1.83±0.03
50,1	0.191	78.9±5.7	17.0±0.1	24.0±0.2	267±20	1.98±0.02
46.8	0.447	112.5±10.6	17.6±0.1	24.9±0.2	384±37	2.15±0.02

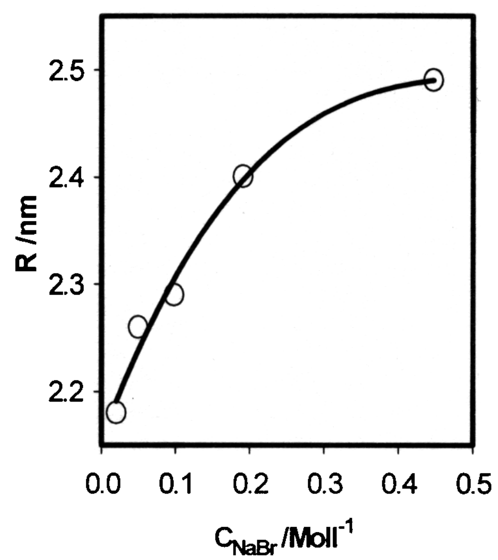

Interestingly, these radii increase with NaBr content from 21.8 ± 0.7 Å at 0.020 M to 24.9 ± 0.2 Å at 0.447 M as shown in Fig.2.

The apparent increase of the radii as determined from the SANS experiments is thus easily be explained by the (partial) dehydration of the hydrophilic head groups. The radius R_o of the bare micelles, however, does not change and is about
25 Å.

Fig.2: Variation of the apparent radius R of the cylindrical micelles vs. C_{NaBr}

The SANS investigations on the system TTABr+D_2O+NaBr at 20 °C and a surfactant concentration of about 50 mM reveal that the micelles exhibit a rod-like shape. As long as the salt concentrations do not exceed 0.1 M the lengths of the micelles are close to 70 – 80 Å and correlation effects due to the interparticle interaction are observed. At higher NaBr content long cylindrical objects are formed, characterized by radii of about 25 Å and lengths of several hundred Å. The apparent increase of surfactant volume with NaBr-concentration from about 415 Å^3 to 550 Å^3 indicates a (partial) dehydration of the -$N(CH_3)_3Br$ head-groups due to the presence of the electrolyte.

For the first time, the gradual stripping of the micelles from its surrounding solvent molecules by the addition of electrolytes could directly be observed. As already suspected by different authors, SANS experiments on D_2O-solutions with no or only minor salt content are likely to yield the properties of the hydrocarbon core of the micelle merely, rather than that of the whole object.

References

[1] Debye P. Ann. N. Y. Acad. Sci. **51** (1949) 575
[2] Zana R., Picot C., Duplessix R. J. Colloid Interface Sci. **93** (1983) 43
[3] Tabony J. Mol. Phys. **51** (1984) 975
[4] Gorski N., Gradzielski M., Hoffmann H. Langmuir **10** (1994) 2594

This work was supported by the Federal Ministry of Education and Science (BMBF) of the Federal Republic of Germany under grant No. 03-DU0GO4-6.

STRUCTURAL CHARACTERIZATION OF UNILAMELLAR LIPID VESICLES WITH ANCHORED ALKYLGLYCOSIDES AT HIGH WATER EXCESS FOR STUDYING CELL RECOGNITION PROCESSES

P. Jörchel[1], J. Gorshkova[2], G. Klose[1], H. Schmiedel[1]

1 Institute of Experimental Physics I, University of Leipzig, Linné-Str. 5, 04103 Leipzig, Germany
2 FLNP, Joint Institute of Nuclear Research, Dubna 141980, Russia

Glycosides play an important role for structural modification of membranes in the process of cell recognition. In extension to our experiments from April this year [1] (system POPC[1]/$C_{12}(EO)_3Glu$[2]) and former experiments [2 - 3] (POPC/$C_{12}E_4$[3]) now we carried out neutron scattering experiments with POPC vesicle membranes containing $C_{12}(EO)_3Glu$, $C_{14}(EO)_3Glu$[4], and $C_{16}(EO)_3Glu$[5], respectively.

The glycoside $C_{12}(EO)_3Glu$ can be considered as a derivative of $C_{12}E_4$ with higher steric requirements (see Fig.1). Furthermore, $C_{14}(EO)_3Glu$ and $C_{16}(EO)_3Glu$ are derived from $C_{12}(EO)_3Glu$ by lengthening the alkyl chain (see Fig.1).

Our attention is directed to the following three points:

- the influence of the exchange of one oxyethylen group by the glucopyranosyl fragment
- the influence of the alkyl chain length
- the influence of the molar ratio POPC/oxyethylen monoalkylether

on the structure of the vesicle membranes (thicknesses of the waterfree core and the water containing headgroup region, the number of water molecules fixed per amphiphile molecule, respectively).

We measured the scattering curves of the samples listed in table I. For measurement vesicles were prepared by extrusion with polycarbonate filters (pore diameter = 200 nm) 25 times, respectively. All measurements were carried out at room temperature (25 °C). The sample thickness was 2 mm in all cases. The measurements covered a q-range from 0.0864 nm^{-1} to 5.92 nm^{-1}.

---

[1] 1-Palmitoyl-2-oleoyl-sn-glycero-3-phosphocholine

[2] Glucopyranosyl-trioxyethylen-mono-dodecylether

[3] Tetra-oxyethylen-mono-dodecylether

[4] Glucopyranosyl-trioxyethylen-mono-tetradecylether

[5] Glucopyranosyl-trioxyethylen-mono-hexadecylether

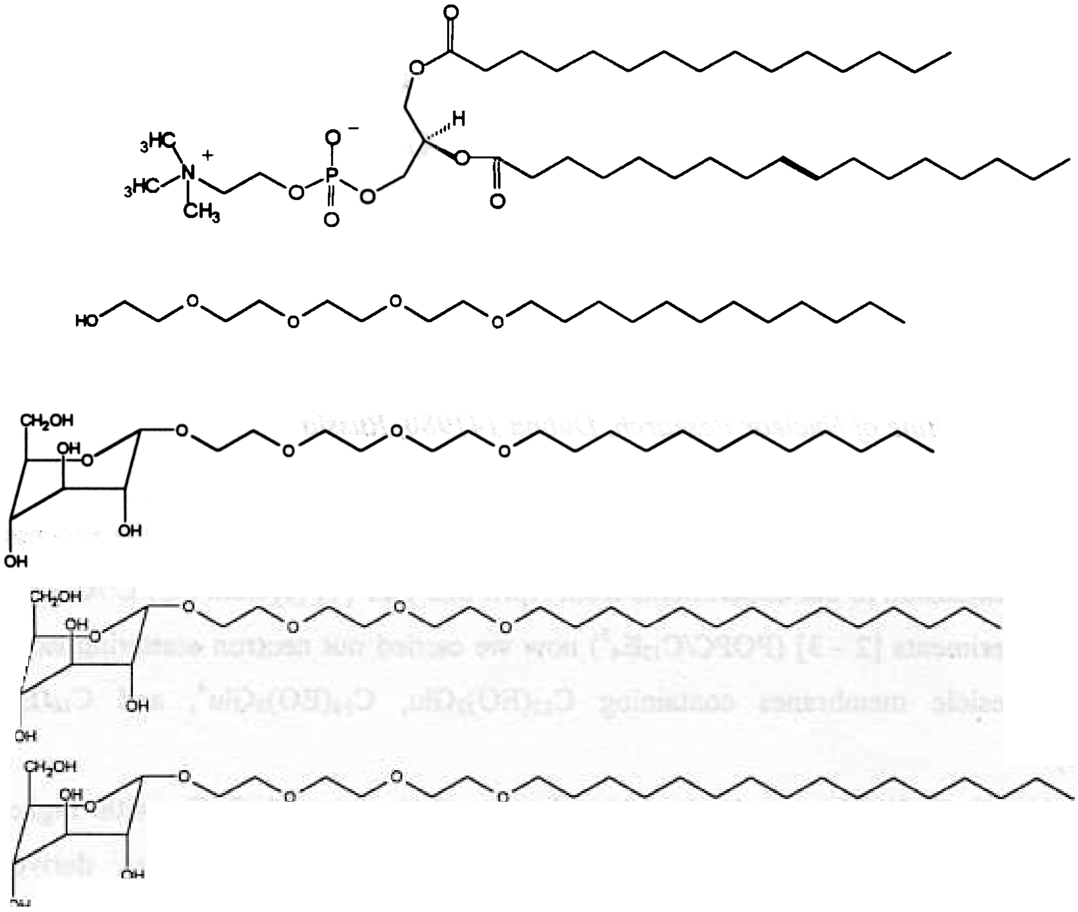

Figure 1: structural comparison of the components of the considered systems, POPC, $C_{12}E_4$, $C_{12}(EO)_3Glu$, $C_{14}(EO)_3Glu$, $C_{16}(EO)_3Glu$ (in the listed order)

Table I: measured samples (S ... $C_{12}E_4$ or $C_n(EO)_3Glu$, respectively)

Sample No.	**content**	**x_S = $n_S/(n_S+n_{POPC})$**	**c(amphiphil) in mg/ml**	**t in minutes**
1	**POPC + $C_{12}(EO)_3Glu$ in D_2O**	0.25	10	360
2	**POPC + $C_{12}(EO)_3Glu$ in D_2O**	0.50	10	360
3	**POPC + $C_{14}(EO)_3Glu$ in D_2O**	0.25	10	360
4	**POPC + $C_{14}(EO)_3Glu$ in D_2O**	0.50	10	360
5	**POPC + $C_{16}(EO)_3Glu$ in D_2O**	0.25	10	360
6	**POPC + $C_{16}(EO)_3Glu$ in D_2O**	0.50	10	360

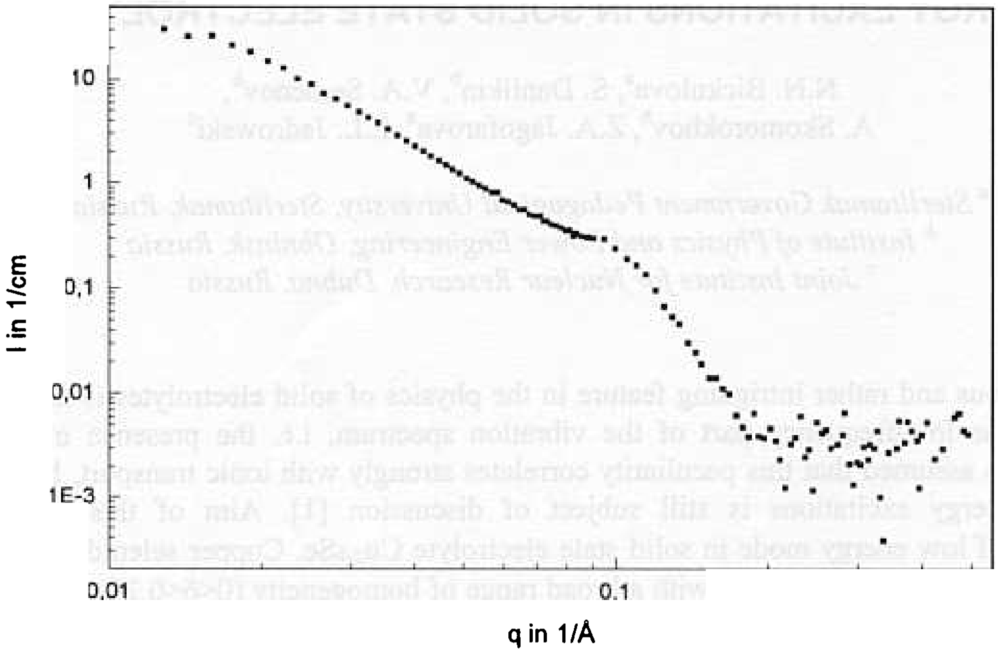

Figure 2: scattering curve of POPC/$C_{14}(EO)_3$Glu (x_S = 0.5)

The data of all samples shows a diffraction shoulder at 1 nm^{-1} which is caused by the presence of a small amount oligolamellar liposomes with a repeat distance of about 6.3 nm. There are small differnces in the shape of the scattering curves. A further and more elaborated data analysis will provide structural details about the inner structure of the membranes (see above: thicknesses of different region water content).

References:

[1] P. Jörchel, J. Gorshkova, M. Kiselev, G. Klose, H. Schmiedel: Structural characterization of unilamellar lipid vesicles with anchored alkylglycosides at high water excess for studying cell recognitation processes, experimental report at YuMo at FLNP Dubna, April 2000.
[2] P. Jörchel, M. Kiselev, G. Klose, H. Schmiedel: Determination of Structural Parameters and Hydration of Unilamellar Vesicles at high Water Excess from SANS Curves Using a Multiple-strip Model, experimental report at YuMo at FLNP Dubna, Dec. 1999.
[3] Schmiedel, H.; Jörchel, P.; Kiselev, M.; Klose, G.: J. Phys. Chem., in press.

LOW ENERGY EXCITATIONS IN SOLID STATE ELECTROLYTE CU$_{2\text{-}X}$SE

N.N. Bickulova[a], S. Danilkin[b], V.A. Semenov[b],
A. Skomorokhov[b], Z.A. Jagofarova[a], E.L. Jadrowski[c]

[a] *Sterlitamak Government Pedagogical University, Sterlitamak, Russia*
[b] *Institute of Physics and Power Engineering, Obninsk, Russia*
[c] *Joint Institute for Nuclear Research, Dubna, Russia*

An ubiquitous and rather intriguing feature in the physics of solid electrolytes is the anomalous behavior of the low-frequency part of the vibration spectrum, i.e. the presence of low-energy excitation. It is assumed that this peculiarity correlates strongly with ionic transport, but the origin of the low-energy excitations is still subject of discussion [1]. Aim of this experiment is investigation of low energy mode in solid state electrolyte $Cu_{2\text{-}\delta}Se$. Copper selenide $Cu_{2\text{-}\delta}Se$ has a mixed ionic-electronic conductivity with a broad range of homogeneity ($0<\delta<0.25$). The peculiarity of this system is that a deviation from stoichiometry (δ) and temperature (T) correlate with the ionic transport. For example, Cu_2Se has superionic phase transition at 140°C with disordering of copper cations and $Cu_{1.75}Se$ belongs to the superionic phase at room temperature already.

Copper selenide in contrary to other solid state ionics shows the low energy mode at room temperature in the superionic ($Cu_{1.75}Se$) and non superionic Cu_2Se) phases [2-4]. Figure 1 demonstrates dynamic structure factor $S(Q,\omega)$ for Cu_2Se and $Cu_{1.75}Se$ at room temperature and two values of momentum transfer $Q = 3.1$ and 3.2 Å^{-1}.

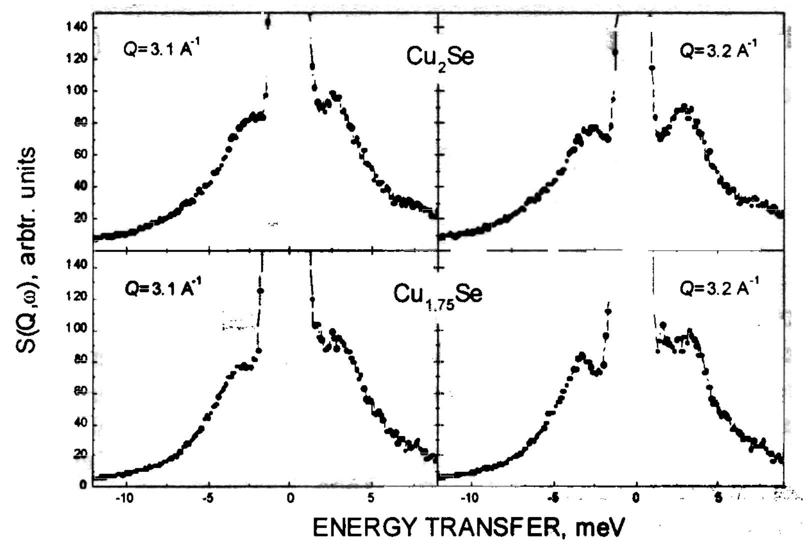

Figure 1. Dynamic structure of Cu_2Se and $Cu_{1.75}Se$ at room temperature and Q=3. and 3.2 Å^{-1}

Intensity, peak-position and width of the low-energy mode show pronounced Q-dependence when $S(Q,\omega)$ spectra of Cu_2Se and $Cu_{1.75}Se$ are the similar. Low frequency excitations are in evidence in both the superionic and non-superionic phases. The presence of the low frequency excitations in both phases of copper selenide is unexpected. Usually the low energy excitations is associated with localized vibrations of mobile ions in its non-superionic phase. Such excitations, however, have been believed to disappear upon transition the most of the solid electrolytes into their superionic phase.

One possible explanation of the unique behavior low energy mode in copper selenide is that only 1/8 part of Cu-cations is mobile in superionic phase [5]. There is assumption that fraction of mobile cations decreases with deviation of stoichiometry and there are no mobile cations in $Cu_{1.75}Se$. Other assumption on origin of the low energy mode in $Cu_{2-\delta}Se$ is its associations with tunneling diffusion of the mobile cations. To study lattice dynamic of superionic conductors and check these assumptions we started the set experiments experiment on neutron scattering in copper selenide at various compositions and temperatures.

Preliminary results show that superionic phase transition in copper selenide via composition and temperature is non-equivalent (see fig 2).

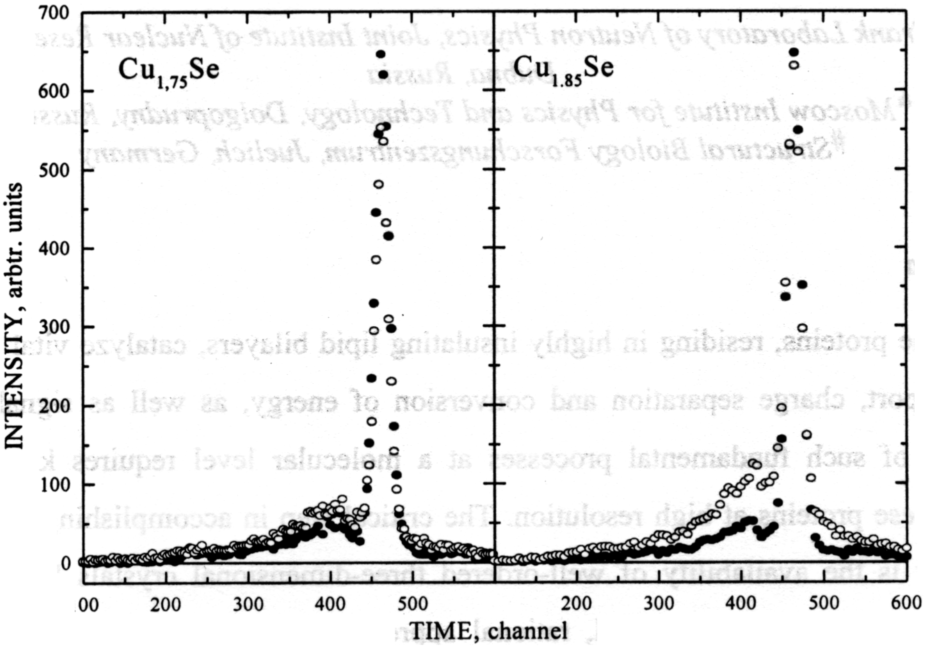

Figure 2. Inelastic neutron scattering spectra on $Cu_{1,75}Se$ и $Cu_{1,85}Se$ at T=20 °C (filled circles) and T=150 °C (empty circles) in time of flight scale. Initial neutron energy is 12 meV, scattering angle –71.2°. Peak at 460 channel corresponds to elastic neutron scattering, spectrum on the left from elastic peak to scattering with neutron energy gain, and from the right to the neutron energy loss scattering.

Figure 2 shows that INS spectra in $Cu_{1.75}Se$ do not change dramatically as temperature increases. Intensity of the spectrum corresponding to the neutron energy gain increases with the temperature due to Bose factor, quasi elastic peak decreases due to Debaye-Waller factor, intensity of the spectra with neutron energy loss is not changed practically. At the same time INS spectra of $Cu_{1,85}Se$ is changed essentially as temperature increases to 150 °C. Wide tails of quasielastic peak corresponding to the fast diffusion of the mobile copper cations appear in the INS spectra at 150 °C.

These results confirm assumption on decreasing of the mobile copper cations with deviation from stoichiometry. We need to note that this results is preliminary, data analysis in progress now. Further detailed experiments is invited also.

Reference

[1] M. B. Salamon (Ed.): Physics of Superionic Conductors, Springer-Verlag, Berlin (1979).

[2] N. Bickulova, S. Danilkin, V. Sememnov, E. Jadrovski,: Low frequency modes in $Cu_{2-\delta}Se$ superionic conductor; submitted to XVI Workshop on neutron scattering study of condensed matter, 13-17 September, 1999, Obninsk, Russia.

[3] T. Sakuma, K. Shibata: Journal of Physical Society of Japan, **58** (1989) 3061.

[4] T. Sakuma, K. Shibata, S. Hoshino: Solid State Ionics **40/41** (1990) 337.

[5] R. A. Yakshibaev, V. N. Konev, Soviet Solid State Physics **26** (1984) 3641-3645.

INVESTIGATIONS OF MECHANISM OF MEMBRANE PROTEINS CRYSTALLIZATION IN LIPIDIC CUBIC PHASE

G.Bobarykina*, R.Efremov*&, V.Gordeliy*#, A.Islamov*, A.Kuklin*
and G. Bueldt#

* *Frank Laboratory of Neutron Physics, Joint Institute of Nuclear Research, Dubna, Russia*
&*Moscow Institute for Physics and Technology, Dolgoprudny, Russia*
#*Structural Biology Forschungszentrum, Juelich, Germany*

1. Intoduction

Membrane proteins, residing in highly insulating lipid bilayers, catalyze vital reactions such as solute transport, charge separation and conversion of energy, as well as signal transduction. Understanding of such fundamental processes at a molecular level requires knowledge of the structures of these proteins at high resolution. The critical step in accomplishing of this by X-ray crystallography is the availability of well-ordered three-dimensional crystals [1]. E.Landau and J.Rosenbush [2] have devised a novel, rational approach to meet this goal using lipidic cubic phases. This membrane system, consisting of lipid, water and protein in appropriate proportions, forms a structured, transparent and complex three-dimensional lipidic array, which is pervaded by an intercommunicating aqueous channel bicontinuous system. Such matrices provide nucleation sites and support growth by lateral diffusion of protein molecules in the membrane.

Only this method of crystallization in cubic phase was successful in crystallization of an important membrane protein - bacteriorhodopsin (BR) [2]. This membrane protein is light-driven proton pump, which creates gradient of hydrogen ions. The energy of this gradient is used by cell for ATP synthesis to provide the *Halobium Salinarium* cells with energy.

Bacteriorhodopsin crystals were obtained from bicontinuous cubic phases, which consisted of monoolein (1-monooleoyl-*rac*-glycerol) or monopalmitolein (1-monopalmitoleyl-*rac*-glycerol) and water [3]. In both cases the intensively purple colored crystals are formed. Crystals of hexagonal morphology are appeared inside the MO matrix, while the MP system yields rhombic crystals.

However, it is not clear whether crystallisation of membrane proteins in lipidic cubic phase is a general method. Moreover, it is an open problem why lipidic cubic phase promote crystallization of membrane proteins.

Main aim of this work is to study phase behaviour of cubic phase formed by monoolein in course of BR crystallization. We expect that such investigation is necessary to understand how general is the behaviour of cubic phase in those cases when BR crystalls are growing.

2. Materials and methods

Standard conditions of BR crystallization [2] were used for the investigation of mechanism of the crystallization via small-angle neutron diffraction at the YuMO spectrometer, Dubna, Russia. 1-monooleoyl-*rac*-glycerol (C18:1) was purchased from Sigma Chemical and used without further purification.

Investigations of lipid phase behaviour at different protein concentrations (from 0.4 to 14 mg/ml), protein/buffer (250mM Na/K/P_i in D2O, 1.2% w/w octylglucoside, pD=6.0) rations and salt concentrations have been carried out. The samples were prepared by using the standard method for protein crystallization: 5 μl of BR buffer was added to 5mg of dry monoolein, centrifuged and then the phosphate salt was added and again centrifuged.

3. Results

In this work the behaviour of BR/MO/buffer system in course of crystallization was studied by small angle neutron scattering (YuMO, Dubna, Russia).

We observed that investigated system forms cubic phase of Pn3m symmetry with lattice constant 16±2Å larger than that of MO/buffer system. The protein essentially influences this system.

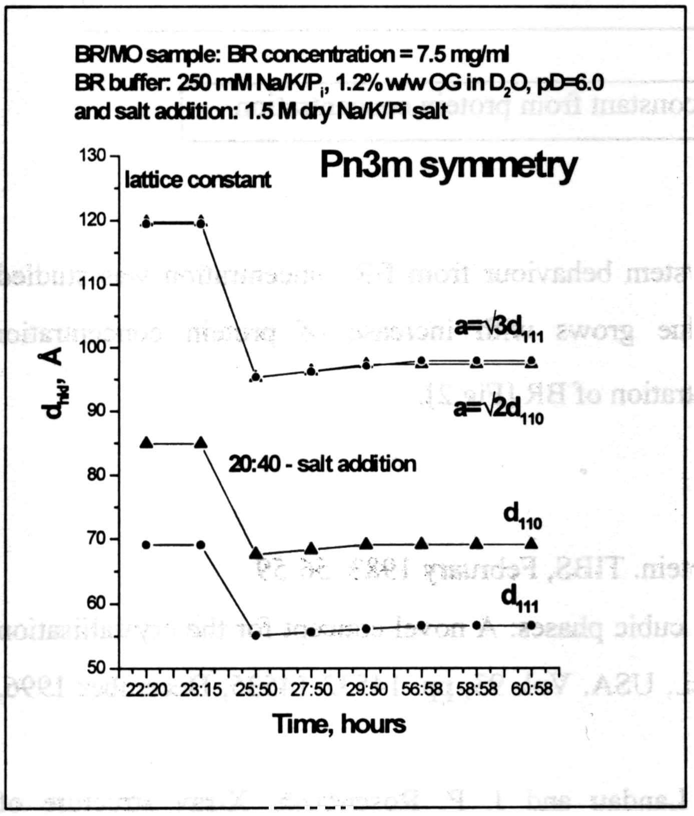

Fig.1. The dependence of repeat distance d_{hkl} and lattice constant for BR/MO buffer system.

BR crystallization was initialising by salt addition. The addition of the salt influences on lattice constant, which is decreased by ~15Å [Fig.1], but not the symmetry of cubic phase. Main changes occur during first 3 hours. It was shown that macroscopic phase symmetry is invariable in course of crystallization, the system does not undergo phase transitions [Fig.1].

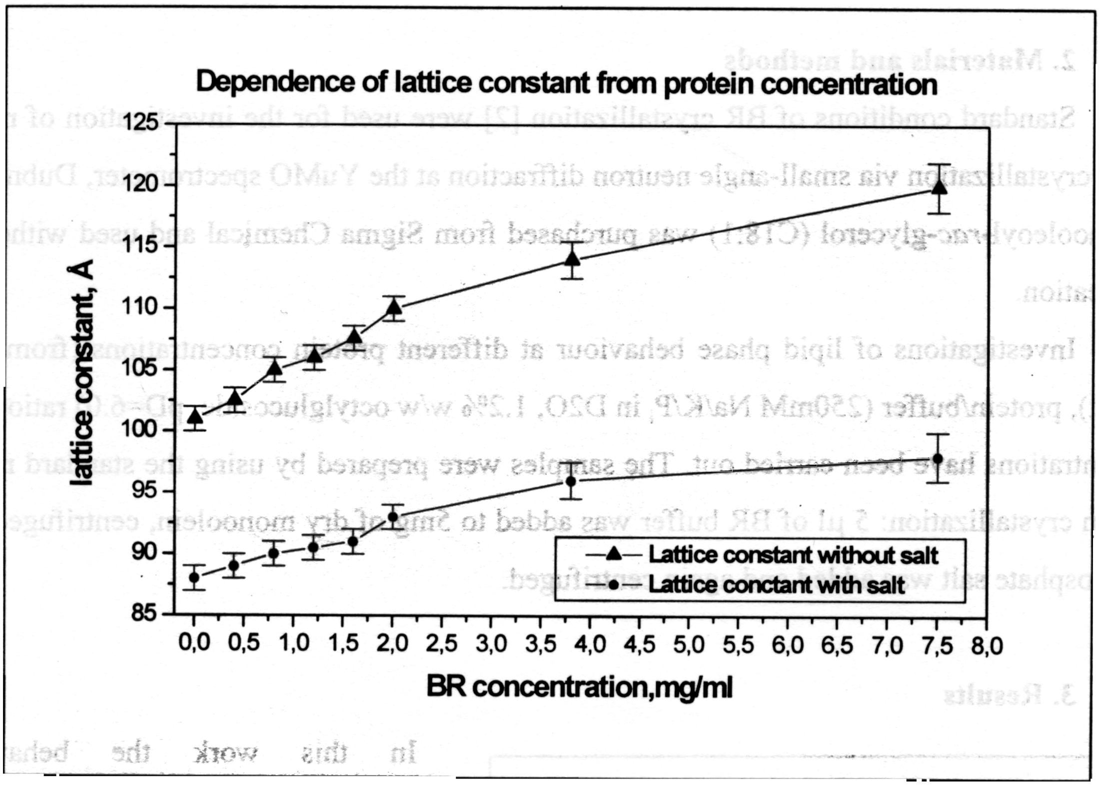

Fig.2. Dependence of lattice constant from protein concentration

Also dependence of BR/MO/buffer system behaviour from BR concentration was studied. We observed that the lattice constant value grows with increase of protein concentration approximately linearly up to 7.5mg/ml concentration of BR [Fig.2].

References:

1. H. Michel. Crystallization of membrane protein. TIBS, February 1983: 56-59
2. E. M. Landau and J. P. Rosenbush. Lipidic cubic phases: A novel concept for the crystallisation of membrane proteins. Proc. Natl. acad. Sci., USA. Vol. 93, pp. 14532-14535, December 1996, Biophysics.
3. E. Pebay-Peyroula, G. Rummel, E. M. Landau and J. P. Rosenbush. X-ray structure of bacteriorhodopsin at 2.5 Angstroem from Microcrystals Growth in Lipidic Cubic Phases. Science, vol. 277, 12 Sept., 1997.

THE STUDY OF THE UNBINDING OF MEMBRANES BY SANS

V. Gordeliy[1], U. Gorshkova[1], A.Islamov[1], V. Haramus[2]

[1] *Frank Laboratory of Neutron Physics, Joint Institute of Nuclear Research,*
Dubna, Russia
[2] *GKSS Research Centre, Geesthacht, Germany*

1 Introduction

Intermembrane equilibrium distance is determined by the van der Waals short-range repulsion, long range electrostatic and undulation (repulsion) forces [1]. Superposition of these forces result in a global energy minimum, which can be shifted to infinite distance under change of the balance of the forces. It means that the transition has a sharp, first order character [2].

However, it has been argued that in presence of undulations the superposition does not work. The reason is that in presence of the undulations different parts of the surfaces of the opposite membranes are not placed at the same distance. Statistical mechanical treatments of the intermembrane interactions in this case were not successful [3]. Nevertheless, in spite of an analytical expressing of the intermembrane forces have not been derived it was shown that unbinding transition between a bound and a free (unbound) state should have a continuos character. It has been proved by renormalization group treatment [3], Monte-Carlo simulation [4] and mean field approach [5]. However, the character of the unbinding has never been experimentally rigorously examined.

2 Materials and methods

Synthetic dimyristoyl- phosphatidylcholine (DMPC) were used. The given amount of $CaCl_2$ in a $CaCl_2$ / D_2O solution was mixed with the lipid (about 1 wt %). The range of the salt concentrations from 0.0 mM to 1.0 mM was used. The measurement was carry out in gel and liquid phases at $T=15^0C$ and $T=55^0C$ respectively.

The samples were kept in quartz cells with a path length of 1.5 mm. For the control of the temperature the thermostate sample holder was used. Scattering data measured using the YuMO spectrometer are present as a function of the magnitude of the scattering vector q.

3 Results

The studies have shown that multilamellar membranes of DMPC in gel phase unbind when the concentration of $CaCl_2$ or $MgCl_2$ increases (Figure 1). It has been argued that this phenomenon can have a continuos character [3]. This prediction was never checked. Indeed, there is no experimental data on the unbinding of the mentioned above systems in liquid phase. As far as undulations are considerable only in liquid phase one can expect a continuos unbinding in this state of the membranes.

The aim of this project was to study in detail membrane unbinding in gel and liquid phases. It seems that SANS is the best method to do this. Indeed, our preliminaries SANS test have shown interesting features of this phenomenon. It is demonstrate in figure 1.

We have observed that the transition is quite sharp and occurs between 0.2 and 0.3 mM $CaCl_2$ in gel phase (see figure 2). The repeat distance is almost constant until the transition occurs. However, the intensity of the diffraction peaks and small angle part of the scattering curves change dramatically with the increase of the concentration of the ions (see Figure 1). It may mean a special type of a continuous unbinding. In any case it is a new observation.

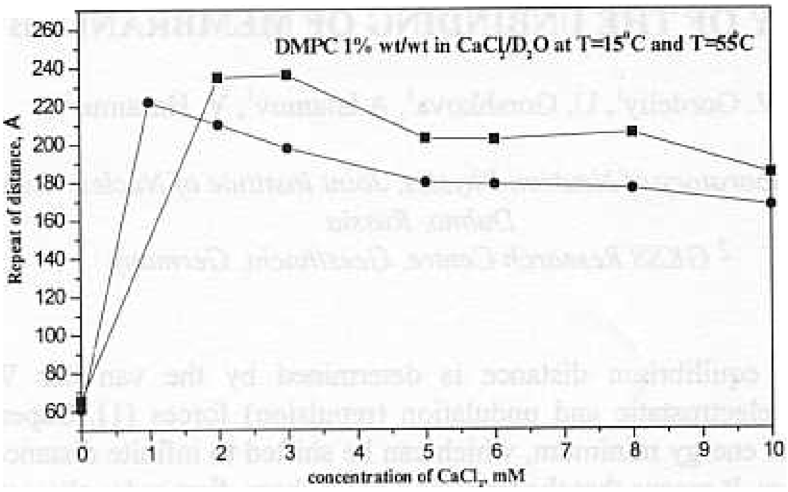

Figure 1: The repeat distance of the DMPC multilayers as a function of the CaCl2 concentration.

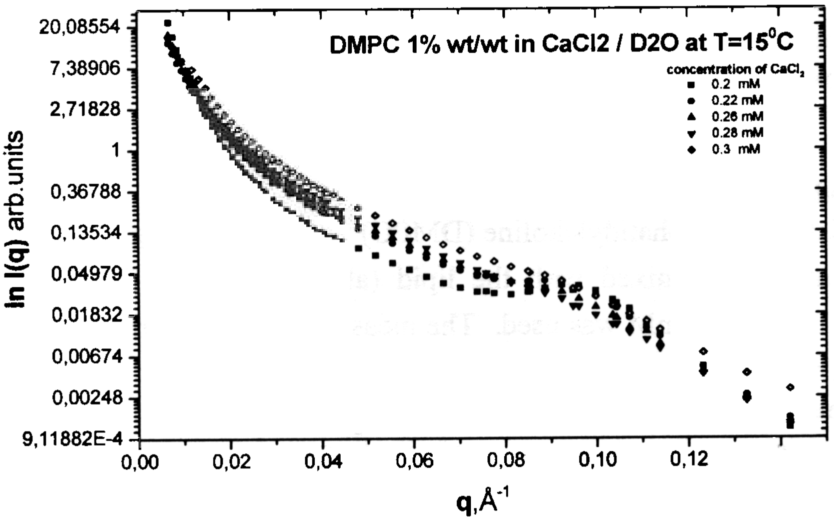

Figure 2: Scattering curves of DMPC/CaCl$_2$/D$_2$O mixture for the following concentration of the CaCl$_2$: 0.2mM, 0.22mM, 0.26mM, 0.28mM, 0.3mM

1. Izraelachvili, J.N., and H. Wennerstrum. 1992. Entropic forces between amphiphilic surfaces in liquids. *J. Phys. Chem. 96: 520-531.*
2. Lipowsky R. 1995. Generic interection of flexible membranes. *In Handbook of Biological Physics. V 1B:521-602*.
3. Lipowsky R., and S. Libler. 1986. Unbinding transition of interacting membranes. *Phys. Rev. Lett. 56, 2541-2544.*
4. Lipowsky R., and B. Zelinska. 1989. Binding and unbinding of lipid membranes. A Monte Carlo Study. *Phys. Rev. Lett. 62, 1572-1575.*
5. Helfrich W. 1993. Mean field theory of n-layer unbinding. *J. Phys. II France 3:385-393.*

WATER MODERATOR OF A REACTOR IBR-2 WITH A CANYON ON A LATERAL SURFACE. A DESIGN AND PHYSICAL PARAMETERS.

A.A.Beliakov, V.I.Bodnarchuk, D.A.Korneev, V.F.Peresedov, E.P.Shabalin,
S.P.Yaradaikin

Frank Laboratory of Neutron Physics
Joint Institute for Nuclear Research

The component of the new methane cryomoderator of a reactor IBR-2 - water premoderator - serves simultaneously as a thermal moderator for 9-th and 1-th channels. The radiation of neutrons in the direction of 9-th channel occurs from a lateral surface of a moderator. The specific feature of a reflectometer a REFLEX located on 9-th channel, consists that it "sees" neutrons, irradiated only from the limited region of a surface of a moderator. The form of this region represents the rectangular, extended along a vertical, with the horizontal size about 7 millimeters. With the purpose of increase of a flux on a sample, on a lateral surface of a moderator in a direction parallel to a wall of an active core of a reactor on distance 52 mm from it the vertical slot-hole pocket (canyon) by depth of 80 mm, width 15 mm and height 200 mm was created. The design data of a moderator and results of relative measurements of distribution of a flux of neutrons along a lateral surface as a function of distance from an active core of a reactor are resulted.

The water premoderator - integral part of a design of the new methane cryomoderator of a reactor IBR-2, represents a cavity filled with water at a room temperature. The casing of a premoderator structurally joint with a vacuum casing of a methane moderator represents a box fabricated from an aluminium alloy (see. fig. 1). The basic applicability of a water premoderator: a) to transform a spectrum of fast neutrons of fission in thermal and to "protect" a methane from fast neutrons of an active zone of a reactor; b) to serve as a thermal moderator for 1 and 9 channels of a reactor IBR-2. The cavity, nearest to a reactor core, of a premoderator is filled with thickness of 10 mm by a powder B_4C. Such decision is traditional for water moderators of a reactor IBR-2 and is dictated by necessity to shield an active zone from thermal neutrons which are taking off from moderators. Thus, structurally water premoderator and methane cryomoderator make a single unit. The premoderator adjoins directly to an active core of a reactor. The further transformation of a spectrum of neutrons in "cold" is carried out by a solid-state methane moderator, contiguous to a water premoderator cooled up to temperatures 30-60K. The geometry of an arrangement of the cryomoderator on a reactor is those, that four beams (IV, V, VIa, VIb) (see. fig. 2) "look" at an obverse surface of a methane moderator. Except for

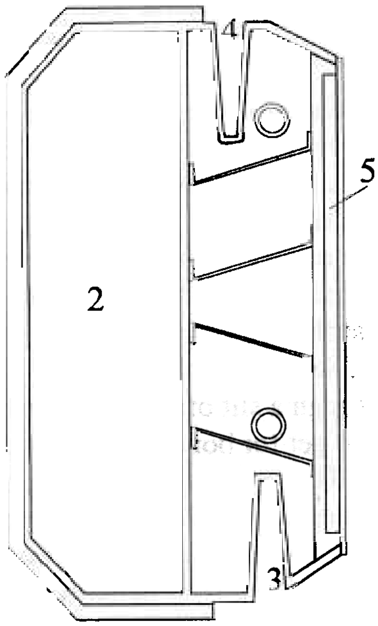

Fig. 1 Section of the cryomoderator in a horizontal plane. 1-cavity of a water premoderator; 2-cavity filled with a methane; 3, 4-slot-hole pockets (canyon) from the sides of channels 9 and 1 accordingly; 5-cavity filled B_4C

the listed beams there are two coaxial beams (I and IX), which "look" at lateral walls of a water warm premoderator from the opposite sides (axis of these beams are perpendicular to lateral surfaces of a premoderator).

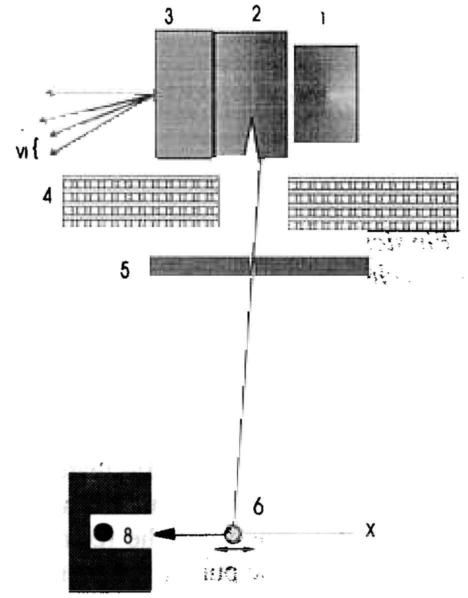

Fig. 2 Figures explaining the experiment by determination of distribution of density of a flux on a lateral surface of a premoderator on 9 channel IBR-2: 1-core of a reactor; 2-premoderators with a canyon; 3-methane moderators; 4-biological shields of a reactor with an aperture of shutter; 5- collimators with narrow (3 mm) vertical slit; 6- vanadium thin cylinder (scatterer) located on the mobile mechanism; 7-shields of the detector, 8-helium detectors; the Roman figures designate directions of the appropriate beams

On the 9-th channel of IBR-2 the neutron reflectometer REFLEX is located. The specific feature of a reflectometer consists that it "sees" neutrons, irradiated only from the limited region of a surface of a moderator. The form of this region represents the rectangular, extended along a vertical, with the horizontal size about 7 millimeters. Other part of a surface of a moderator in experiment is not used.

Taking into account this specific property of a reflectometer, with the purpose of increase of a flux on a sample, the design of a premoderator was complicated. Namely, on its lateral surface the vertical slot-hole pocket (canyon) by depth of 80 mm, width 15 mm and height 200 mm and located on distance 52 mm from a wall closed to the active reactor core was created (see a fig. 1). The similar pocket was created as well with opposite the side of a premoderator. It was supposed, that it will result to local in the field of a canyon to increase of a flux of irradiated neutrons.

In figure 2 the experiment on study of distribution of a flux of neutrons on a lateral surface of a premoderator from the side of 9 channel is shown. The collimator with a narrow vertical slit (width - 3.0, height - 150 of mm) was placed on distance of 7.5 meters from a moderator in the experimental hall of the reactor directly with a wall of a ring corridor. On distance of 20.1 meters from a collimator the vanadium cylinder by a diameter of 5 mm and

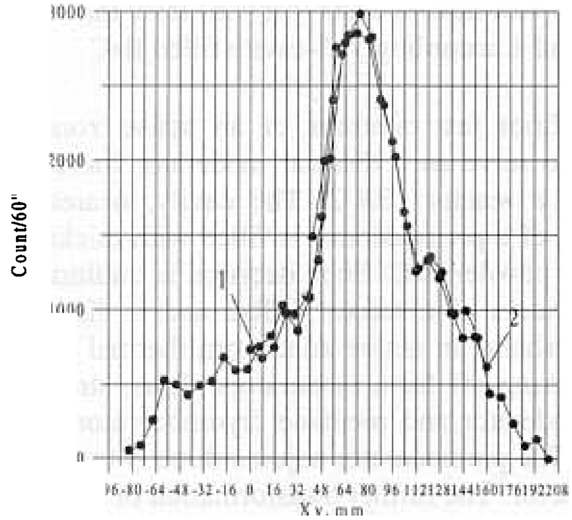

Fig. 3 Dependences of the count of the detector of the vanadium coordinate after subtraction of a background. The position of a maximum of count of the detector coincides with conyon position. The zero values of the count on the left and right borders of distribution correspond to coordinates of vanadium of which projection through a slit of a collimator on a premoderator get for borders of aperture of the shutter. The numeral on the diagram mark coordinates of vanadium in relation to which the spectral gain of a flux in a point of a maximum (see fig. 4) is determined

height 100 mm was placed in order to scatter neutrons in the detector direction. The cylinder automatically with accuracy of 0.05 mm could move in a horizontal plane across a neutron beam. The neutrons scattered by vanadium were registered by the detector fixed in shield on distance 400mm from an average position of vanadium. The window in shield of the detector was oriented so, that the vanadium cylinder always was in a field of visibility of the detector. Obviously (see. fig. 2) that a projection of the vanadium cylinder through a slit of a collimator (vertical stripe like spot with width 5mm) on a surface of a premoderator moves synchronously with moving vanadium. Thus, the registration of scattered neutrons by the detector at various coordinates of vanadium carries out measurement of horizontal plane distribution of a flux on a surface of a premoderator. In figure 3 the measured distribution of neutron intensity is shown depending on coordinate of vanadium (integrated over a thermal neutron spectrum). From figure it is visible, that the distribution on a surface of a moderator of an integrated intensity has at the certain coordinates brightly expressed maximum. The gain in an intensity in these coordinates in relation to an average intensity behind its equal approximately to 3.5. In a fig. 4 the neutron wave length dependence of a gain in an intensity in maximum in relation to intensities behind its in coordinates 1 and 2 figures 2 is shown. It is visible, that at increase the relative gain grows and at 3 angstroms reachessize 4.5 and 5.5 for points 1 and 2 accordingly.

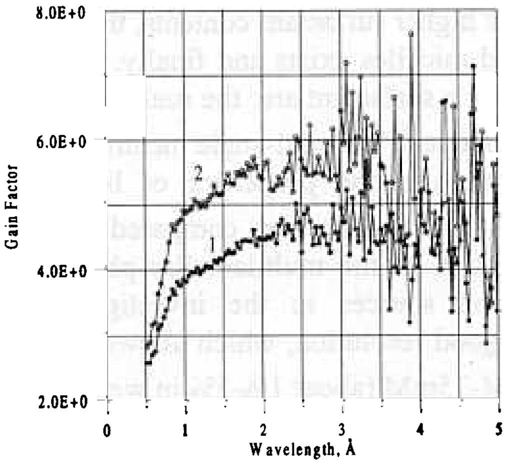

Fig. 4 Spectral gains in a local flux in a point appropriate to a position of a canyon on a premoderator concerning points outside a canyon. The curves 1, 2 correspond to points 1 2 in a fig. 2

The received results have confirmed essential increase of a local flux of neutrons which are irradiated from a canyon area of a surface of a moderator. It will allow to use this area on a moderator for formation of a beam of neutrons on REFLEX and as result (see fig. 3,4) to lift luminosity of installation essentially.

The authors thank V.L.Aksenov for support, V.V.Golikov and A.D.Rogov for the useful remarks.

DMPC MEMBRANE SWELLING BY NONIONIC SURFACTANT $C_{12}E_8$: X - RAY DIFFRACTION STUDY

M.A. Kiselev*, D. Lombardo#, P. Lesieur#

** - Frank Laboratory of Neutron Physics, JINR, 141980 Dubna, Russia*
 # - LURE, Bat. 209-D, B.P. 34, F-91898 Orsay, France

Mixed lipid/surfactant aggregates are currently of great interest because of their wide use for the development of new drug delivery systems. The phase state of a dilute aqueous lipid/surfactant mixture depends on the effective surfactant mole fraction in the aggregates. Mixed bilayers are formed up to the saturating fraction of the surfactant. For higher surfactant contents, the coexistence range of surfactant-saturated bilayers and lipid-saturated micelles exists and finally, only micelles are found. The main stages of membrane solubilisation by a surfactant are: the multilamellar phase, unilamellar phase, rod-like micelles, and spherical micelles/1/. Small-angle neutron and X-ray scattering are appropriate techniques to study the structure and properties of lipid/surfactant aggregates in the unilamellar or micellar phases/2,3,4/. X-ray diffraction compared with neutron diffraction is a more suitable method for the investigation of the multilamellar phase structure. Synchrotron sources have an advantage over neutron sources in the investigation of the multilamellar phase due to an extremely high flux and good resolution, which allows you to study diluted systems with a small lipid concentration of 15mM-75mM (about 1%-5% in weight)/5/.

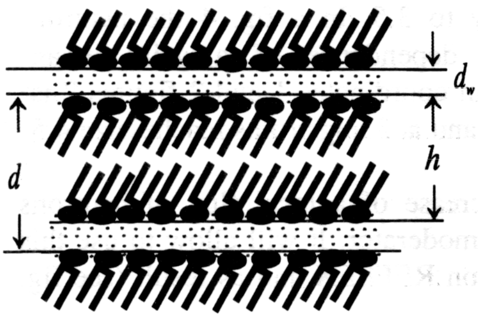

Fig. 1. The schematic representation of the gel $L_{\beta'}$ - phase of the DMPC multilamellar structure. The multilamellar structure consists of DMPC bilayers with the membrane thickness h and solvent layers with the solvent thickness d_W. The repeat distance of the DMPC membrane $d = h + d_W$. In the $L_{\beta'}$ - phase, the DMPC hydrocarbon chains tilte to the membrane surface.

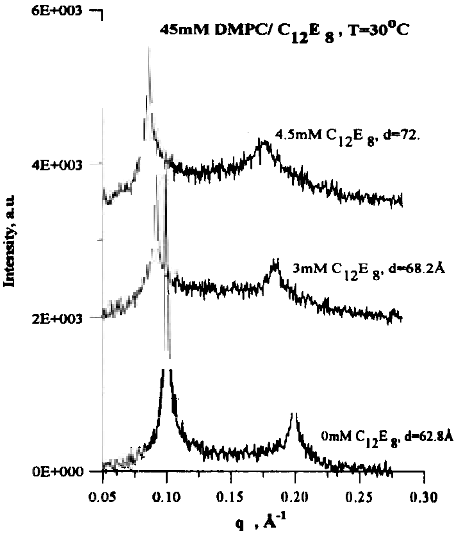

Fig. 2. The diffraction patterns recorded with the acquisition time 10min (0mM $C_{12}E_8$), 10min (3mM $C_{12}E_8$), 15min (4.5mM $C_{12}E_8$).

A highly diluted multilamellar phase of the DMPC/$C_{12}E_8$ system is characterized with the help of X-ray diffraction on beam line D22 of the synchrotron source DCI, LURE, France. The first stage of membrane solubilization, which is the transformation of multilamellar to lamellar phase, was studied for systems with the DMPC concentrations 30mM, 45mM, and 60mM as a function of surfactant concentration and temperature. Figure 2 presents the diffraction patterns recorded at T=30°C for the 45mM DMPC with the surfactant concentration 0mM (pure water), 3mM, and 4.5mM. The DMPC membrane repeat distance increases from 62.8±0.3Å at a 0 surfactant concentration to 68.2±0.3Å at the surfactant concentration 3mM, and to 72.3±0.4Å at 4.5mM. A decrease in the intensity of the diffraction peak with increasing surfactant concentration corresponds to a decrease in the number of multilayers in the liposomes. All the measured membrane repeat distances for the 45mM DMPC as a function of surfactant concentration and temperature are presented in Fig. 3. An increase of d with increasing surfactant concentration describes membrane swelling. Membrane swelling is calculated as a derivative d of the surfactant concentration at constant temperature. The results of the calculation are presented in Fig. 4 for 30mM, 45mM, and 60mM lipid concentrations.

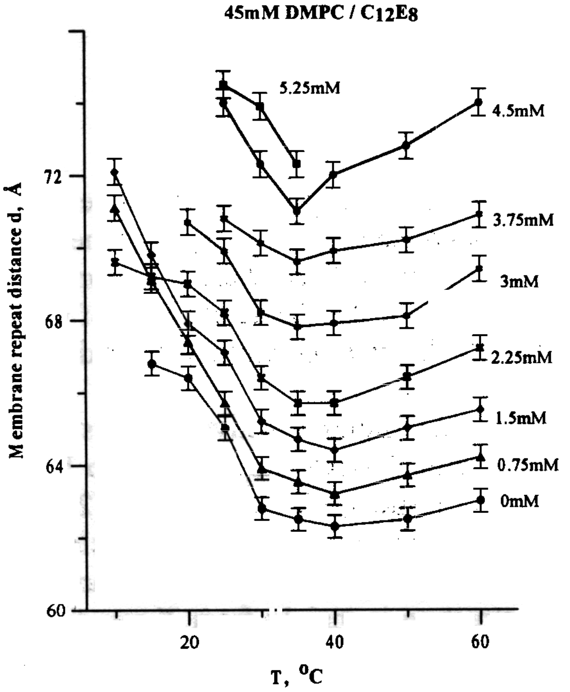

Fig. 3. The 45mM DMPC. The repeat distance as a function of temperature for the surfactant concentrations: 0; 0.75; 1.5; 2.25; 3; 3.75; 4.5; 5.25mM.

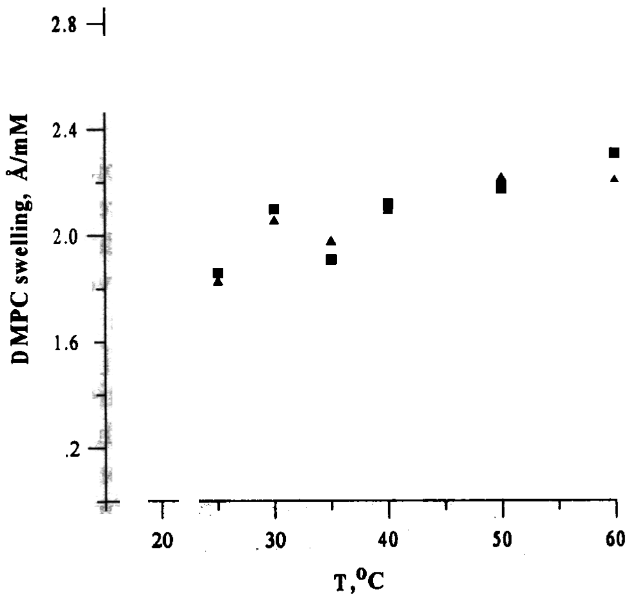

Fig. 4. DMPC membrane swelling as a function of temperature for 30mM DMPC (circles); 45mM DMPC (squares); 60mM DMPC (triangles).

It is found that membrane swelling is a temperature dependent parameter. DMPC membrane swelling has a tendency to increase from 1.25±0.15Å/mM at T=20°C to 2.26±0.20Å/mM at T=60°C. The swelling has a local maximum at T=30°C and a local minimum at T=35°C.

Acknowledgments: This study was supported by the TMR program for Large Instruments.

References

1. M.A. Kiselev, P. Lesieur, A. M. Kisselev, S.A. Kutuzov, L.I. Barsukov, T.N. Simonova, T. Gutberlet, G. Klose. Investigation of temperature sensitive mixed lipid/detergent systems at the YuMO spectrometer. JINR publication E3, 14-98-168 (1998), 52-57.
2. P. Lesieur, M.A. Kiselev, L.I. Barsukov, D. Lombardo. Temperature induced micelle to vesicle transition: kinetic effects in the DMPC / NaC system. J. Appl. Cryst. 33 (2000) 623-627.
3. T. Gutberlet, M. Kiselev, H. Heerklotz, G. Klose. SANS study of mixed POPC/$C_{12}E_n$ aggregates. Physica B, 381-383 (2000) 276-278.
4. H. Schmiedel, P. Joerchel, M.Kiselev, G. Klose. Determination of structural parameters and hydration of unilamellar POPC/$C_{12}E_4$ vesicles at high water excess from neutron scattering curves using a novel method of evaluation. J. Phys. Chem. B 105 (2001) 111-117.
5. M.A. Kiselev, P. Lesieur, D. Lombardo, A.M. Kisselev, T. Gutberlet. The investigation of temperature-sensitive phospholipid /surfactant systems via neutron and X-ray small-angle scattering and diffraction. Chemistry and Physics of Lipids, 107 (2000) 72.

STRUCTURE FACTOR OF DMPC UNILAMELLAR VESICLES: SAXS STUDY AT SYNCHROTRON

M.A Kiselev*, D. Lombardo#, A.M. Kisselev$, P. Lesieur#

** - Frank Laboratory of Neutron Physics, JINR, 141980 Dubna, Moscow reg., Russia*
 # - LURE, Bat. 209-D, B.P. 34, F-91898 Orsay, France
$ - Physics Department, Cornell University, Ithaca, NY 14853, USA

1. Introduction

Vesicles technology is a rapidly evolving field in basic and applied sciences and engineering. In addition, at present there are several industrial organizations engaged in the research and development of processes and products from vesicular materials. Thus, there is a strong driving force for the development of noninvasive and accurate methods for the characterization of vesicular dispersions. For potential applications of vesicular systems the size, polydispersity and dynamic properties are needed to be determined [1].

Of particular interest is application of the phospholipid vesicles as delivery agents of drugs, genetic materials and enzymes through living cell membranes. Vesicle size appears to be a key factor in their permeation through tumor microvessels and the residence in tumor tissues [2].

Today, the problem of accurate simultaneous determination of the vesicle radius, polydispersity and the internal membrane structure is not solved yet in SAXS and SANS experiments. Information about the internal membrane structure is mainly from X-ray diffraction experiments on multilamellar vesicles [3]. Large unilamellar vesicles are a more biologically appealing model of lipid bilayer than multilamellar vesicles. The new proposed methods (Schmidel's model and Pencer's approach) of the evaluation of the membrane thickness involve complementary techniques (freeze fraction cryomicroscopy and dynamic light scattering) to characterize the vesicle size and polydispersity [4,5].

A 40% sucrose buffer has been used in a SAXS investigation of a micelle to vesicle transition in a mixed DMPC/ionic surfactant system [6]. In this approach, the vesicle size and distribution were calculated directly from the SAXS curves. Sucrose solutions in water decrease the vesicle size and polydispersity and create appropriate experimental conditions for the investigation of vesicles via SAXS and SANS [7].

Different authors have reported the appearance of intervesicle interaction for vesicles at different lipid concentrations in the range of 3%-5% w/w. To clarify this problem, the SAXS experiment on vesicles with a low polydispersity was carried out in the range of scattering vectors $0.004Å^{-1} \le q \le 0.04Å^{-1}$ at a synchrotron source DCI (beam line D22). DMPC vesicles were prepared via extrusion through polycarbonate filter with the pores diameter 500Å for 15mM, 30mM, 45mM, 60mM, 75mM DMPC concentrations in the 40% sucrose buffer.

2. Results and discussion

The macroscopic cross section of monodispersed vesicles is

$$\frac{d\Sigma}{d\Omega}_{mon}(q,R) = n\cdot(\Delta\rho)^2\cdot F(qR,d_l)\cdot S(qR)\,, \qquad (1)$$

here n is the number of vesicles per unit volume, $F(qR,d_l)$ is the form factor of a hollow sphere in the approximation $R \ll d_l$ [5,6], R is the vesicle radius, d_l is the membrane thickness, $\Delta\rho$ is the X-ray contrast between the membrane and aqueous sucrose solution, and S(qR) is the structure factor of spherical vesicles in the Debye form

$$S(qR) = 1 - \frac{8V_v}{v}\left(8\pi \cdot \frac{R^2}{qR} \cdot Sin(2qR)\right) \qquad (2)$$

The experimentally measured macroscopic cross section $d\Sigma(q)/d\Omega$ was calculated via convolution of equation (1) with the vesicle distribution function $G(R)$ by integration over the vesicle radius R_{min}=70Å to R_{max}=2000Å

$$\frac{d\Sigma}{d\Omega}(q) = \frac{\int\limits_{R\min}^{R\max} \frac{d\Sigma}{d\Omega}_{mon}(q,R) \cdot G(R) \cdot dR}{\int\limits_{R\min}^{R\max} G(R) \cdot dR} \qquad (3)$$

A nonsymmetrical Schulz distribution was used to describe vesicle polydispersity

$$G(R) = \frac{R^m}{m!} \cdot \left(\frac{m+1}{\bar{R}}\right)^{m+1} \exp\left[\frac{(m+1) \cdot R}{\bar{R}}\right] \qquad (4)$$

Finally, the $d\Sigma(q)/d\Omega$ values were corrected for the resolution function of the D22 spectrometer.

The polydispersity of vesicles P was defined as half width at half height (HWHH) of distribution function (4), $P = 1.18 \cdot \sqrt{\frac{1}{(m+1)}}$.

The SAXS curve for the DMPC concentration 15mM can be fitted well with $S(q)\equiv 1$. Fitting with $S(q)\equiv 1$ of the SAXS curve with the DMPC concentration 30mM gives overestimated results for the q range $0.004Å^{-1} \leq q \leq 0.008Å^{-1}$. The experimentally measured SAXS curves and the fitted curves with a structure factor in the Debye form are shown in Fig. 1. The obtained vesicles parameters are presented in Tab. 1. The experimental curves for the range of DMPC concentrations from 15mM to 75mM are fitted well with the introduced interaction as it is seen in Fig. 1. The application of different DMPC concentrations makes it possible to determine the accuracy of the evaluation of model parameters from the SAXS experiment. The evaluation of the membrane thickness from the q range $q \leq 0.04Å^{-1}$ gives a big uncertainty in the value of the membrane thickness because this region of the scattering vector is just the begining of the Guinier region. No physical reason exists for the differences in the values of R, P, d_l for the different discussed concentrations of DMPC (for 75mM DMPC, $\frac{V_v}{v} = 0.106$). From the results presented in Table 1 the average model parameters are calculated for DMPC vesicles at T=30°C: $\bar{R} = 254 \pm 16$Å; P=0.29±0.07; d_l=36.6±4.1Å.

Figure 2 shows the calculated values of the structure factors $S_{av}(q)$ for all the DMPC concentrations presented in Figure 1. The average $S_{av}(q)$ functions were calculated with the Schulz distribution and vesicles parameters from Table 1. For 15mM DMPC, $|S_{av}(q)-1|<0.05$ for $q \geq 0.004$ Å^{-1}, and $S_{av}(q) \approx 1$ for $q \geq 0.006$ Å^{-1}, $|S_{av}(q)-1|<0.05$ for 30mM DMPC at $q \geq 0.006$ Å^{-1}. For the DMPC concentrations ≥45mM, $|S_{av}(q)-1|>0.05$ at $q=0.008$Å^{-1}. The average structure factor $S_{av}(q)$= 1 for all the concentrations at $q \geq 0.02$ Å^{-1} due to the system polydispersity. The influence of the structure factor is negligibly small for the Guinier region ($q \geq 0.02$ Å^{-1}), which is important for the determination of the membrane thickness.

3. Conclusions

Disregarding of structure factor calculations for the lipid concentrations ≥30mM (2% w/w) leads to errors in the calculation of the vesicle radius. At the same time, the structure factor correction is not important in the evaluation of the membrane thickness from the small angle experiment. For the lipid concentrations about 15mM (1% w/w) the structure factor correction is negligibly small. For the SANS experiment with polarized neutrons an increase of the scattering intensity is a problem due to decreasing of the polarized neutron flux. The use of samples with the lipid concentrations 5%-10% w/w is a much simple way to improve statistics in the SANSP experiment. The correct evaluation of vesicle structure factor is necessary in this case.

TABLE 1. The vesicle parameters evaluated from the model calculations of the SAXS curves. $\bar{R}$ is the average vesicle radius, P is the vesicle polydispersity, d_l is the membrane thickness at T=30°C.

DMPC concentration, mM	15	30	45	60	75
$\bar{R}$, Å	242±1	252±1	255±1	261±1	261±1
P	0.30	0.26	0.30	0.34	0.33
d_l, Å	40±5	35±5	35±5	36±5	37±5

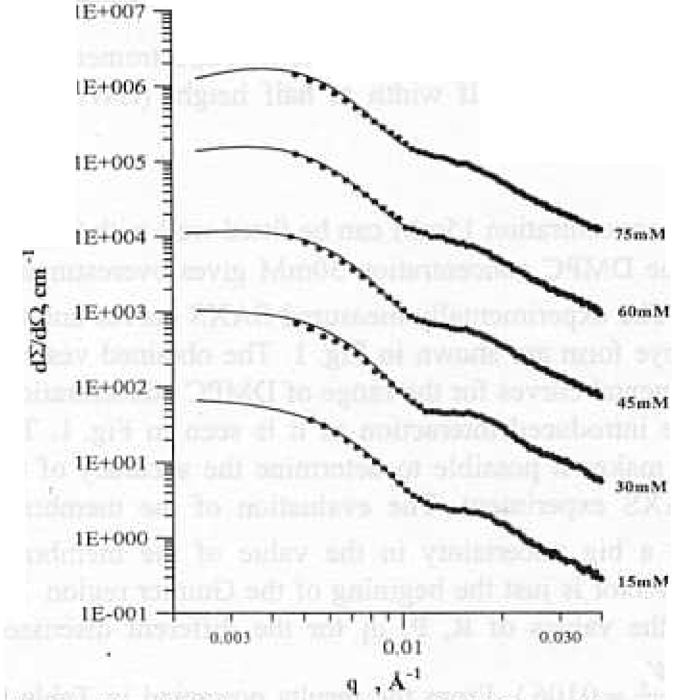

Fig. 1. The SAXS spectra from DMPC vesicles at T=30°C. The macroscopic cross section for the 15mM DMPC vesicles in absolute units. The macroscopic cross sections for 30mM, 45mM, 60mM, and 75mM are multiplied by 10, 100, 1000, 10000, respectively.

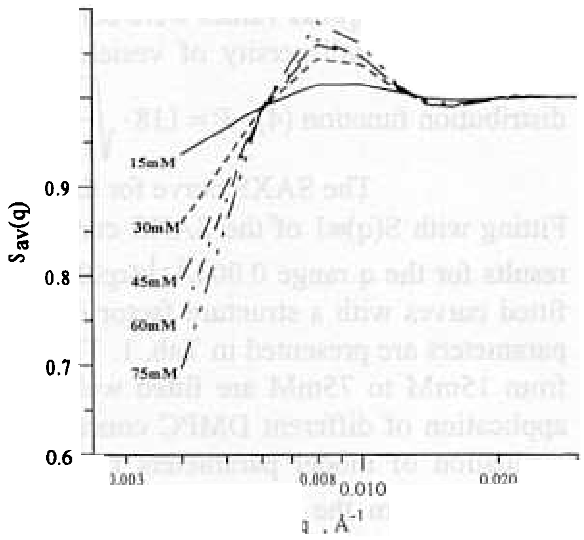

Fig. 2. The average structure factor of vesicles $S_{av}(q)$ calculated by the Debye model with the Schulz distribution for the 15mM, 30 mM, 45 mM, 60mM, and 75mM DMPC concentrations at T=30°C.

Acknowledgements: This study was supported by the TMR program for Large Instruments.

References

[1] Vesicles. ed. M. Rossoff. Marcel Dekker, Inc. 1996.

[2] A. Nagayasu, K. Uchiyama, and H. Kiwada. Adv. Drug Delivery Rev. 40 (1999) 75-87.

[3] J.F. Nagle, S. Tristram-Nagle. Biochim. Biophys. Acta 1469 (2000) 159-195.

[4] H. Schmiedel, P. Joerchel, M. Kiselev, G. Klose. J. Phys. Chem. 105 (2001) 111-117.

[5] J. Pencer, R. Hallet. Phys. Rev. E 61 (2000) 3003-3008.

[6] P. Lesieur, M.A. Kiselev, L.I. Barsukov, D. Lombardo. J. Appl. Cryst. 33 (2000) 623-627.

[7] M.A. Kiselev, P. Lesieur, A.M. Kisselev, D. Lombardo, M. Killany, S. Lesieur, M. Ollivon. Nucl. Instr&Methods A (2000), accepted for publication.

NEUTRON WAVE CHANNELING IN THE STRUCTURE Cu(30nm)/Ti(150nm)/Cu(100nm)/glass

V.L. Aksenov[a], Yu.V. Nikitenko[a], A.V. Petrenko[a], V.V. Proglyado[a],
F. Radu[b], V. G. Syromyatnikov[c]

[a]*Frank Laboratory of Neutron Physics, Joint Institute for Nuclear Research,*
141980 Dubna, Moscow Region, Russia
[b]*National Institute of Physics and Nuclear Engineering, Department of Experimental Physics,*
76900, P.O. Box MG-6, Magurele, Romania
[c]*Petersburg Nuclear Physics Institute, Russian Academy of Sciences, 188350, Gatchina, St. Petersburg, Russia*

Propagation of neutrons in a channel with a nanometric cross section is a wave process (neutron wave channeling). A potential application of the channeling effect may be the creation of a highly collimated neutron beam with a super-narrow cross section (100 nm in diameter). The neutron guide is a matter-channel layer enveloped in layers, the walls, whose material has an optical density higher than that of the matter of the channel. Neutron waves propagate through the channel reflecting from the walls. Attenuation of the propagation is due to decoherence of the neutron wave possibly resulting from the curvature or changing of thickness of the channel and the roughness of the interface. In this connection, an important application of channeling is the study of violations in the rectilinearity of the interface in the length of the structure. In [1-2] experiments of neutron wave channeling in the structures $(SiO_2+TiO_2)/Ti/Si$ and $Co_{0.95}Zr_{0.05}/Al/\ Co_{0.95}Zr_{0.05}$ are discussed. In the experiments an increase in neutron transmission over the neutron guide was observed for a wave vector on the order of 10^{-2} Å^{-1}. The authors of the experiment claim that the growth of transmission is due to formation of a neutron wave with an increased amplitude caused, in its turn, by the coherent summation of 2π-multiple neutron waves with different amplitudes. The factor of growth of the amplitude of the resulting neutron wave in the neutron guide increases as the wall thickness of the neutron guide grows. At the same time, the beam divergence decreases together with a decrease of the wavelength interval over which it happens. This results in the growth of the influence of decoherent processes on the wave propagation and as a result, in a rise of the sensitivity of measurements to the probability of such processes. To study the channeling processes, the structures Cu(30nm)/Ti(150nm)/Cu(100nm)/glass (Fig. a.) and Cu(30nm)/Ti(150nm)/Cu(100nm) /glass with a 30 mm cadmium angle piece on the surface of the structure (Fig. b.) were chosen.

The structures were illuminated with a collimated neutron beam at a glancing angle of 2.55 mrad, the mean square deviation of the glancing angle being 20 μrad. The neutrons tunneled through a 30 nm copper layer into the titanium layer where they propagated.

Figure c. illustrates the dependence of the neutron reflection coefficient R(η) on the perpendicular wavelength component $\eta = \lambda/\theta$ in the first structure. For η equal to 0.74, 0.91 or 1.58 Å/mrad, resonance downfalls (dips) on the reflection coefficient curve are seen (narrower dips, although not seen in the figure, also exist at $\eta < 0.74$). The dips are due to increasing neutron density and the related growth of neutron absorption in the titanium channel. Estimates show that the neutron density is reduced two times due to neutron absorption in the channel but at the same time, around the dips marked "2" it is 50 times larger than the density of neutrons in the incident beam. Figures d., e., f. show the dependence of the neutron transmission in the second structure T(η) for the summation of counts over three, two or one channel of the detector, respectively (one channel equals 0.69 mm of the sensitive area of the linear detector, which corresponds to an angular interval of 0.26 mrad, the spatial resolution of the detector being on the order of 1.5 mm). From the results illustrated in Fig. d. it is seen that the large transmission maximums marked with "1", "2" or

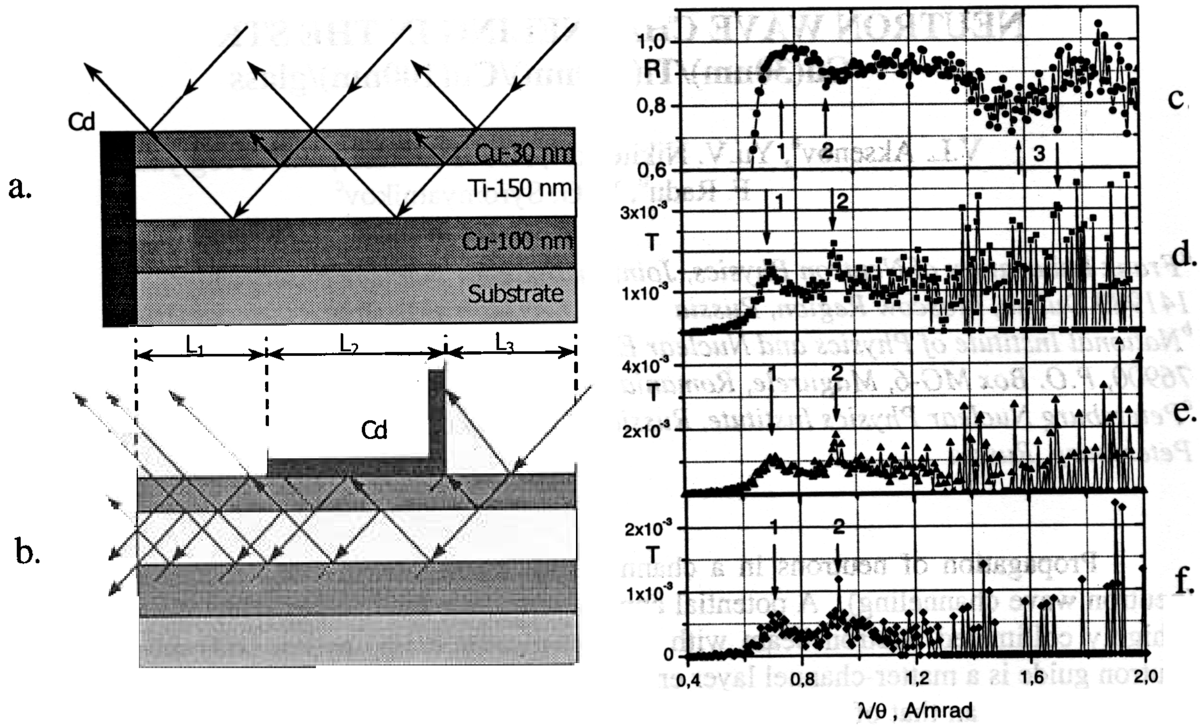

"3" are observed for η equal to 0.71, 0.93 or 1.67 Å/mrad. In the vicinity of the maximums "2" and "1" one will also see transmission oscillations with a smaller amplitude. The maximum "2" in Fig. d. virtually coincides with the minimum "2" in Fig. c. Thus, it is obvious that this maximum on $T(\eta)$ is also due to an increase in the neutron density in the titanium channel. The maximum "1" in Fig. d. shifts (by 4%) with respect to the minimum at 0.74 Å/mrad in Fig. c. The maximum "3" in Fig. d. is extremely narrow and shifts (by 6%) from the center of the wide maximum at 1.58 Å/mrad in Fig. c. The entire process of channeling is as follows. In the 35 mm section of the titanium layer prior to cadmium a wave with an increased amplitude is formed at certain values of η. Then, in the titanium layer under the cadmium the neutron wave propagates and its amplitude decreases. In the 35 mm section of the titanium layer behind the cadmium the wave exits through the surface (tunneling through the copper layer) and through the exit cross section of the channel. In Fig. d. it is seen that the transmission maximums are on the background which increases linearly as η increases. Obviously, the magnitude of the background is determined by the flux of the incoherently propagating neutrons. It is seen that as the divergence of the registered neutrons decreases (Figs. e. and f.) the background decreases and equals a third of the peak for the data in Fig f. The transmission peaks themselves are of the order of 10^{-3}, which is about ten times larger than the intensity peaks observed in [1,2] and is caused by a higher neutron density in the channel because of a three times larger thickness of the first copper layer. Thus, the resonance modes corresponding to neutron channeling in the titanium layer at a distance larger than 30 mm are obtained.

1. Y.P. Feng, C.F. Majkrzak, S.K. Sinha, D.G. Wiesler, H. Zhang, H.W. Deckman, Phys. Rev. B 49 (1994) 10814.
2. A. Menelle, S.P. Pogossian, H.Le Gall, J.M. Desvignes, J. Ben Youssef, Physica B 234-236 (1997) 510.

NEUTRON SPATIAL BEAM-SPLITTING AND POLARIZATION ANALYSIS IN REFLECTOMETRY

V.L. Aksenov, S.V. Kozhevnikov, and Yu.V. Nikitenko

*Frank Laboratory of Neutron Physics, Joint Institute for Nuclear Research,
141980 Dubna, Moscow Region, Russian Federation*

Magnetically anisotropic layered structures are attractive because of their extended applications. Improvement of the methods of their investigation is thus an important problem. At reflection or refraction on the interface of magnetically noncollinear media neutrons experience spin-flip followed with spatial splitting of the neutron beam [1-5]. In [5] it is noted that a combined use of polarization analysis and the effect of beam splitting increases the efficiency of polarization measurements. This paper presents a more detail study of the problem.

The measurements were conducted with the SPN-1 spectrometer at the IBR-2 reactor in Dubna. The experimental setup comprises a polarizer, a spin-flipper in front of the sample, a spin-flipper behind the sample, an analyzer, and a position-sensitive detector (PSD). The sample is a magnetic film of Co (700 Å) on a glass substrate. The size of the sample is 100×50×5 mm^2. An external magnetic field of 220 Oe and 3.5 kOe is applied at an angle of β=80^0 to the plane of the sample. The spatial resolution of PSD is 1.5 ÷ 2.5 mm [6]. The glancing angle of the incident beam and the sample to detector distance changed and were θ_0=6.10±0.30 mrad and θ_0=3.17±0.10 mrad, and 3 m and 8 m, respectively.

The polarization efficiencies of the polarizer and analyzer are different from unity, which reduces the efficiency of the polarization analysis method [7]. Figures 1 a,b depict the neutron intensity distribution as a function of the glancing angle of the reflected beam θ (the wavelength interval is 2.55 ÷ 6.67 Å, θ_0=3.17 mrad). The indices 1 and 2 mark the regions of off-specular reflection and the index 3 stands for the specular reflection region. In a parallel external magnetic field (black circles) the spin-flip effect is absent but the intensity of the reflected neutrons in the "off,on" regime of the spin-flippers is different from zero in the specular reflection region 3. This is a background intensity in the measurement of spin-flip-related coefficients. It is seen that in the off-specular region the background decreases 30 times. In an inclined magnetic field (open symbols) neutron spin-flip is present. However, since the external field is small (Fig. 1a) the splitting is weak and all the beams lie in the specular region. In a strong external magnetic field (Fig. 2b) spin-flip neutrons experience off-specular reflection. Figures 2 a,b show the reflectivities in the off-specular regions 1 and 2 in the field 3.5 kOe (θ_0=6.10 mrad). It is seen that neutrons that experience the spin transition "+-" are reflected to region 1 while "-+" transition neutrons are reflected to the region 2.

In the specular region (Fig 1a) the *effect/background* ratio is η=(0.6-0.25)/0.25=1.4, where the "effect" is the spin-flip-related intensity of neutrons. In the off-specular region (Fig. 1b) for the "off,on" neutrons at 4.3 mrad η=(0.2-0.01)/0.01=20 while for the "on,off" neutrons at 2.0 mrad η=(0.08-0.008)/0.008=10. So, as is seen at beam splitting the effect decreases about three times, but the effect to background ratio increases about ten times. Obviously, the efficiency of measurements in the off-specular reflection region increases the more the smaller the *effect/background* ratio in the specular region. For example, if η=1/10, the measuring time decreases 10 times.

On the other hand, in the off-specular region beam polarization grows. Figures 2 c,d show the beam polarization at the exit of the polarizer P and the neutron beam polarization behind the sample P_s at off-specular reflection (for the transition "+-" the polarization is negative and the polarization dependence is shown with an opposite sign in the Figure). It is seen that the neutron beam polarization at the exit of the polarizer decreases as the neutron wavelength grows while the polarization of neutrons reflected from the sample increases with growing neutron wavelength and tends to unity.

Thus, a combined use of total polarization analysis and neutron beam spatial splitting increases significantly the efficiency of neutron reflection measurements from magnetically noncollinear structures.

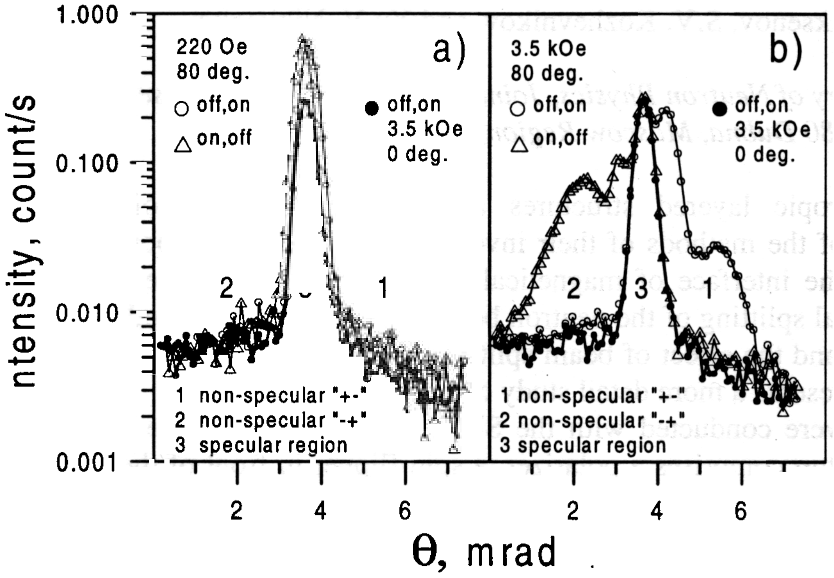

Fig.1. The neutron intensity as a function of the glancing angle of the reflected beam over the wavelength interval 2.55-6.67 Å.

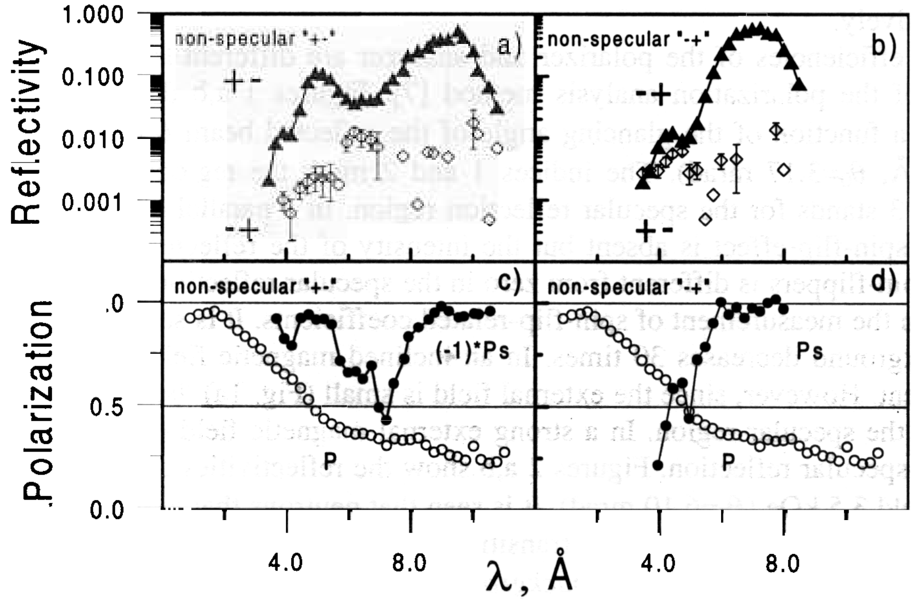

Fig. 2. The reflectivities (a,b) and the polarization degree of the beam (c,d) as a function of the neutron wavelength. *P* is the polarization of the beam falling on the sample; P_s is the polarization of the beam reflected from the sample.

[1] V.K. Ignatovich, Lett. JETP **28** (1978) 311 (in Russian).

[2] N.K. Pleshanov, Z. Phys. **94** (1994) 233.

[3] G.P. Felcher, S. Adenwalla, V.O. de Haan, A.A. van Well, Phys. **B 221** (1996) 494.

[4] V.L. Aksenov, E.B. Dokukin, S.V. Kozhevnikov, Yu.V. Nikitenko, A.V. Petrenko, J. Schreiber, Physica **B 234-236** (1997) 513.

[5] V.L. Aksenov, Yu.V. Nikitenko, S.V. Kozhevnikov, Phys. **B 297** (2001) 94.

[6] O.V.Fateev, G.A.Cheremukhina, S.P.Chernenko, Yu.V.Zanevskii, H. Lauter, V.V.Lauter, S.V.Kozhevnikov, Yu.V.Nikitenko, A.V.Petrenko, The position-sensitive detector for the spectrometer of polarized neutrons, Pribory i Tekhnika Experimenta **2** (2001) (in print).

[7] H. Fredrikze, R.W.E. van de Kruijs, Phys. **B 297** (2001) 143.

RBS INVESTIGATION OF MULTYLAYER STRUCRURES

A.P.Kobzev, A.Z.Kiss[a], A.Simon[a]

[a]*Institute of Nuclear Research of the Hungarian Academy of Sciences (ATOMKI),*
H-4001 P.O. Box 51, Debrecen, Hungary

Artificial, synthetic compositionally modulated materials, such as Si/Ge multylayers, are not equilibrium structures. In particular, they have high interfacial gradients and sufficient atomic mobility, therefore changes in the composition profile are expected to occur even at moderate temperatures. The mechanism of their diffusion homogenization is still indefinite. First of all, the diffusion asymmetry (manifested in strong concentration dependence of interdiffusion coefficients) and strong porosity formation during diffusion mixing are the most important factors indicating the need of a better understanding of the above-mentioned process. Stability of the material, its resistance to composition changes, is obviously of importance for practical applications.

A study of the interdiffusion of the elements in amorphous Si/Ge multilayers has been carried out in cooperation with ATOMKI and the Department of Solid State Physics in Debrecen as part of a Co-ordinated Research Program of the International Atomic Energy Agency. This report is devoted to the studying of the elemental depth distributions in the amorphous Si/Ge multilayer structures prepared by DC magnetron sputtering from alternating elemental target onto (001) silicon wafers at the Department of Solid State Physics, University of Debrecen.

Si, Ge and O depth profiling in the Si/Ge multilayer structure consisting of 5 bilayers has been performed by the RBS and NRA methods[1,2]. The determination of the depth profiles of oxygen atoms in the investigated samples was carried out using the $^{16}O\ (\alpha,\alpha)^{16}O$ nuclear reaction. A number of spectra were measured for the different angles of the incident beam with respect to the surface of the samples (φ ranging from 5^0 to 60^o) with 3.112 MeV helium ions.

Some of the measured spectra are shown in Fig.1. All silicon and germanium layers are seen in the spectrum as the separated peaks for $\varphi=6^o$. But the depth resolution is worse for deeper layers because of energy struggling. Nevertheless a layered structure with degraded interfaces is observed. From our analysis it is seen that all layers contain some oxygen impurity (10-13%), and a definite SiO_2 layer with a thickness of 177Å situated between the multilayer structure and the Si wafer is revealed. The oxygen peak shown in Fig. 1 corresponds to it (spectrum B). A sharp resonance in the $^{16}O\ (\alpha,\alpha)^{16}O$ reaction for the 3.045 MeV is observed for all incident angles except φ=60° (spectrum A, fig.1). For this incident angle and an initial energy of 3.112 MeV of ^{4}He ions resonance occurs in an oxygen free substrate.

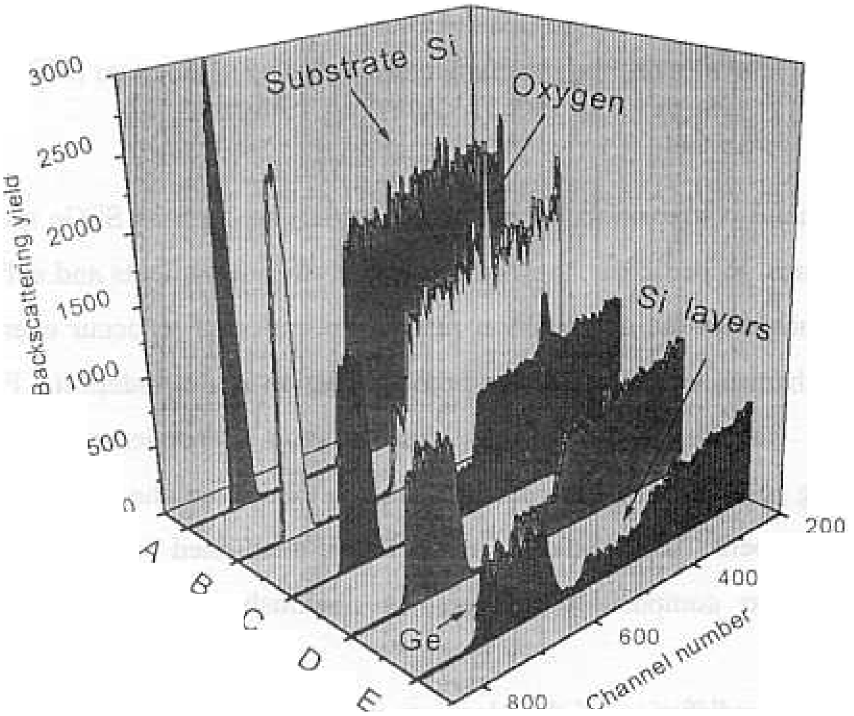

Fig.1 The backscattering spectra for the Si/Ge multylayer structure.
The incidence angle $\varphi = 6^o$ – A, $\varphi = 10^o$ – B, $\varphi = 20^o$ – C, $\varphi = 40^o$ – D, $\varphi = 60^o$ – E.

Modelling has allowed us to determine the full thickness of the Ge-layer which is about 130 Å and that of the Si layer to be about 231 Å, including the mixed layers with the thickness 64.7 Å. It is essential that the same model has been used for the description of all the experimental spectra obtained at different incident angles. So, a complete structure of the sample has been reconstructed by this non-destructive technique.

Another sample consisting of three Si/Ge bilayers was investigated by the RBS method at an energy of 1 MeV. A better depth resolution has been reached because the stopping power increases for lower energies of ^{4}He ions. Figure 2 shows both the experimental and simulated spectra of ^{4}He ions scattered back at 170°, for an incident angle to the target surface of 10°, where the best resolution has been obtained. As it is seen there is fairly good agreement between the experimental and calculated spectra (every detail for an energy resolution of ΔE=15 keV). The elemental depth distribution derived from the RBS spectra is shown in the table.

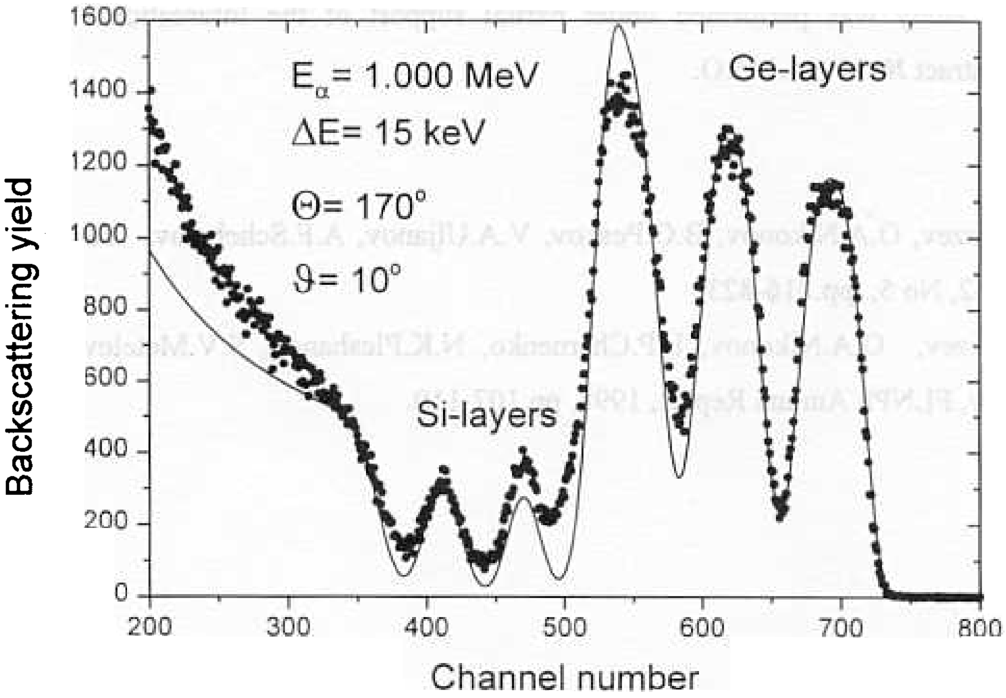

Fig. 2. The experimental (points) and calculated (line) backscattering spectra for three Si/Ge bilayer sample.

Depth Å	Element Concentrations (at %)	
	Ge	Si
100.5	0.00	100.0
147.2	50.0	50.0
296.3	100.0	0.00
343.1	50.0	50.0
429.5	0.00	100.0
476.3	50.0	50.0
618.5	100.0	0.00
665.3	50.0	50.0
755.7	0.00	100.0
802.5	50.0	50.0
942.5	100.0	0.00
989.3	50.0	50.0
2000	0.00	100.0

The thickness of the full period obtained from this measurement is 320 Å. It consists of a Ge layer with a thickness of 143 Å, a Si layer with a thickness of about 90 Å and two layers of mixed content with a thickness of about 47 Å. As interdiffusion at room temperature is practically zero, the mixed layer refers to surface roughnesses.

This study was performed under partial support of the International Atomic Energy Agency, contract № 10036.1/ RO.

References

[1] A.P.Kobzev, O.A.Nikonov, B.G.Peskov, V.A.Uljanov, A.F.Schebetov. Yadernaya Fizika. 1999, Vol. 62, No 5, pp.816-823.

[2] A.P.Kobzev, O.A.Nikonov, L.P.Chernenko, N.K.Pleshanov, S.V.Metelev, A.F.Schebetov, V.A.Uljanov, FLNPh Annual Report, 1998, pp.107-110.

SURFACE EXCITATIONS IN THIN HELIUM FILM IN SILICA AEROGELS.

I.V.Bogoyavlenskii, A.V.Puchkov, H.J.Lauter*, and Andrei Skomorokhov

Institute for Physics and Power Engineering, 249020, Bondarenko sq.1, Obninsk, Russia
Institute Laue Langevin, F-38042, Grenoble Cedex 9, France

Liquid helium attracts the attention of experimentalists and theorists nowadays even more than as previously. The long term studies of the excitation spectrum of bulk liquid helium on DIN-1M, DIN-2PR, and DIN-2PI spectrometers (IBR-30 and IBR-2 reactors) brought interesting results [1] in parallel with the investigations at other neutron centres. During the last years the interest in this field widened from bulk helium to helium in confined geometries. So properties of helium in porous media like exfoliated or powdered graphite, zeolites, sponge, vycor glass, aerogels, and xerogels were explored. It turns out that liquid helium properties in porous media differ from those of bulk helium and depend on geometrical parameters and type of porous media [2]. It appears that the surface properties of the media have great influence on the helium adjacent to the confinement. Neutron scattering studies of thin liquid helium films on different substrates are started now to get an understanding of these properties

Neutron scattering data, taken from helium films on graphite show the existence of the ripplons at the liquid-gas interface of the film and of excitation, which have the character of 2-dimentional rotons at the solid-liquid interface of the film, called layered-phonon-roton modes [3]. In very thin films only these two excitations may exist, whereas in the example of a 4-monolayer film parts of the bulk phonon-roton curve are visible.

The interest to study the excitations in a ^{4}He film adsorbed on silica aerogel is, that ^{4}He films in the aerogel shows a different behavior compared to films on other substrates as e.g. graphite. Apart from this, bulk helium in aerogel, graphite or vycor shows a different exponent for the temperature dependence of the superfluid component near the lambda-transition. This may be related again to the different interface properties of the helium film excitations on the fractal aerogel surface.

The results presented here are the first attempt of the investigation of liquid helium films on the DIN-2PI spectrometer.

The incident neutron energy was 2.58 meV. The range of scattering angles and of momentum transfers was 11° - 133° and 0.2-2.0A^{-1}, respectively. The aerogel sample had been annealed at 600C under a pressure of ~10^{-4} torr during 3 days. The MAX ORANGE cryostat has been used together with the special sample-stick for the filling of the aerogel sample with helium gas under pressure-temperature control. The measurement was carried out at a sample temperature of T=1.55K. Three different coverages have been tested: corresponding to a monolayer (20 l of normal pressure helium gas), a 2-3 layer film (58 l), and a filling of 68 l, a coverage at which the signal from the bulk roton is just appearing. It should be mentioned that the first layered part of the helium film adjacent to the aerogel substrate is amorphous and is added to the aerogel substrate.

Fig.1 shows the experimental dynamic structure factor of aerogel+helium at constant angle at T=1.55K. No background was subtracted. The scattered intensity at the angle of 133° picks up the signal from the roton region near the momentum transfer of $Q=1.9A^{-1}$. At T=1.55K the energy of the bulk roton (BR) and the layer roton (LR) are very close. Perhaps the influence of the bulk roton appears already at the 58 l-coverage due to its high intensity.

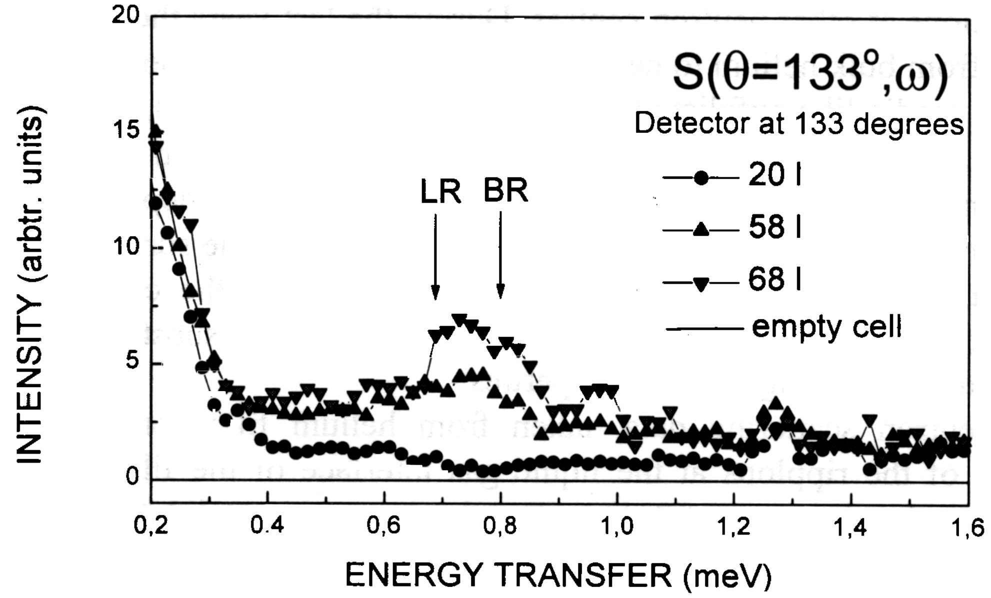

Fig.1. Experimental dynamic structure of a thin 4He film adsorbed on silica aerogel for three coverages at T=1.55K. No difference between the 20 l-coverage spectrum and the empty cell spectrum was found. The scattering angle corresponds to a momentum transfer near the "roton minimum". No background was subtracted. Arrows mark the values of the bulk roton (BR) energy [3] and the layer roton (LR) energy [3].

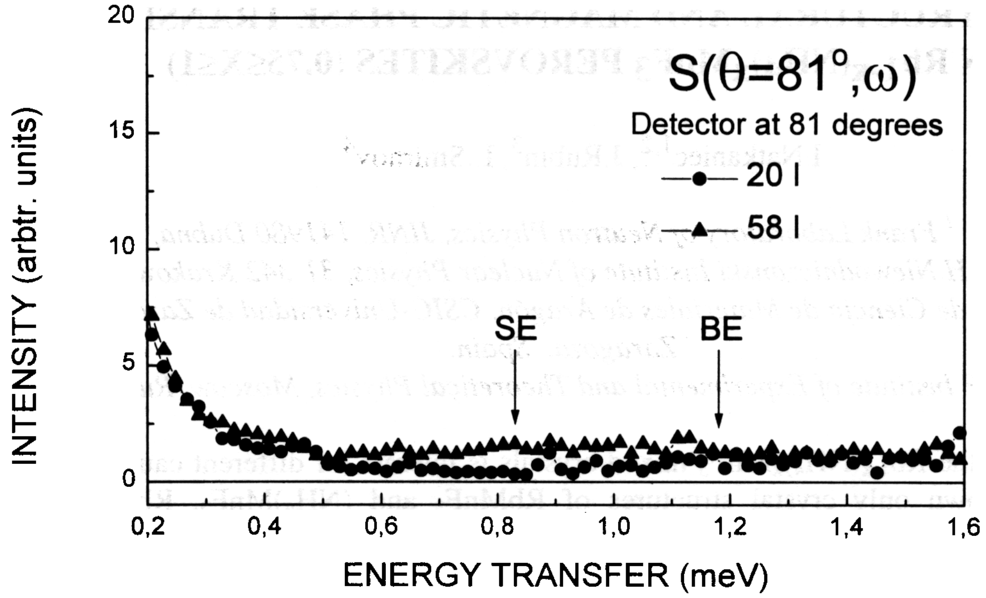

Fig.2. Experimental dynamic structure of thin 4He film adsorbed at silica aerogel for two coverages at T=1.55K. The scattering angle corresponds to a momentum transfer near the "maxon" region. The energy values of the bulk excitation (BE) [4] and the surface excitation (SE) [3] differ considerably. No background was subtracted.

The first experiment on the DIN-2PI spectrometer with thin helium films shows the good performance of this spectrometer even without cold source. In particular the very low background is an absolute necessary feature to observe the very small signals.

REFERENCE

1. I.V.Bogoyavlenskii, A.V.Puchkov and A.Skomorokhov, "The association between temperature dependence of liquid ^{4}He scattering law and the phenomena of the Bose condensation", Physica B276-278 (2000) 465.
2. M.Chan, N.Mulders and J.Reppy, Physics Today (August 1996) 30.
3. B.Clements, H.Godfrin, E.Krotscheck, H.J.Lauter, P.Leiderer, V.Passiouk, "Excitations in a thin liquid ^{4}He film from inelastic neutron scattering", Phys.Rev.B53 (1996) 12242.
4. I.V.Bogoyavlenskii, A.V.Puchkov, A.N.Skomorokhov and S.V.Poupko, "Neutron scattering study of ^{4}He *S(Q,w)* at the phonon-maxon region", Physica B234-236(1997)324.

STRUCTURAL AND MAGNETIC PHASE TRANSITIONS IN $Rb_{1-x}(NH_4)_xMnF_3$ PEROVSKITES ($0.75 \leq X \leq 1$)

I.Natkaniec[1,2], J.Rubin[3], L.Smirnov[4]

[1] *Frank Laboratory of Neutron Physics, JINR, 141980 Dubna, Russia*
[2] *H.Niewodniczanski Institute of Nuclear Physics, 31-342 Krakow, Poland*
[3] *Instituto de Ciencia de Materiales de Aragón, CSIC-Universidad de Zaragoza, Zaragoza, Spain.*
[4] *SSC RF Institute of Experimental and Theoretical Physics, Moscow, Russia.*

The study of the $Rb_{1-x}(NH_4)_xMnF_3$ mixed crystals is interest for different causes. Until recent time there are known only crystal structures of $RbMnF_3$ and $(NH_4)MnF_3$. $RbMnF_3$ has the cubic perovskite structure (space group Pm3m, Z=1) with Rb ion at the body centre which is surrounded by 12 ions of F on the cube edges and 4 ions of Mn on the cube vertex. $RbMnF_3$ do not undergo the phase transition in wide interval of the temperature from 50 to 300 K [1,2]. $(NH_4)MnF_3$ is isomorphous to $RbMnF_3$ at high temperatures but undergoes phase transition at 183 K from orientational disordered cubic phase to the orientational ordered orthorhombic crystal structure with space group Pnma, Z=4 [3,4]. Ionic radii of ammonium and rubidium are very close and on the one hand it is possible to expect that $RbMnF_3$ and $(NH_4)MnF_3$ will form the solid solution in wide concentration region. On the other hand by the analogy with the mixed crystals of the type of $K_{1-x}(NH_4)_xI$ [5], $K_{1-x}(NH_4)_xSCN$ [6], $Rb_{2-x}(NH_4)_xSO_4$ [7] it is possible to expect that the $Rb_{1-x}(NH_4)_xMnF_3$ mixed crystals will form the phase diagram with the region of orientational glass at low temperatures.

The measurements of the inelastic incoherent neutron scattering (IINS) and neutron powder diffraction (NPD) are carried out on the $Rb_{1-x}(NH_4)_xMnF_3$ mixed crystals with the concentrations x=0.75 and 1.0 at 20, 100 and 200 K. The NPD spectra and the IINS spectra for $(NH_4)MnF_3$ at 25, 100 and 200K are presented in Figs. 1 and 2(a,b). The NPD spectra are measured at different Bragg angles in order to have the possibility to obtain diffraction spectra with good resolution and to fix crystal structure transformation with the help of the detector at big Bragg angle and to obtain magnetic reflection on big interplane distances with the help of the detector on small Bragg angle.

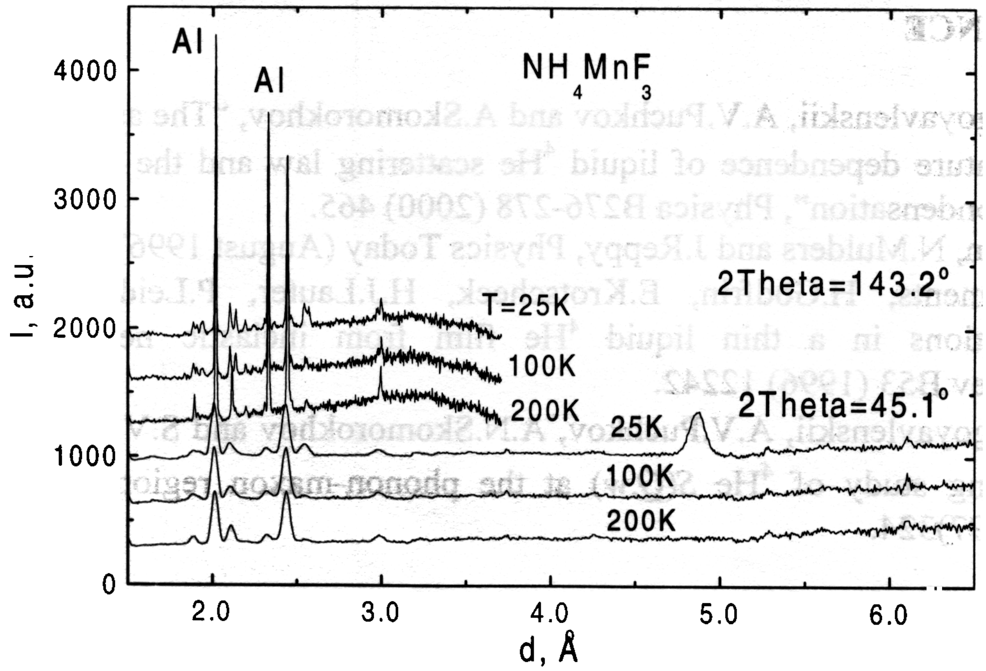

Fig. 1. The NPD spectra from $(NH_4)MnF_3$ at different temperatures and Bragg angles.

In accordance with determined crystal stuctures of different phases of $(NH_4)MnF_3$in [4] diffraction profile of NPD at 200 K is satisfactorily described by cubic perovskite structure with lattice parameter *a*=4.2364 Å, at 100 K it is described by orthorhombic lattice with parameters *a*=5.9539, *b*=8.5572 and *c*=5.9585 Å and at 25 K magnetic orthorhombic phase is observed with lattice parameters *a*=5.9524, *b*=8.5579 and *c*=5.9577 Å. Magnetic reflections are observed near 4.8 and 2.5 Å, showing antiferromagnetic ordering.

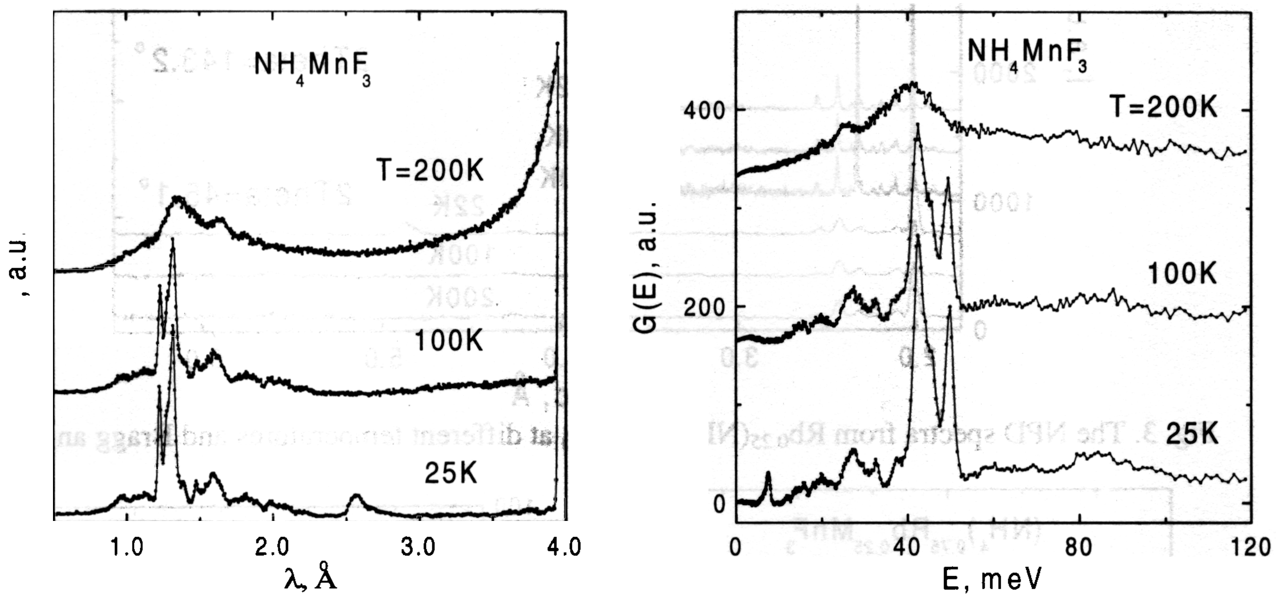

a) b)

Fig. 2. The IINS spectra (a) and G(E) spectra (b) for $(NH_4)MnF_3$ at different temperatures.

The IINS spectrum of $(NH_4)MnF_3$ at 200 K has the significant contribution of quasielastic incoherent neutron scattering (QINS) (see Fig. 2a) that confirms that in the cubic phase ammonium ions are orientationally disordered. The contribution of QINS intensity is absent in the IINS spectra at 100 and 25 K that is confirms orientational ordering of ammonium ions in the orthorhombic phase. The spectra of generalized phonon density of states G(E) for $(NH_4)MnF_3$ at 25, 100 and 200 K are presented in Fig.2b. At temperatures 25 and 100 K in orthorombic phase G(E) presents in energy region 10-35 meV the translational lattice modes and in the energy region 35-50 meV the librational modes in accordance with the results of [4]. However there is difference between G(E) spectra at 25 and 100 K which is concluded in the absence of assymetric peak near 7.6 meV. If one take attention that difference between NPD spectra of $(NH_4)MnF_3$ at 25 and 100 K is in the absence of magnetic reflections so it is possible to do the conclusion that the energy near 7.6 meV can be described to magnetic excitations or spin wave modes..

The substitution of 25% ammonium ions by rubidium in $(NH_4)MnF_3$ do not change the succession of phase transitions from orientational disordering cubic perovskite phase to orientational ordering orthorhombic phase with successive magnetis phase transition in antiferromagnetic phase. This conclusion succeeds from the NPD spectra obtained at 200, 100 and 22 K and are presented in Fig.3. The spectra of IINS intensities and G(E) of $Rb_{0.25}(NH_4)_{0.75}MnF_3$ are presented in Fig. 4(a,b) respectively. The IINS and G(E) spectra for $Rb_{0.25}(NH_4)_{0.75}MnF_3$ are analogous to appropriate spectra of $(NH_4)MnF_3$ but at 22 and 100 K its are more smeared. The energy of spin wave mode is approximately 7.9 meV. Earlier authors of [8] measured spin-wave dispersion relation for $RbMnF_3$ and obtained approximate value of the energy on the boundary of Brillouein zone 8.6 meV. If one takes attention that Neel temperature for $RbMnF_3$ is higher than for NH_4MnF_3 then the value 7.6 meV is real for spin wave energy of NH_4MnF_3 on the boundary of Brillouin zone.

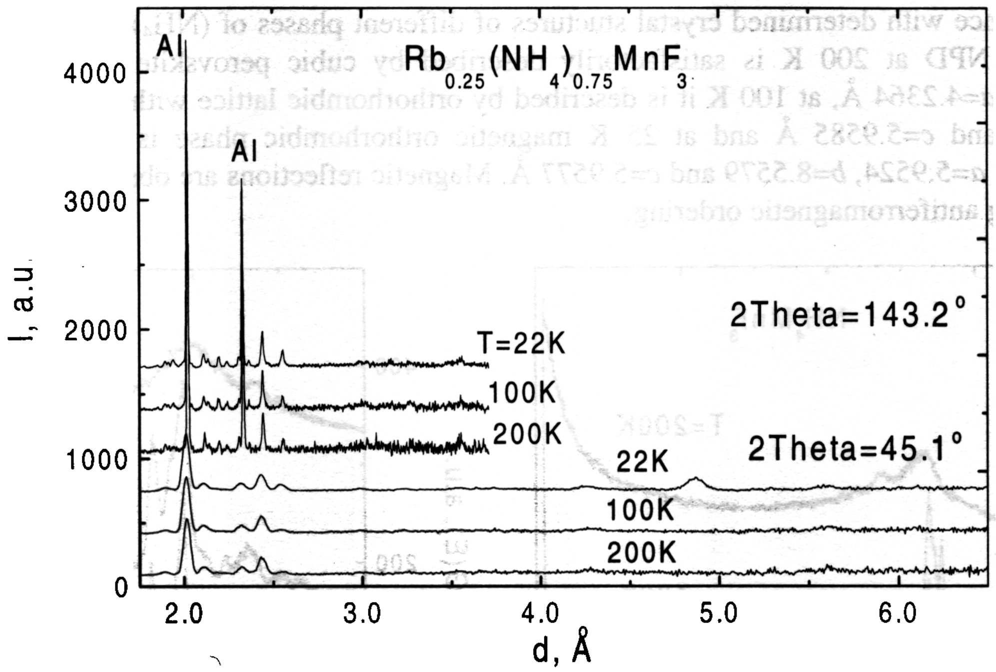

Fig. 3. The NPD spectra from $Rb_{0.25}(NH_4)_{0.75}MnF_3$ at different temperatures and Bragg angles.

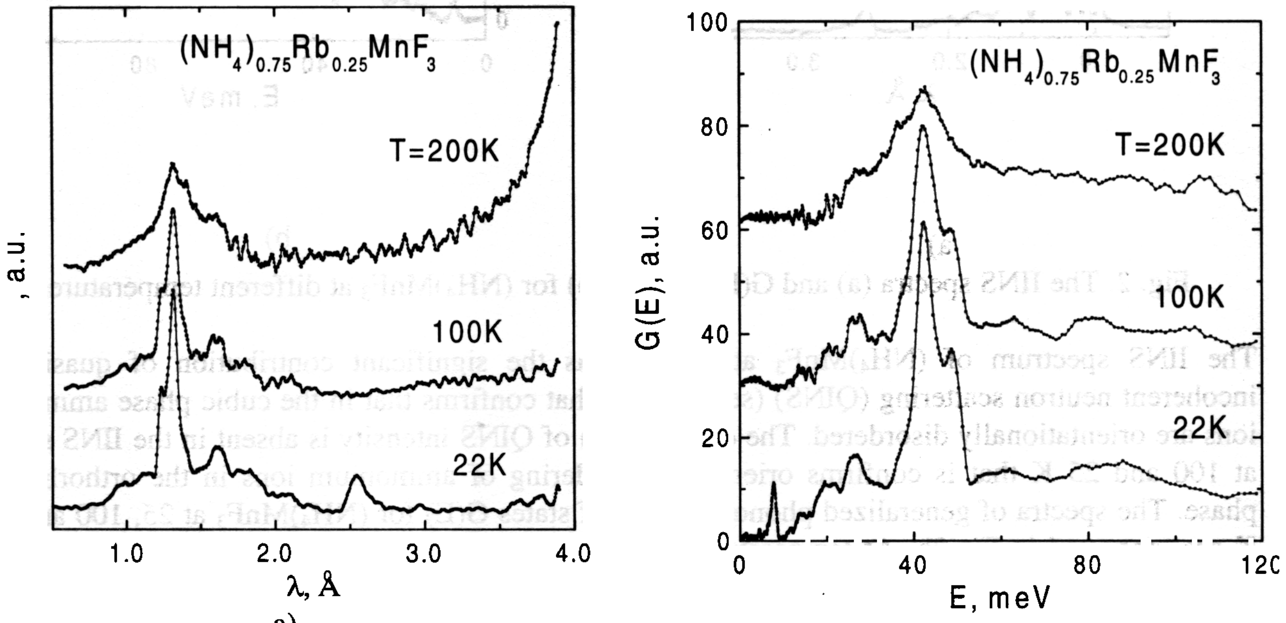

a)

b)

Fig. 4. The IINS spectra (a) and G(E) spectra (b) for $Rb_{0.25}(NH_4)_{0.75}MnF_3$ at different temperatures.

References:

1. C.G.Windsor, R.W.H.Stevenson, Proc.Phys.Soc., **87**, 501 (1966).
2. D.T.Teaney, V.L.Moruzzi, B.E.Argyle, J.Appl.Phys., **37**, 1122 (1966).
3. M.A.Laguna, M.L.Sanjuan, V.M.Orera, J.Rubin, E.Palacios, M.C.Pique, J.Bartolome, J.F.Berar, J.Phys.:Condens.Matter, **5**, 283 (1993).
4. J.Rubin, E.Palacios, J.Bartolome, J.Rodriguez-Carvajal, J.Phys.:Condens.Matter, **7**, 563 (1995).
5. I.Natkaniec, L.S.Smirnov, Physica B **234&236** (1997) 409-411.
6. I.Natkaniec, L.S.Smirnov, A.I.Solov'ev. Physica B **213&214** (1995) 667-668.
7. I.Natkaniec, M.L.Martinez-Sarrion, L.Mestres, L.S.Smirnov, L.A.Shuvalov, Physica B, Condens.Matter, **241-243**, 487 (1998).
8. C.G.Windsor, R.W.H.Stevenson, Proc.Phys.Soc., **87**, 501 (1966).

Phonons in coarse grained and plastically deformed vanadium

S.Danilkin[1], M. Jung[2], H. Wipf[2]

[1] *Institute of Physics and Power Engineering, 249020 Obninsk, Russia*
[2] *Technische Universitat Darmstadt, D-64289 Darmstadt, Germany*

Aim of the study was to observe changes in the vibrational density of states ($g(\varepsilon)$) of vanadium due to deviations from perfect crystalline order. We investigated differences in the $g(\varepsilon)$ between plastically deformed and well-annealed vanadium. Vanadium is most suitable material for measurements of $g(\varepsilon)$ because it scatters neutrons nearly exclusively incoherently.

The measurements were done with DIN-2PI spectrometer at incident energy of neutrons 10 meV in scattering angle range of 70 ÷ 130°. Samples were vanadium plate of 1 mm thickness and the same material after the cold deformation (90 %). The second sample was consisted of 10 plates to have the same total thickness as the annealed vanadium sample. The time-of-flight spectra of two vanadium samples normalised by the area of the elastic peak are shown in Fig. 1. The spectrum of the deformed vanadium has higher intensity in the low energy region at $\varepsilon \approx 4$ meV.

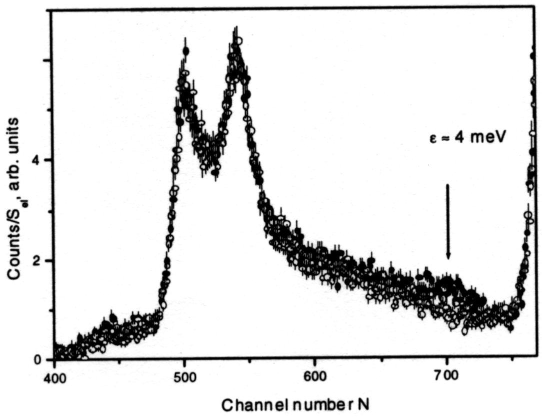

Fig. 1 INS spectrum of deformed (•) and annealed (#) vanadium

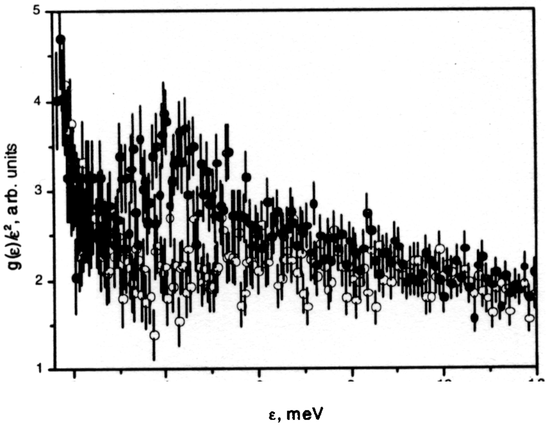

Fig. 2 Function $g(\varepsilon)/\varepsilon$ of deformed (•) and annealed (#) vanadium

These additional modes are also seen in the $g(\varepsilon)$ of deformed vanadium, but they are less pronounced there. To observe the deviation of $g(\varepsilon)$ from the Debye spectrum the function $g(\varepsilon)/\varepsilon^2$ was calculated for both samples (Fig. 2). This function for the annealed vanadium has a nearly linear behaviour in the energy range 2 ÷ 12 meV while that of deformed vanadium has a pronounced peak at $\varepsilon \approx 4$ meV. At frequencies lower then 2 meV the increase of intensity is connected with contribution from the elastic line. The similar excess soft modes designated as the "boson peak" were observed earlier in different glasses and amorphous alloys [1]. INS study of austenitic steels showed that an enhancement of the low-frequency VDOS may also be induced by cold plastic deformation - the distinct increase of the VDOS in the low-frequency range between 8 and 16 meV was observed after cold plastic deformation (70%) in Fe-18Cr-10Mn-16Ni-0.5N alloy [2]. Also these changes are in fact very similar to those found for nanocrystalline materials [3, 4] demonstrated recently that the low-frequency increase of the *g(ε)* results predominantly from atoms in or at grain boundaries or surfaces.

References

A. Meyer, J. Wuttke et al., Phys. Rev. B, **53**, 12107 (1996).

2. S.Danilkin, V.Minaev, V.Sumin: Preprint No. FEI-2371, 1994, Institute of Physics and Power Engineering, Obninsk, Russia.
3. U.Stuhr, H.Wipf, K.H.Andersen, H.Hahn, Phys. Rev. Lett. **81**, 1449 (1998)
4. A.Kara, T.Rahman, Phys. Rev. Lett. **81**, 1453 (1998)

Quasielastic scattering investigation of liquid phosphorus oxychloride $POCl_3$

A.G.Novikov[a], O.V.Sobolev[b]

[a]State Scientific Centre of RF – Institute of Physics and Power Engineering. 249020, Obninsk, Kaluga reg., Russia.

[b]Frank Laboratory of Neutron Physics, Joint Institute for Nuclear Research, 141980, Dubna, Moscow Reg., Russia.

In the frame of neutron scattering experiments on liquid $POCl_3$ [1] we have measured and analysed the quasielastic component of its common double-differential scattering cross section (DDSCS). The detail description of the procedure and results of analysis will be published [2]. Now we give short information, concerning with these questions.

For separation of quasielastic component from the total DDSCS and its subsequent analysis the following procedures were performed:

- time-of-flight DDSCS were transformed into energy scale and then by interpolation into the form $S(Q,\varepsilon)$ at Q = const, where $S(Q,\varepsilon)$ is the scattering law (or dynamic scattering function) and ε - energy transfer.;
- from the total DDSCS the inelastic contribution was removed; it was shown by calculations and practically [3,4], that for $S(Q,\varepsilon)$ in the vicinity of quasielastic peak the inelastic contribution can be considered as a flattened background with relatively small amplitude, so the approximation appropriate for $S(Q,\varepsilon)$ can be written:

$$S(Q,\varepsilon) = \{S_q(Q,\varepsilon) + [a + b\varepsilon]\} \otimes R(Q,\varepsilon) \qquad (1)$$

where the expression in square brackets represents inelastic scattering effects and sign $\otimes$ means the convolution of natural scattering law with resolution of spectrometer $R(Q,\varepsilon)$, measured by special vanadium sample.

The shapes and halfwidths (full width at halfmaximum, FWHM) of quasielastic peaks arise from a number of effects, including coherent and incoherent scattering, translation and rotation components of diffusion motions (the detail expressions for DDSCS of quasielastic scattering on molecular liquids with mixed (coherent and incoherent) scattering are given in [5,6]). It turned out, that in our case some alleviation takes place, because according to results of [7] on peak widening of Rayleigh scattering effects of rotation diffusion in liquid $POCl_3$ are expected to be negligible. This conclusion can be conformed by the estimation of rotation diffusion coefficient in liquid $POCl_3$ on the basis of Einstein – Stokes law for rotation motion [8]:

$$D = kT/8\pi\eta R^3 \qquad (2)$$

Substituting in (2) viscosity (for room temperature η = 1.06 cP [9]) and effective radius of $POCl_3$ molecule ($R_{eff} \approx 3$ A), we find: $D_{rot} \approx 1.3 * 10^{10}\ c^{-1}$ and

$$\Delta E_{rot} = 2D_{rot} * h \sim 0.02 \text{ meV}.$$

Keeping in mind the resolution of our spectrometer for elastic scattering ($\Delta E_o \sim 0.1 \div 0.13$ meV), we are led to conclusion, that these effects can not be observed under our experimental conditions. So, the later analysis of experimental quasielastic DDSCS will be performed under assumption, that we deal only with effects of translation diffusion. In so doing, we have supposed, the quasielastic peaks are superposition of two components, hypotically corresponding to coherent and incoherent contributions:

$$S_q(Q,\varepsilon) = \{1/\pi\Sigma_{i=1,2}\, c_i(Q)\Delta E_i(Q)/(\varepsilon^2+\Delta E^2{}_i)\} \otimes R(Q,\varepsilon), \qquad (3)$$

with their own Q-dependened weights and halfwidths $c_i(Q)$, $\Delta E_i(Q)$, which are shown on fig. 1 and 2. It follows from fig. 8, that the common integral intensity of quasielastic scattering (the sum of coherent and incoherent contributions: $c_1(Q)+c_2(Q) = \int_{-\infty}^{\infty} S_q(Q,\varepsilon)d\varepsilon$)) is not far from diffraction results [1].

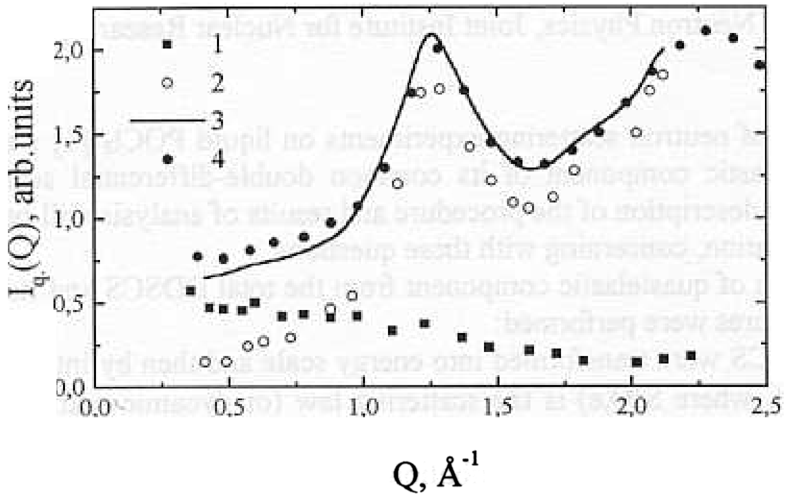

Fig. 1. Integral intensity of quasielastic scattering.
1 – incoherent component; 2 – coherent component; 3 – sum of coherent and incoherent components; 4 – angular differential scattering cross section (diffraction experiment, see [1]).

The curve 1 of fig.1 gives the integral intensity of incoherent quasielastic scattering, which can be expressed as [10]:

$$S_q(Q) \sim \Sigma_s/4\pi \exp\{-u^2Q^2\}\ , \qquad (4)$$

where $W = u^2Q^2$ is Debye - Waller factor and u^2 - mean – sqare amplitude of molecular vibration, infered from analysis of this curve, is:

$(u^2)^{1/2} = (0.55 \pm 0.05)$Å.

Now draw our attention to fig. 2. Curve 1 corresponds to the common halfwidth of quasielastic peak (in one-Lorentzian representation). The main contribution in the intensity of this peak arises from coherent scattering, so, its halfwidth demonstrates some evidence of oscillatory behaviour, being distinctive feature of coherently scattering liquids [11] (its first minimum coincides with the position of the fist structure factor maximum, Q ~ (1.2 – 1.3) A^{-1}, see [1]). We did not try to describe this curve by Scold model [12], because it contains a remarkable portion of incoherent scattering. Curve 2 of fig. 2 shows the halfwidth of incoherent quasielastic peak (two-Lorentzian representation). In small Q-region curves 1 and 2 are near each other (coherent effects are weak), but then they come apart, and curve 2 tends to flatten, what is commonly understood, as an evidence of jump diffusion process, which is distinctive for highly associated liquids. Fitting curve 2 by mixed diffusion model [13], assuming the diffusion process to be superposition of two mechanisms: continuous and jump ones, we get parameters of model: common selfdiffusion coefficient D, coefficient of collective diffusion (diffusion of particle together with nearest surrounding) D_o and the residence time of molecule at the temporary equilibrium position τ_0:

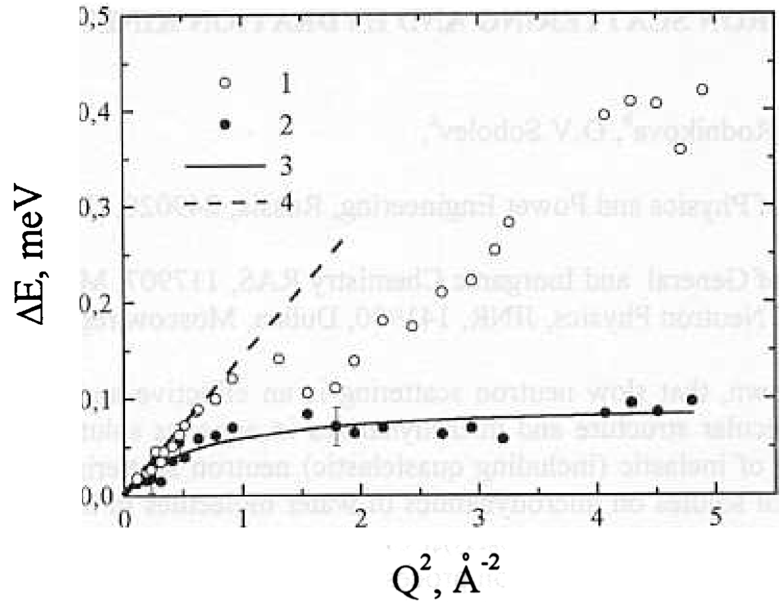

Fig. 2. Halfwidths of quasielastic peaks.
1 – common halfwidth of quasielastic peak (one – Lorentzian description); 2 – halfwidth of incoherent component of quasielastic peak; 3 – description of incoherent quasielastic peak halfwidth with the model of mixed diffusion.

$D = (2.3 \pm 0.8)\ \text{см}^2/\text{с}$;
$D_o \sim 0.02\ \text{см}^2/\text{с}$;
$\tau_0 = (7 \pm 1) * 10^{-12}$ с.

The sizable errors of the parameters given arise from the procedure of decomposition, as well as from restricted experimental statistics.

The work was performed under financial support of Russian Federation Program “Actual Directions in Condensed Matter Physics”, project “Neutron studies”.

References

1. A.Novikov, D.Seliverstov, O.Sobolev. Annual Reportn of FLNP, JINR, Dubna, 1999, p. 89-90.
2. A.Novikov, O.Sobolev. J. of Mol. Liquids. (in press).
3. S.Iskanderov, A.Novikov. Rus. J. Phys. Chem. 56 (1982) 1469.
4. A.G.Novikov, M.N.Ivanovskii, V.V.Savostin, A.L.Shimkevich, O.V.Sobolev, M.V.Zaezjev. J. Phys.: Cond. Matter. 8 (1996) 3525.
5. F.Bermejo, F.Batallant, E.Enciso, R.White, A.Dianoux, W.Howells. J. Phys.: Cond. Matt. 2 (1990) 1301.
6. F.Bermejo, M.Alvarez, M.Garcia-Hernandez at al. J. Phys.: Cond. Matt. 3 (1991) 851.
7. R.Pappalardo, A.Lempicki. J. Appl. Phys. 43(1972) 1699.
8. G.Sposito. J. Chem. Phys. 74 (1981) 6943.
9. K.C.Krasnov. Molecular constants of inorganic compounds. Leningrad, “Nauka”, 1977, 448 p., (in russian).
10. I.Gurevich, L.Tarasov. Low-energy neutron physics. North-Holland, Amsterdam, 1968, 608 p.
11. J.Copley, S.Lovesey. The Dynamic Properties of Monatomic Liquids. Rep. Prog. Phys. 38 (1985) 461.
12. K.Skold. Phys. Rev. Lett. 19 (1967) 1023.
13. V.Oskotskii. Sov. Phys. Solid State. 5 (1963) 789.

INELASTIC NEUTRON SCATTERING AND HYDRATION KINETICS IN AQUEOUS SOLUTIONS

A.G.Novikov[a], M.N.Rodnikova[b], O.V.Sobolev[c]

[a]SSC RF – Institute of Physics and Power Engineering, Russia, 249020, Obninsk, Kaluga reg., Russia.
[b]Kurnakov Institute of General and Inorganic Chemistry RAS, 117907, Moscow, Russia.
[c]Frank Laboratory of Neutron Physics, JINR, 141980, Dubna, Moscow reg., Russia

It is well known, that slow neutron scattering is an effective and adequate instrument for investigation of molecular structure and microdynamics in aqueous solutions. Last years we have performed a number of inelastic (including quasielastic) neutron scattering experiments, aimed to clarify an influence of solutes on microdynamics of water molecules in ionic (LiCl, CsCl, [1]) and hydrophobic ($(CH_3)_4NCl$, $(C_4H_9)_4NCl$, $(C_6H_5)_4PCl$, [2,3]) aqueous solutions. From results of these experiments the information about diffusion processes (coefficients of self- and collective diffusion, residence times of molecules, static and dynamic hydration numbers) and vibration-rotation dynamics (in the form of generalyzed frequency distribution, GFD) for water molecules, incorporated in hydration shells was extracted. Basing on these data the comparative analysis of ionic and hydrophobic hydration effects was performed with the conclusion, that the ionic hydration destroys the hydrogen bond network in surrounding water, and conversely hydrophobic one retains it to be untouched.

The dynamical information, above mentioned, corresponds to the equilibrium state of solutions under study. But for chemical kinetics it is more important to understand a way, which proceed transition processes in solutions, when a disturbance of equilibrium takes place, for example, by instant appearance of a charge on one of solute and to be able to describe the time-space picture of transition from old equilibrium state of a solution to new one. This problem, known in contemporary literature as "fast hydration dynamics" (FHD) takes last decade much attention and is under intensive investigation experimentally [4], theoretically [5] and by molecular dynamics (MD) simulation [6]. The frequently used characteristic for description of the transition processes mentioned is called as time correlation function of hydration energy S(t). At present there are some theories, dealing with FHD, which give the relation between S(t) and GFD **g (ω)** of hydration water molecules. In particular (see [5]):

$$S(t) = 1 - kT\left\langle(\delta V)^2\right\rangle^{-1} \int d\omega\, g(\omega) \frac{(1-\cos(\omega t))}{\omega^2} \qquad (1)$$

where $\mathbf{(\delta V)^2 = kT(1\text{-}1/\varepsilon) / a}$ – mean-square fluctuations of interaction potential and **a** – radius of sphere beyond which ranges the solution can be considered as structureless continuum with dielectric constant ε.

Our fist attempt to use this relation in combination with GFD for water molecules, obtained by us, demonstrates the qualitative agreement between experimental and calculated (by MD and theory) S(t) curves (see fig. 1). So, there are grounds to believe, the inelastic neutron scattering method among with information about the equilibrium microdynamics of aqueous solutions can be applied for investigation of transition processes, associated with fast hydration dynamics.

The work was performed under financial support of Russian Federation Program "Actual Directions in Condensed Matter Physics", project "Neutron studies".

References

1. A.Novikov, M.Rodnikova, O.Sobolev. J. Mol. Liquids. **82**, 83, (1999).

2. A.G.Novikov, M.N.Rodnikova, V.V.Savostin, O.V.Sobolev. Chem. Phys. Letters. **259**, 391, (1996)
3. A.Novikov, M.Rodnikova, J.Barthel, O.Sjbolev. J. Mol. Liquids.**79**, 203, (1999).
4. S.Rosenthal, X.Xie, M.Du, G.Fleming. J. Chem. Phys. **95**, 4715, (1991).
5. R. Stratt, M.Cho. J. Chem. Phys. **100**, 6700, (1994).
6. M.Maroncelli, G.Fleming. J.Chem. Phys. **89**, 5044, (1988).

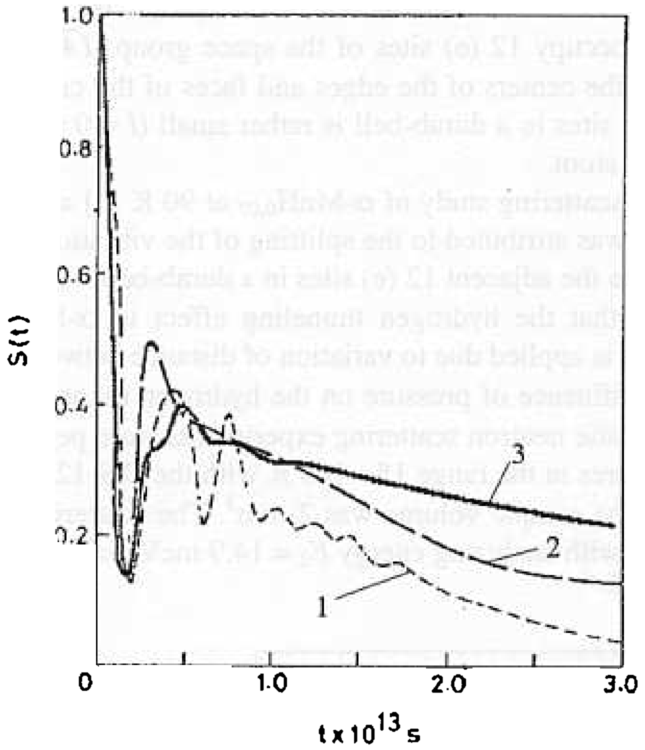

Fig.1. Time correlation function of hydration energy S(t):
1 – MD simulation [6];
2 – theoretical calculation [5];
3 – calculation by equation (1) with the use of the experimental g(ω).

THE EFFECT OF PRESSURE ON HYDROGEN TUNNELING IN α-Mn

V.E.Antonov[a], V.P.Glazkov[b], D.P.Kozlenko[c], B.N.Savenko[c], V.A.Somenkov[b], V.K.Fedotov[a]

[a] *Institute of Solid State Physics RAS, 141432 Chernogolovka Moscow Reg., Russia*
[b] *Russian Research Center "Kurchatov Institute", 123182 Moscow, Russia*
[c] *Frank Laboratory of Neutron Physics, JINR 141980 Dubna Moscow Reg., Russia*

Recently it was shown that under pressure the solubility of hydrogen in α-Mn increases up to a few atomic percent [1]. A neutron diffraction investigation of α-$MnH_{0.07}$ [2] revealed that hydrogen atoms randomly occupy 12 (e) sites of the space group ($I\bar{4}3m$) which form dumb-bells situated rather far apart, at the centers of the edges and faces of the cubic unit cell of α-Mn. Since the distance between 12 (e) sites in a dumb-bell is rather small (l = 0.68 Å) each dumb-bell can be occupied by the only one H atom.

In inelastic neutron scattering study of α-$MnH_{0.07}$ at 90 K [3] a strong peak at 6.3 meV was observed in INS spectra. It was attributed to the splitting of the vibrational ground state of hydrogen due to tunneling between the the adjacent 12 (e) sites in a dumb-bell.

One would expect that the hydrogen tunneling effect in α-$MnH_{0.07}$ may undergo sharp changes if external pressure is applied due to variation of distance between the adjacent H positions.

To investigate the influence of pressure on the hydrogen tunneling effect in α-$MnH_{0.07}$ and α-$MnH_{0.04}$, incoherent inelastic neutron scattering experiments were performed at high pressures up to 3 GPa and low temperatures in the range 15 - 100 K with the DN-12 spectrometer using sapphire anvil high pressure cells. The sample volume was 2 mm^3. The scattering angle was $2\theta = 90°$. The pyrolytic graphyte analyzer with analyzing energy E_2 = 14.9 meV was used for experiments.

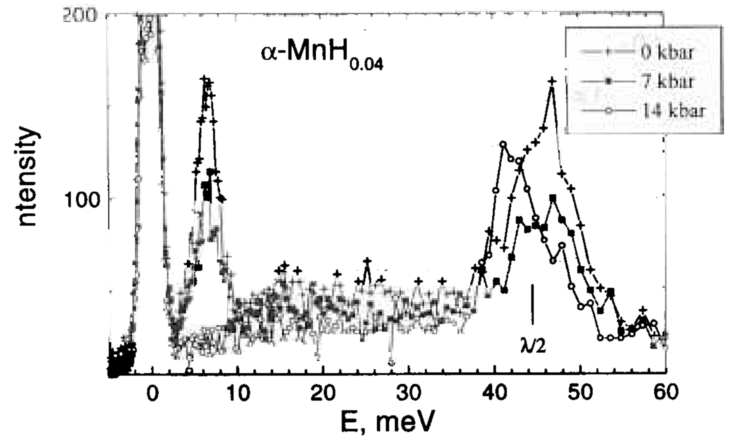

Fig. 1. Inelastic neutron scattering spectra of α-$MnH_{0.04}$ at different pressures obtained with the DN-12 spectrometer using pyrolytic graphite analyzer.

The INS spectra of α-$MnH_{0.04}$ at different pressures are shown in Fig. 1. Hydrogen tunneling peak becomes smaller with the pressure increase. At pressures higher than 10 kbar it completely disappears. In the pressure range up to 10 kbar the tunneling peak position in INS spectra remains nearly the same with the pressure increase. These results show that application of external pressure suppresses the hydrogen tunneling effect in α-Mn.

The work has been supported by Russian Foundation for Basic Research, grant № 00-02-17199.

1. V.E.Antonov et al., Scripta Materialia 34, 1331 (1996).
2. V.K.Fedotov et al., J. Phys.: Condens. Matter 10, 5255 (1998).
3. A.I.Kolesnikov et al., Physica B 263-264, 421 (1999).

NEUTRON DIFFRACTION STUDY OF PYRIDINIUM PERRHENATE AT AMBIENT AND HIGH PRESSURES.

L. Bobrowicz-Sarga [1,2], J. Wąsicki[1], A.I. Beskrovnyi[2], P.Czarnecki[1] I. Natkaniec[2,3],
W. Szczepański[1]

[1]*Institute of Physics, A. Mickiewicz University, 61-614 Poznań, Poland*
[2]*Frank Laboratory of Neutron Physics, JINR, 141980 Dubna, Russia*
[3]*H. Niewodniczański Institute of Nuclear Physics, 31-342 Kraków, Poland*

Pyridine, Py = C_5H_5N, forms salts with many strong mineral and organic acids. These salts belong to a family of molecular – ionic crystals where a solid – solid transition related to changes in ion dynamics occurs. It has recently been found that ferroelectricity exist in pyridinium tetrafluoroborate, perchlorate and perrhenate [1-3]. At atmospheric pressure these salts reveal two solid – solid transitions, and a higher one appears to be the Curie point of the intermediate ferroelectric phase. Both phase transitions are connected with the ordering of the cation and anion reorientations.

As a continuation of our study of pyridinium salts, we report here the results of the neutron powder diffraction study of pyridinium perrhrnate as a function of temperature and pressure. Pyridinium perrhenate, $[C_5\ NH_6\ ]^+[ReO_4]^-$, (hereafter denoted as $PyReO_4$) reveals two structural transitions, at 250 and 333 K. The x-ray diffraction study performed at room temperature shows that the salt crystallises in the orthorombic system, space group $Cmc2_1$. At 333 K, the ferroelectric crystal transforms to Cmcm symmetry and at 250 K, to the space group Pbca.

Neutron scattering experiments were carried out using the time of flight spectrometer NERA-PR installed on the IBR-2 pulsed neutron source of JINR in Dubna. The studied polycrystalline sample at ambient pressure was placed in the cryostat cooled by a close–cycle helium refrigerator permitting temperature changes from 20 – 300 K within an accuracy of 0.5 K. Measurements of neutron scattering spectra as a function of hydrostatic pressure have been performed on the same spectrometer with the aid of a high pressure set-up. The high-pressure helium gas arrangement consist of a U-11GC gas compressor (UNIPRESS, Poland), GNC-400 high-pressure cell and a top loaded cryostat with adjustable temperature in the 78-350 K temperature range. The polycrystalline sample was a cylindrically shaped by an additional aluminium container inserted into the high-pressure cell. The use of helium gas as a pressure-transmitting medium enables the achievement of purely hydrostatic conditions inside the cell. Measurements under high pressure were carried out in the temperature range 90 –310 K and pressures from 0.01 to 370 MPa. Part of the diffraction spectra, between 300 and 350 K at ambient pressure, were measured on the DN-2 diffractometer at the IBR-2 reactor of JINR in Dubna.

The neutron powder diffraction spectra made it possible to determine the experimental intermolecular distances d used in the calculation of unit cell parameters with the AUTOX program [4]. At each temperature, the measured interplanar distances are adequately described by the orthorombic unit cell. Figure1 shows the temperature dependence curves of elementary unit cell parameters. A monotoneus change of all elementary unit cell parameters up to 250 K indicates that the crystalline symmetry of $PyReO_4$ remains unchanged in the temperature range 25-250 K. All phase transitions are clearly seen on the temperature dependence curves of lattice parameters. The phase transition at 250 K, from low-temperature phase III to intermediate phase II, is marked by jumps of the parameters a and c and smaller jumps of the parameters b and volume V. At 333 K the crystal transforms from phase II to high-temperature phase I. This phase transition corresponds to small discontinuous change of all elementary unit cell parameters.

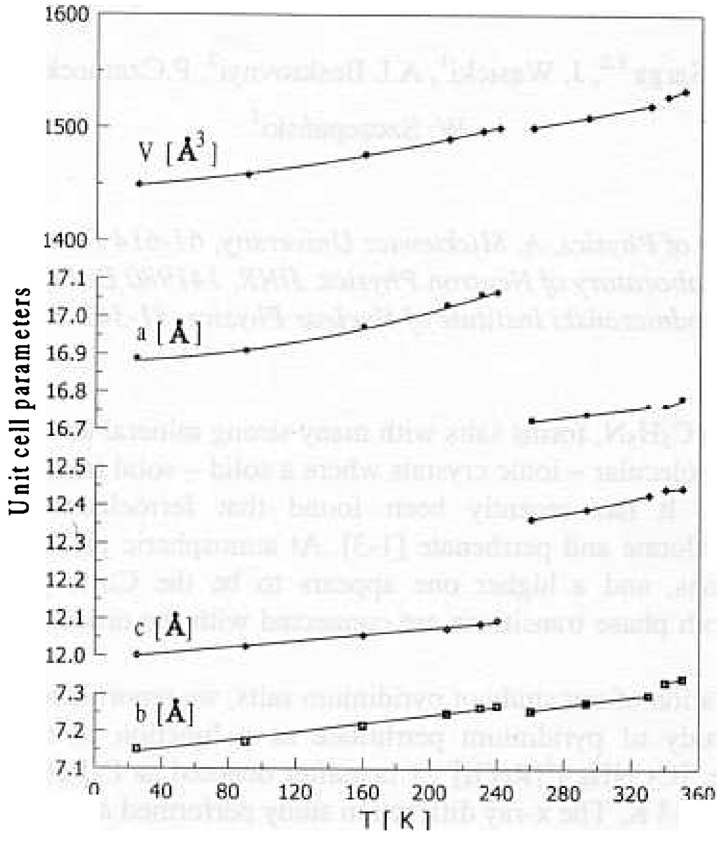

Fig.1. The temperature dependence of the elementary unit cell parameters of PyReO$_4$.

The temperature dependence of the elementary unit cell volume was used to determine the isobar thermal expansion coefficient α from the relative slope of the V_p (T) curves. The values of the parameters α for three phases of the PyReO$_4$ crystal are collected in Table1.

Table1. The isobar thermal expansion coefficient for three phases of PyReO$_4$.

		$\alpha=1/V(dV/dT)_p$ [1/K] x10^{-3}
PyReO$_4$	Phase I	0.347 (p=0.1 MPa)
	Phase II	0.175 (p=0.1 MPa)
	Phase III	0.163 (p=0.1 MPa)

It has recently been observed by some authors (by dielectric and NMR methods) that the new phase transition takes place due to high pressure. To examine the influence of high pressure on the phase transition, the neutron diffraction spectra as a function of hydrostatic pressure were measured at the temperature: 90, 230, 260, and 310 K. Figure 2 presents the most interesting result obtained at the temperature 230K. The upper diffraction spectrum corresponding to the low-temperature phase III was measured in the cryostat cooled by a helium refrigerator. Taking the high-pressure cell background (the lowest spectrum) into account, the spectrum obtained at 80 MPa can be identified as the spectrum of phase III.

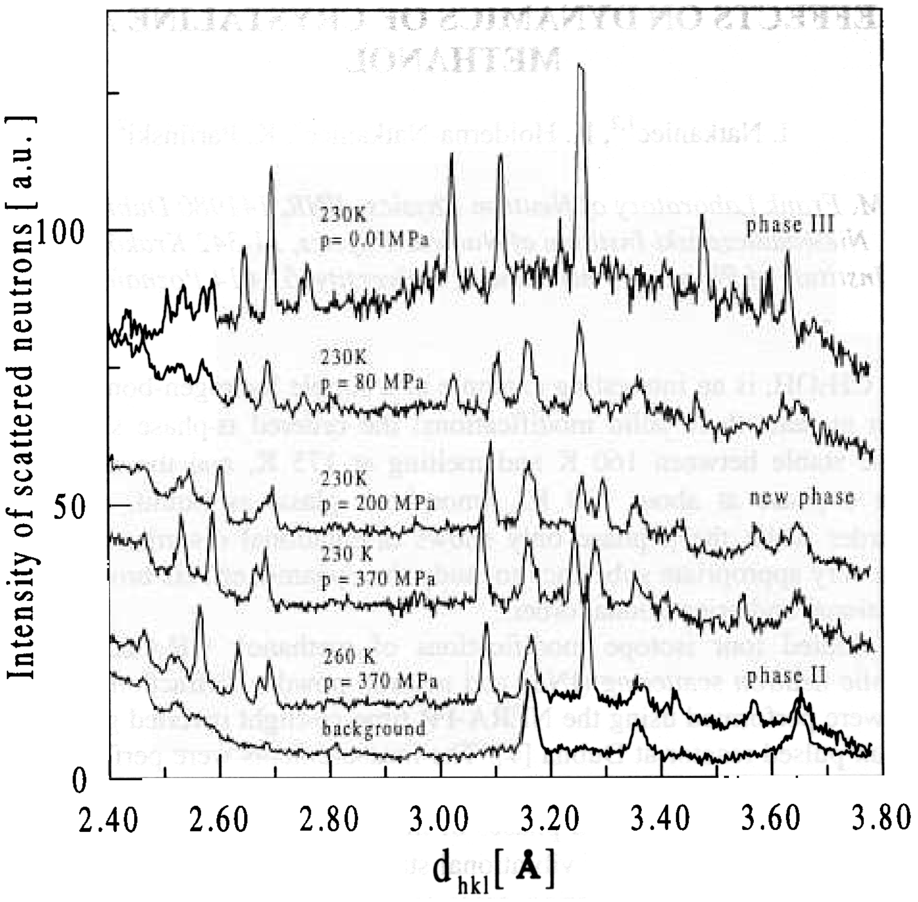

Fig.2. The neutron powder diffraction spectra of pyridinium perrhenate measured with a close-cycle helium refrigerator set-up at ambient pressure (upper spectra at 0.1 MPa) and with a high-pressure set-up.

Visual examination of the spectra measured at 200 and 370 MPa indicate that they differ from this one characteristic for phase III as well as for phase II (spectrum at 260 K). From this we may conclude that the $PyReO_4$ crystal reveals a structural transition to the new phase at 230 K and about 200 MPa. At 230 K and 370 Mpa, the crystal remains in the same phase and then transforms to phase II at equal pressure but higher temperature.

Acknowledgments

The authors express their sincere thanks to Mr. T.Sarga and Mr S.I. Bragin for their help with neutron scattering measurements.

References

[1] P. Czarnecki, W. Nawrocik, Z. Pająk and J. Wąsicki, Phys.Rev.**B** **49**, 1511 (1994).
[2] P. Czarnecki, W. Nawrocik, Z. Pająk and J.Wąsicki, J.Phys.Cond. Matter, **6**, 4955 (1994).
[3] J. Wąsicki, P. Czarnecki, Z. Pająk, W. Nawrocik and W. Szczepański, J.Chem.Phys.**107**, 576 (1997)
[4] V.B. Zlokazov, Comput. Phys Commun., **85**, 415 (1995)

ISOTOPIC EFFECTS ON DYNAMICS OF CRYSTALINE AND VITREOUS METHANOL

I. Natkaniec[1,2], K. Hołderna-Natkaniec[3], K. Parliński[2]

[1] *I.M. Frank Laboratory of Neutron Physics, JINR, 141980 Dubna, Russia.*
[2] *H. Niewodniczański Institute of Nuclear Physics, 31-342 Kraków, Poland.*
[3] *Institute of Physics, A. Mickiewicz University, 61-614 Poznań, Poland.*

Methanol, CH_3OH, is an interesting example of a simple hydrogen-bonded organic crystal. It is known to exist in at least three solid modifications: the ordered α-phase stable below 160 K, the disordered β-phase stable between 160 K and melting at 175 K, and the amorphous phase, which transforms to the α-phase at about 130 K. Amorphous glass, as liquid, shows translational and orientational disorder while the β-phase only shows orientational disorder of plastic crystals. This makes methanol a very appropriate substance to study the dynamic effects brought forward due to loss of long-range positional and orientational order.

We have studied four isotope modifications of methanol: CH_3OH, CH_3OD, CD_3OH and CD_3OD, by inelastic neutron scattering (INS) and neutron powder diffraction (NPD), simultaneously. The experiments were performed using the NERA-PR time-of-flight inverted geometry spectrometer at the IBR-2 high flux pulsed reactor at Dubna [1]. The measurements were performed at temperature 20 K, over a wide range of momentum and energy transfer. These allow us to investigate the vibrational spectra up to 2000 cm^{-1} for all condensed phases of methanol whose structures were controled by the NPD method. The generalized density of vibrational states - G(ω) (weighed over square amplitudes of atom vibrations and their neutron scattering cross-sections) for the crystalline α-phase at 20 K, is shown in Fig. 1.

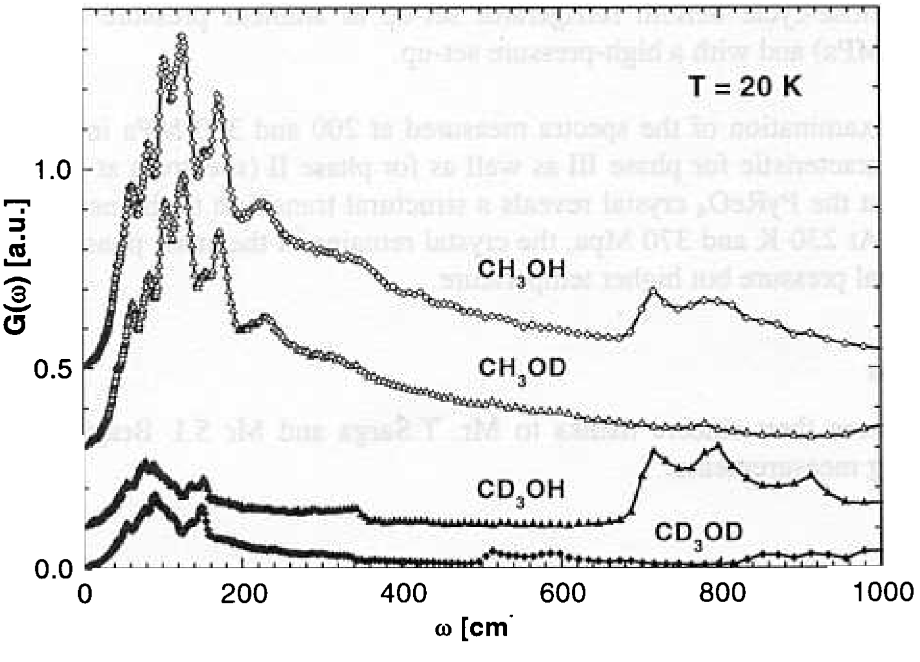

Fig. The weighed densities of vibrational states G(ω) of crystalline methanol in the solid α-phase at 20 K for differently deuterated molecules.

The glass samples were prepared by fast quenching of room temperature liquid samples (in a liquid nitrogen bath) just before placing them into the measuring cryostat well, which was cooled to about 20 K. The sample container was an aluminum plate 16x7 cm^2 of ca.1 mm internal thickness. A comparison of the G(ω) spectra of vitreous and crystalline samples of CH_3OD and CD_3OH, is shown in Fig. 2.

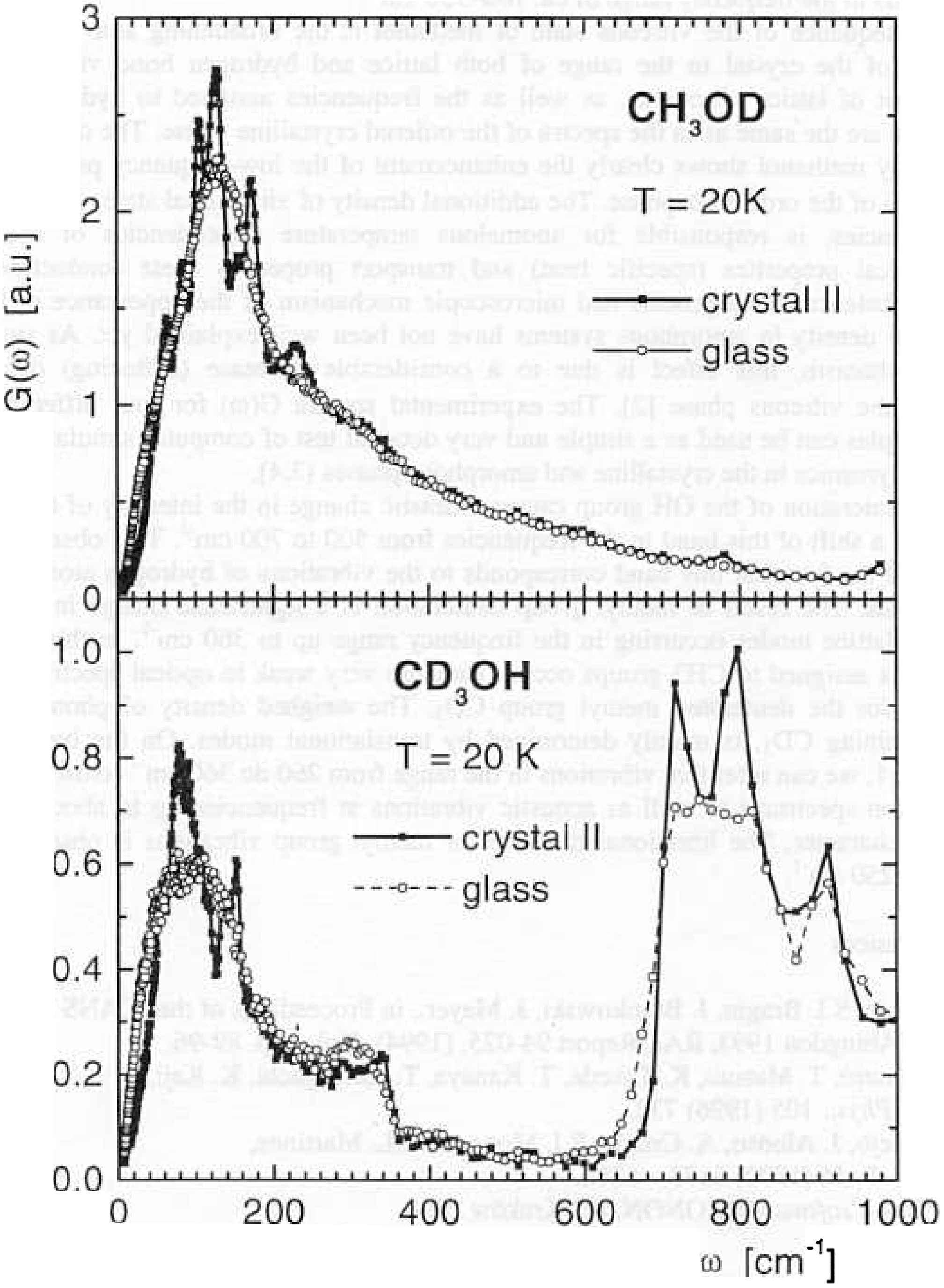

Fig. 2. The weighed densities of vibrational states G(ω) for vitreous and crystalline methanol at 20 K and for partly deuterated CH_3OD and CD_3OH molecules.

The intensities of the G(ω) spectra presented in figures 1 and 2 were normalised to equal mass and volume of the sample, and equal number of neutrons incident on the sample.The different isotope modifications of methanol molecules allow as to study the contribution of methyl group rotations and hydroxyl dynamics to lattice dynamics. Wide range of energy transfer allows one to display the effects of disorder in the whole frequency range of lattice dynamics up to ca. 400 cm^{-1}, and on the dynamics of hydrogen bonds in the frequency range of ca. 700–950 cm^{-1}.

A consequence of the vitreous state of methanol is the broadening and smoothing of bands characteristic of the crystal in the range of both lattice and hydrogen bond vibrations. The high-frequency limit of lattice vibrations, as well as the frequencies assigned to hydrogen bonds, in the vitreous phase are the same as in the spectra of the ordered crystalline phase. The density of vibrational states of glassy methanol shows clearly the enhancement of the low-frequency part comparing to the reference G(ω) of the ordered α-phase. The additional density of vibrational states in the vitreous phase at low-frequencies, is responsible for anomalous temperature dependencies of the macroscopic thermodynamical properties (specific heat) and transport properties (heat conduction), typical of amorphous substances. The genesis and microscopic mechanism of the appearance of the additional vibration state density in amorphous systems have not been well explained yet. As suggested in the proposed mechanism, this effect is due to a considerable decrease (softening) of the librations frequency in the vitreous phase [2]. The experimental spectra G(ω) for four differently deuterated methanol samples can be used as a simple and very detailed test of computer simulations of molecular glass former dynamics in the crystalline and amorphous phases [3,4].

The deuteration of the OH group causes a drastic change in the intensity of the band at 700 to 950 cm^{-1}, and a shift of this band to the frequencies from 500 to 700 cm^{-1}. This observation is a direct confirmation f the fact that this band corresponds to the vibrations of hydrogen atoms in the chain of hydrogen bonds. The result of methyl group deuteration is a significant change in the intensity and frequency of lattice modes occurring in the frequency range up to 360 cm^{-1}. In this range the strong libration bands assigned to CH3 groups occur. They are very weak in optical spectroscopy and in the IINS spectra for the deuterated methyl group CD_3. The weighed density of phonon states, for the samples containing CD_3, is mainly determined by translational modes. On the basis of the spectra shown in Fig. 1, we can infer that vibrations in the range from 260 do 360 cm^{-1} (close to the limit of the lattice vibration spectrum) as well as acoustic vibrations at frequencies up to about 90 cm^{-1}, have a translational character. The librational character of methyl group vibrations is observed in the range from ~100 to 250 cm^{-1}.

References

[1]. I. Natkaniec, S.I. Bragin, J. Brankowski, J. Mayer., in Proceedings of the ICANS XII Meeting, Abingdon 1993, RAL Report 94-025, (1994), Vol. I., p. 89-96.

[2]. O. Yamamuro, T. Matsuo, K. Takeda, T. Kanaya, T. Kawaguchi, K. Kaji, *J. Chem. Phys.*, 105 (1996) 732.

[3]. F.J. Bremejo, J. Alonso, A. Criado, F.J. Monpean, J.L. Martinez, *Phys. Rev. B*, **46** (1992) 6173 – 6286.

[4]. K. Parliński, *software* PHONON, IFJ Kraków 2000.

COMPUTER SIMULATION AND NEUTRON SCATTERING INVESTIGATION OF DYNAMICS OF UREA: $CO(NH_2)_2$ AND $CO(ND_2)_2$

I. Natkaniec[1,2]. K. Parliński[2], K. Hołderna-Natkaniec[3], J. Mayer[2]

[1] *I.M. Frank Laboratory of Neutron Physics, JINR, 141980 Dubna, Russia.*
[2] *H. Niewodniczański Institute of Nuclear Physics, 31-342 Kraków, Poland.*
[3] *Institute of Physics, A. Mickiewicz University, 61-614 Poznań, Poland.*

Physical and chemical properties of urea NH_2-CO-NH_2 have been studied for many years. The crystal structure of urea is relatively simple and has been resolved as one of the first structures of organic compounds. Under normal pressure the tetragonal structure of crystalline urea of the D^3_{2h} symmetry with two molecules in the elementary unit does not change with temperature varied from the melting point to that of liquid helium [1]. The chemical singularity of this structure is the fact that each oxygen atom from the CO group accepts four hydrogen bonds N-H...O.

Computer simulations of the dynamics of molecular crystals are much in demand but very difficult because of the degree of complication of their structure. This dynamics includes lattice modes corresponding to mutual vibrations of molecules and vibrations of atoms in molecules (internal modes), also dependent on the crystal field. Recently, the programs for simulation of structure and dynamics of molecular crystals based on generalised semi-empirical field force methods and the "*ab initio*" calculations based on the methods of quantum chemistry have been tested. The authors of [2] presented results of computer simulation of the dispersion curves for deuterated urea obtained by a combination of these two calculation methods.

Here we report a comparison of the calculated phonon densities of state weighted by the amplitudes of atoms vibrations in the given modes - G(ω), with the experimental one, which can be determined from the spectra of inelastic neutron scattering on polycrystalline samples. The spectra of inelastic neutron scattering on the powdered samples of $CO(NH_2)_2$ and $CO(ND_2)_2$ were performed at 20 K, on a NERA spectrometer [3] at the pulse reactor IBR-2 in Dubna. The experimental densities of phonon states G(ω) were determined in the approximation of single-phonon scattering for frequencies up to 1000 cm^{-1}. A satisfactory agreement was obtained between the calculated and experimental results in the range of the lattice modes frequencies (see Fig. 1, below 220 cm^{-1}). These spectra are very little dependent on deuteration of the urea molecule. The significant isotopic shifts were observed for the internal vibrations in the range from 300 to 1000 cm^{-1}. The frequencies of these vibrations calculated by the *ab initio* method are in a worse agreement with experiment than those of lattice vibrations. However the calculated intensities of internal bands and their isotopic shifts permit a reliable interpretation of the experimental spectra.

1. S. Swaminathan, B.M. Craven, R.K. McMullan, Acta Cryst. **B40** (1984) 300-306.
2. K. Parlinski, G. Chapuis, J. Chem. Phys., **110** (1999) 6406-6411.
3. I. Natkaniec, S.I. Bragin, J. Brankowski, J. Mayer., in Proceedings of the ICANS XII Meeting, Abingdon 1993, RAL Report 94-025, (1994), Vol. I., p. 89-96.

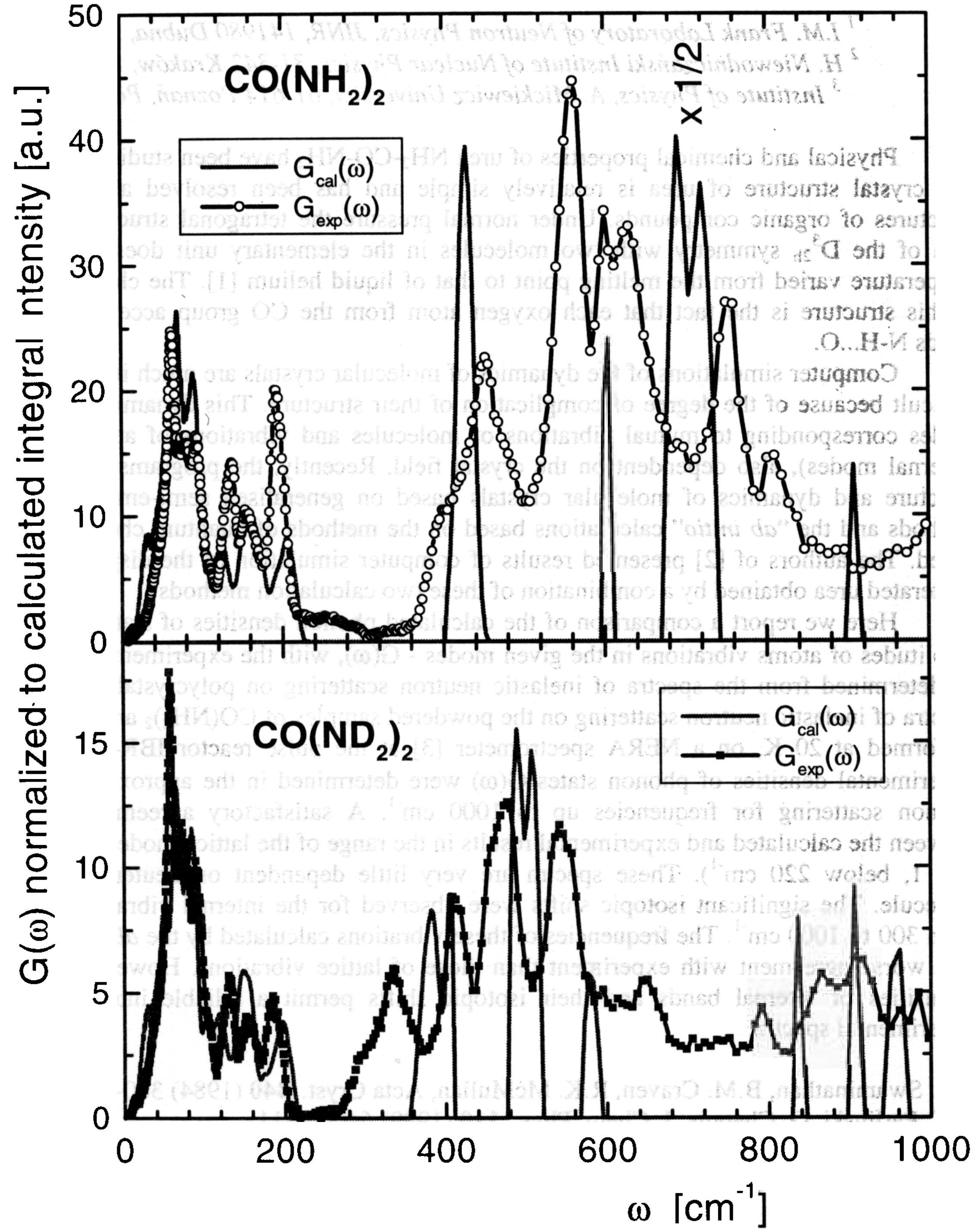

Fig. Calculated and experimental neutron scattering weighted vibrational density of states of crystalline urea at 20 K.